Master Thesis in Geosciences

COMPACTION, EVOLUTION OF ROCK PROPERTIES AND AVO MODELING

Tornerose Prospect

South West Barents Sea

Rock property evolution and AVO modeling

Abel Onana Ndingwan

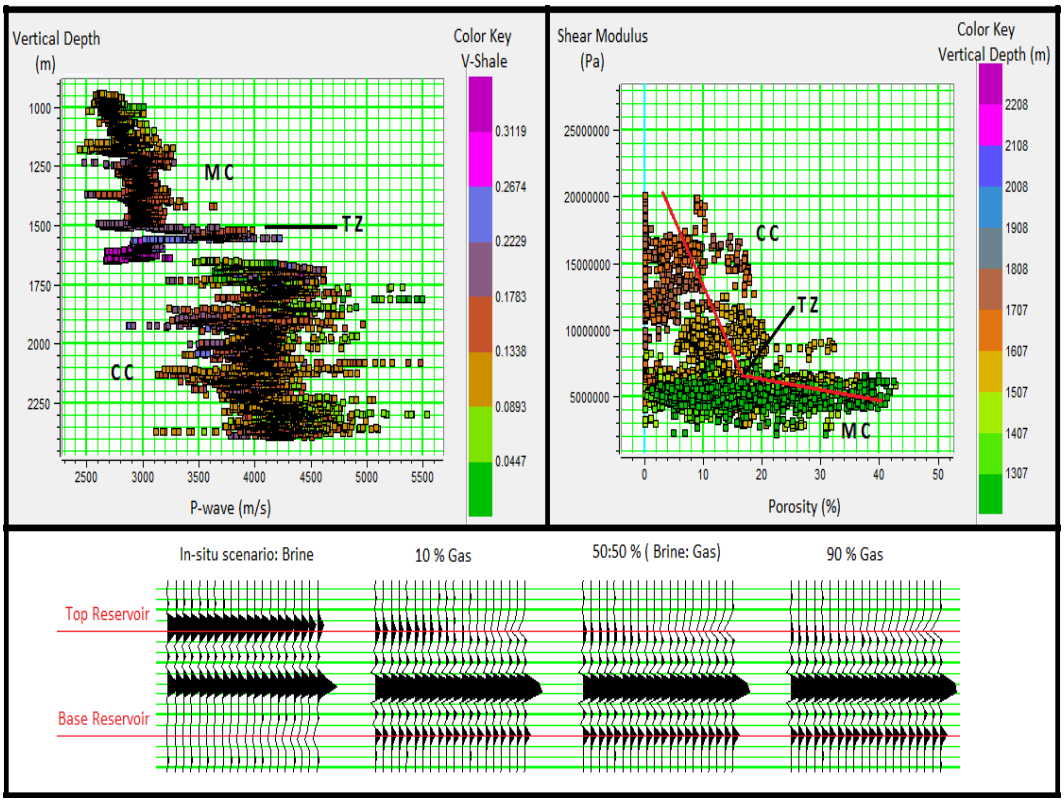

UNIVERSITY OF OSLO

FACULTY OF MATHEMATICS AND NATURAL SCIENCES

COMPACTION, EVOLUTION OF ROCK PROPERTIES AND AVO MODELING

Tornerose Prospect

South West Barents Sea

Rock property evolution and AVO modeling

Abel Onana Ndingwan

Master Thesis in Geosciences

Discipline: Petroleum Geology and Petroleum Geophysics

Department of Geosciences

Faculty of Mathematics and Natural Sciences

UNIVERSITY OF OSLO

01.06.2011

Tutor(s): Associate Professors **Jens Jahren (UiO) and Nazmul Haque Mondol (UiO)**
This work is published digitally through DUO – Digitale Utgivelser ved UiO
http://www.duo.uio.no
It is also catalogued in BIBSYS (http://www.bibsys.no/english)

Preface

This research is part of the BarRock (Barents Sea Rock Properties) Project.
It is submitted to the Section of Petroleum Geology and Petroleum Geophysics,
Department of Geosciences, University of Oslo (UiO) in
candidacy of an MSc. Degree.

The research has been performed at the Department of Geosciences, UiO,
during the period of January to May 2011 under the supervision of
Associate Professors: Nazmul Haque Mondol and Jens Jahren,
Section of Petroleum Geology and Petroleum Geophysics,
University of Oslo, (UiO),
Norway

DEDICATION

This research is dedicated to my lovely mother, Epo Mary Isabelle, for the constant love, patience, encouragements and prayers particularly during the writing of this thesis.

Acknowledgements

I profoundly thank my supervisors: Associate Professors Nazmul Haque Mondol and Jens Jahren for the valuable support, guidance, inspiring ideas and tutorship from the conception to maturation of this thesis. All the long status meetings in your offices will be missed. I also thank Manzar Fawad for his technical inputs during the practical sessions in the laboratory.

I owe special gratitude to my lecturers Johan Petter Nystuen and Roy Helge Gabrielsen for their inspiration during a field course in Ainsa, Spain. Their academic inputs encouragements, advice and had been constant.

To the following lecturers who have taught me all that they know to the best of their abilities, I do hereby express my gratitude for the knowledge and confidence received: Knut Bjørlykke, Jan I. Faleide, Leiv Gelius, Dag Karlsen, and Michael Heeremans. I further thank the entire staff of the Geoscience department for the wonderful education and training.

Special gratitude to my parents who have always supported me from day one. I would like to thank my family; Williams Chindo, the Mbata family, Jennifer, Toube, Grand soeur Doris, Eugene and petit frère Danny for their support and patience during the writing of this thesis.

Thanks to my classmates Fai Honore, Agus Fitriyanto, Piratheeben k. and Tashi Tshering for the interesting and long discussions.

Finally, I thank all my friends mentioned herein and to those whose names have not been mentioned but have always supported me in one way or the other: Nana Afriyie Takyi, Nkemtaji Moses, Olivier Pamen, Emesum family, Tizinbu Eric, and Toh Lih Raymond for their assistance. To Ronny Rønning, the first Norwegian I ever met: thank you.

Thank you God.

Abstract

The Barents Sea is an active area for frontier petroleum exploration .This study focuses on an area across the Tornerose prospect in the Hammerfest Basin, South West of the Barents Sea. Cenozoic exhumation of the entire region resulted in dramatic changes in rock properties and eventual petroleum systems therein. Analysis of this sedimentary basin as a normally subsiding basin would yield misleading results. The focus of this thesis comprise of two phases which are compaction analysis and evolution of rock properties as a function of depth coupled with AVO/AVA (amplitude versus offset/angle) evaluation and modeling of the Stø and Snadd reservoirs.

Petrophysical logs from 5 wells, published natural compaction curves and experimentally compacted mudstone and sandstone curves have been used to investigate compaction and evolution of rock properties of the area. Mechanical compaction dominates as a monotonic function of vertical effective stress from the overburden to depths of about 1530m BSF (well 7123/4–1A). An abrupt velocity increase at this depth corresponding to present day temperatures of 45.9°C is inferred to as resulting from grain framework stiffening related to precipitated micro-quartz released from the transformation of the clay mineral smectite to illite via mixed layer smectite – illite (SI). This marks the transition zone to chemical compaction. The high velocity/depth ratio of these sediments compared to experimentally compacted synthetic mudstones is related to the burial history and subsequent uplift. Correcting for exhumation yields estimates in the range of 1200 to 1600m.Velocity and density inversion in the organic rich Hekkingen Formation due to high pore pressures, among other factors, could possibly have contributed to the good reservoir quality in the underlying Stø reservoir sandstones.

Lateral variation of the cap rock elastic properties greatly control the AVO character of the Stø reservoir. Lithological heterogeneity within the Snadd reservoir reduces the impedance contrast with the overlying Fruholmen Formation giving low AVO response. A systematic increase in pore fluid compressibility in the Stø reservoir results in a corresponding decrease in reflection coefficients. Substituting brine with an initial 10% gas as reservoir pore fluid results in remarkable changes on seismic. However these changes are not evident for higher gas saturations of 50 to 90%. AVO modeling effectively quantifies these fluid effects at all gas saturations. The result presented herein establishes possible AVO variation trends for increasing gas saturation within the Stø reservoir. The various models within the framework of this thesis give a quick preliminary AVO evaluation of the Stø and Snadd reservoirs. With an expanding data base, more constrains could be incorporated into these elementary models.

Table of Contents

Preface.....i

Acknowledgements.....iii

Abstract.....iv

Table of Contents.....v

CHAPTER 1: INTRODUCTION

1.1 General.....1

1.2 Motivation of Research.....3

1.3 General Description of Thesis Outline.....4

1.4 Research Objectives.....4

1.4.1 Compaction and Evolution of Rock Properties.....5

1.4.2 AVO (Amplitude versus Offset) Modeling.....5

1.5 Study Area.....6

1.6 Materials and Methods.....7

1.6.1 Database.....7

1.6.2 Software.....9

1.6.3 Methods.....11

CHAPTER 2: REGIONAL GEOLOGIC FRAMEWORK

2.1 Structure and Tectonics.....13

2.2 Stratigraphy.....14

2.2.1 Nordland Group.....14

2.2.2 Sotbakken Group.....14

2.2.3 Nygrunnen Group.....15

2.2.4 Adventdalen Group.....16

2.2.5 Kapp Toscana Group.....16

2.3 Petroleum System.....17

2.3.1 Source Rocks.....17

2.3.2 Studied Reservoir Units.....19
2.3.2.1 Stø Reservoir.....19
2.3.2.2 Snadd Reservoir.....21
2.3.3 Trap.....23

CHAPTER 3: COMPACTION AND EVOLUTION OF ROCK PROPERTIES

3.1 Introduction.....24
3.2 Theoretical Background.....26
3.2.1 Mechanical Compaction.....26
3.2.2 Chemical Compaction.....28
3.2.3 Compaction of Clays, Mudstones and Shales.....29
3.2.4 Compaction of Sandstones.....32
3.3 Methodology.....34
3.3.1 Correlative Analysis of Petrophysical logs.....34
3.3.2 Cross plots.....34
3.3.3 Correction for Exhumation and Comparative analysis.....35
3.4 Results.....36
3.4.1 Compaction Trends in the Study Area.....36
3.4.2 Transition Zone from Mechanical to Chemical Compaction.....39
3.4.3 Rock Property Variations.....41
3.4.4 Correction for Exhumation and Comparative Analysis.....44
3.5 Discussion of Results.....49
3.5.1 Compaction as a Function of Rock Properties.....49
3.5.2 Exhumation.....54
3.5.3 Compaction in Source Rocks.....55
3.5.4 Uncertainties.....57

CHAPTER 4: AVO/AVA MODELING

4.1 Introduction.....59

4.2 Theoretical Background.....60

4.2.1 Reflectivity Series.....60

4.2.2 The convolutional Trace Model.....60

4.2.3 Zoeppritz Equation and Aki-Richard approximation.....61

4.2.4 AVO Reservoir sand Classification Scheme.....64

4.2.5 Gassmann's Theory and Fluid Substitutions.....66

4.3 Methodology.....69

4.3.1 Shear Wave Velocity (Vs) Estimation 69

4.3.2 Water Saturation (Sw).....70

4.3.3 Density to Porosity Transform.....71

4.3.4 Wavelet.....71

4.3.5 Upscaling.....72

4.3.6 AVO/ AVA Modeling.....73

4.4 Results.....75

4.4.1 Stø Reservoir.....75

4.4.2 Snadd Reservoir.....77

4.4.3 Sensitivity Analysis.....78

4.5 Discussion of Results.....80

4.5.1 Cap rock Properties.....80

4.5.2 Pore Fluid Property and Saturation Effects on AVO Response.....82

4.5.3 Facies Variations and Depth Dependent AVO Signature.....84

4.5.4 Models Uncertainties.....85

CHAPTER 5: SUMMARY AND CONCLUSIONS

5.1 Summary.....86

5.2 Conclusions.....88

REFERENCES.....91

Appendix.....103

CHAPTER 1: INTRODUCTION

1.1 General

The Barents sea is a shallow epicontinental sea with an average water depth of around 230m and covers an area of about 1.2 x 10^6 Km^2 (Butt et al., 2002). The Norwegian Barents Sea is located north of Norway and Russia. It is bordered by the shelf edge towards the Norwegian Sea in the west, the island of Svalbard (Norway) in the northwest, and the islands of Franz Josef Land and Novaya Zemlya (Arkhangelsk Oblast) in the northeast and east respectively (Fig. 1.1). This is a highly explored area for oil and gas dating back to the 1970s with the first offshore drilling in the early 1980s. Askeladd discovery was the first to be made one year later in 1981.

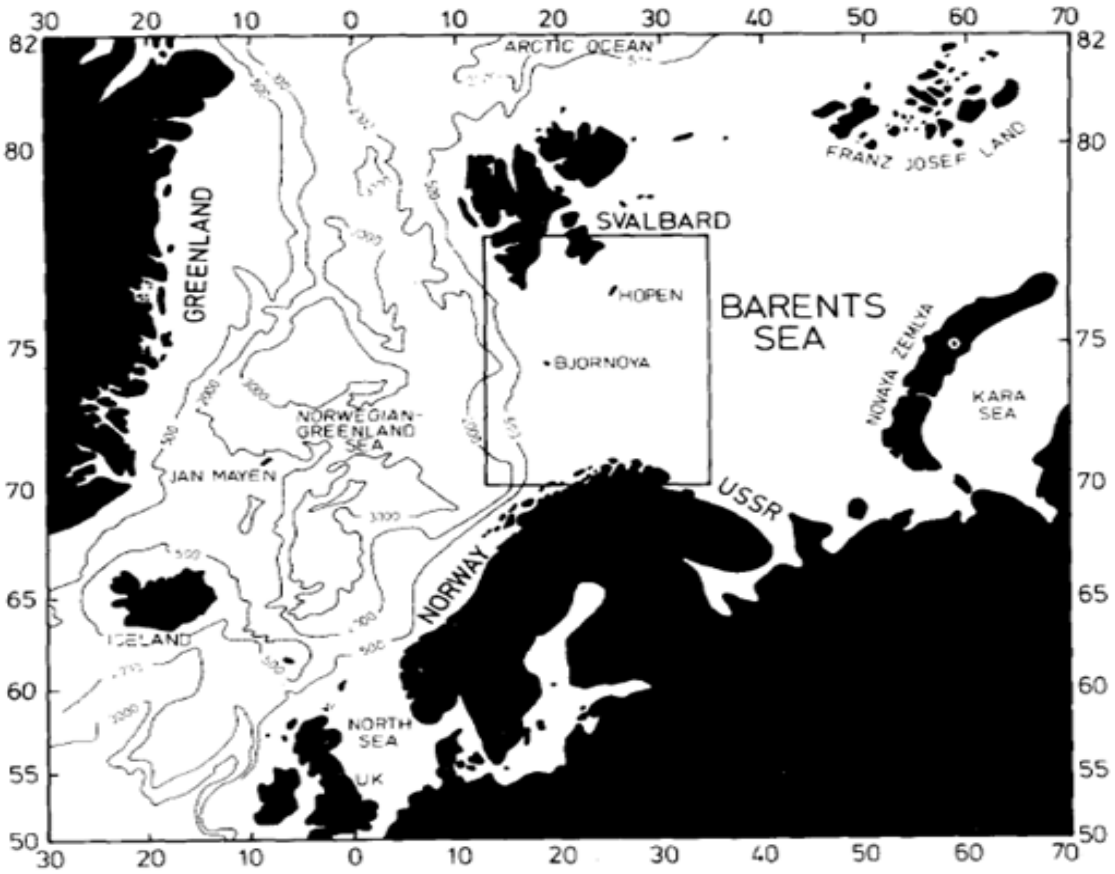

Fig. 1.1 Location map of the Barents Sea. Source: (Faleide et al., 1984)

Over the past years, a number of wells have been drilled in the area with only a couple of major commercially significant oil and gas fields found such as the Snøhvit and Goliat fields

(Fig.1.2). Most of the discoveries yielded gas such as the Snøhvit, Albatross and Askeladd gas fields. The Snøhvit gas field, discovered in 1984, started development in 2005 as the first offshore development project in the Barents Sea and a stepping stone for resource exploitation in the Arctic. A latest discovery (Skrugard in 2011) has presented a significant break-through for frontier exploration with the possibility of the area becoming a future oil province. The Skrugard discovery, located approximately 150 Km northwest of the Goliat field, was made through exploration well 7220/8 – 1 and was the first well to be drilled in production license PL532 awarded in 2009 within the 20th Norwegian licensing round. However, further east in the Russian sector lies the giant Shtockmanovskoye and Ludlovskoye gas fields.

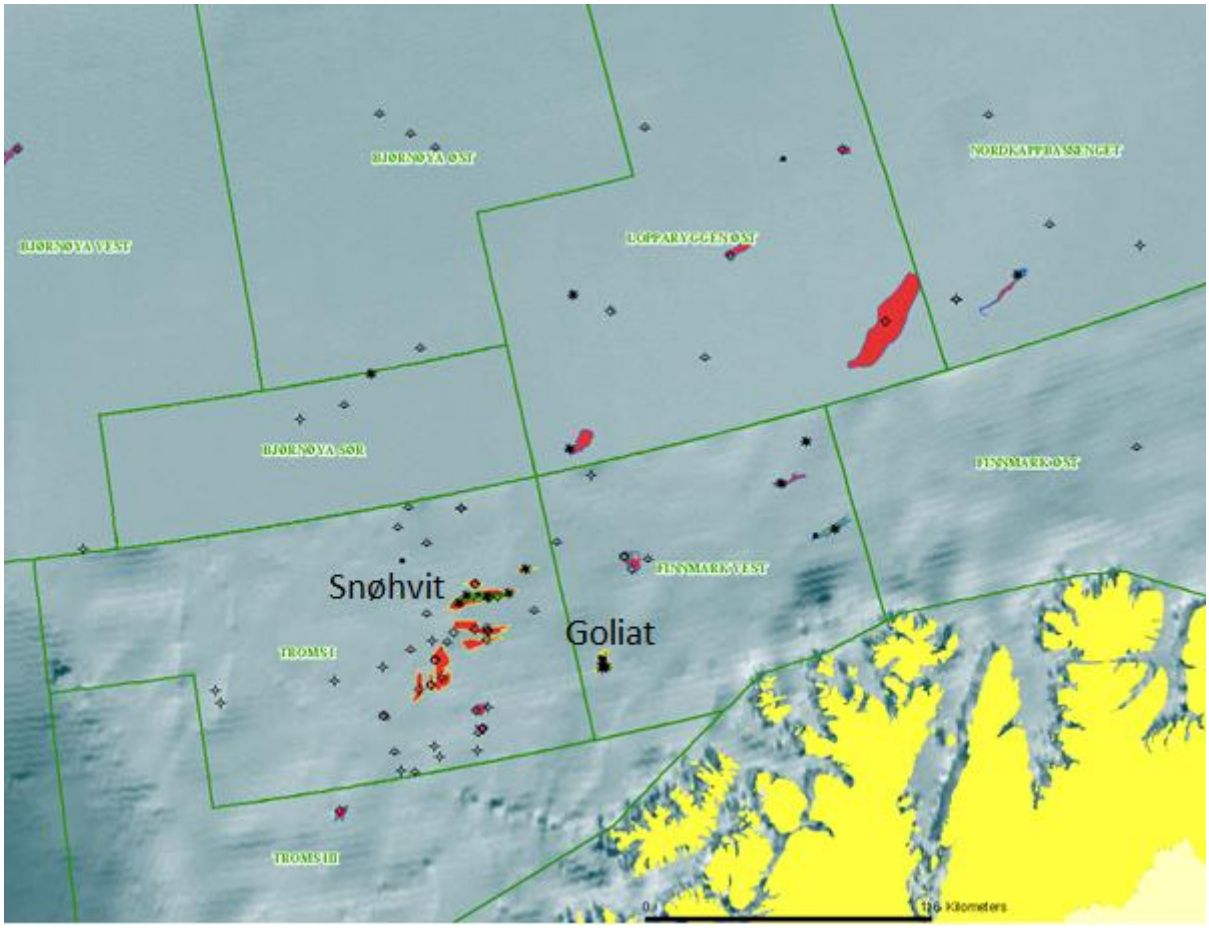

Fig. 1.2. Location map of two major commercial hydrocarbon fields in the South West Barents Sea: Snøhvit and Goliat Fields. Modified from NPD Factmaps (2011)

Following the 21st licensing round in April 2011, the Norwegian Government awarded 24 offshore oil and gas production licenses (PL), half of which were in the Barents Sea. Exploration and development in this area is technologically complex and expensive given

the extremely low temperatures, sea ice, and long distances from existing infrastructures. However, soaring oil prices and ground-breaking technologic advances have attracted exploration activities.

According to the United States Geological survey (USGS) (Bird et al., 2008), in an unbiased geology-based probabilistic methodology to estimate undiscovered oil and gas resources, through a Circum-Arctic Resource Appraisal, approximated that in the Barents Sea region, there are $\approx 326.10^6$ m^3 of oil, $\approx 743.10^6$ m^3 of natural gas and $\approx 44.10^6$ m^3 of natural gas liquids still undiscovered. Several phases of uplift and erosion have probably caused depletion and redistribution of hydrocarbon accumulation in the Barents Sea region.

1.2 Motivation of Research

On a global scale, hydrocarbon resources are finite and the rate at which new hydrocarbon discoveries are found is in a decline, particularly at a period when the demand for oil and gas continuously increases. In many areas the rate of production supersedes that of reserves replacement. On the other hand in several mature hydrocarbon provinces, the reserves are there; but they need to be located or extracted more efficiently. A robust combination of reservoir characterization techniques and the latest software packages yields top-notch improvements to production in existing fields.

Characterization of virgin reservoir relies mainly on techniques such as; AVO, inversion, seismic attributes, statistical modelling and simulation and, in certain cases, multicomponent data. In the case of a reservoir under production, more emphasis is laid on the link between seismic data and reservoir fluid, pressure and temperature. Seismic data analysis is therefore one of the key technologies for characterizing reservoirs. However while there has been mile-stone advances in 3D seismic data processing, the quantitative interpretation of the seismic data for rock property determination still represents a challenge (Avseth, 2005).

The ultimate goal therefore of a petroleum geoscientist is to define reservoirs in terms of its porosity, permeability, fluid content, lateral and vertical heterogeneity and net-to-gross prior to drilling and during production. Much work is done to include as many sources of information as possible into reservoir characterization. Information is required from well logs, cores and cuttings, seismic and production data and geotechnical input. This has led to an increasing need for reservoir characterization technology within the oil and gas industry.

The need is mostly driven by economic realities. That is if reservoirs can be defined appropriately using available technology, then the end result is higher drilling success and optimizing reservoir production over the life of the field.

1.3 General Description of Thesis Outline

A progressive and systematic integration of rock property evolution with depth and AVO modeling approach is employed to investigate the main concerns within the framework of this study. This description gives the general outline of

Chapter I, general aspects of the Barents Sea region, the Hammerfest basin and Tornerose prospect will be addressed. The objectives of the entire study will be spelled out. The materials and methodology of the entire thesis are introduced at this level.

Chapter II discusses the geologic framework which shall be divided into two parts: the structural setting and stratigraphic successions encountered by the different wellbores. Background on the petroleum system will be reviewed. The two reservoir units that shall be the later focus of this study are also briefly discussed in this section.

Chapter III, a more detailed analysis of the evolution of dynamic rock properties of the various stratigraphic successions is done in this section. Evaluation of implications of the structural history (Cenozoic exhumation) and rock property changes is addressed both at Group and Formation levels.

Chapter IV focuses on mainly on the Stø and Snadd reservoir units. Reflectivity as a function of offset/ angle is evaluated at the top reflector of these reservoirs from different perspectives. Several AVO models will be developed within this section for further analysis of these reservoir units.

Chapter V summarizes and presents succinct conclusions of this study based on the analysis of datasets, available literature and assumptions made throughout this study.

1.4 Research Objectives

Most petroleum reservoirs are heterogeneous. The pattern of heterogeneity in sandstone reservoirs, which determines the volumes, flow rates and recovery of hydrocarbons, are controlled by geometry and internal structures of sand bodies, grain size, sorting, degree of

bioturbation, provenance and by the types, volumes and distribution of diagenetic alterations. (Morad et al., 2010). The presence of clays and shales in reservoir rocks add even more complexity. Understanding the link between geologic processes and seismic signatures is of prime importance in reservoir characterization. Rock physics can give a more quantitative link between seismic, well logs and reservoir properties. Moreover, understanding compaction mechanisms is important in sedimentary basins as this causes changes in physical properties of sediments during burial. These physical parameters control reservoir quality and available pore space for hydrocarbon accumulation.

The main objective of the thesis is to understand compaction behaviour, evolution of rock properties and AVO (Amplitude Versus Offset) modeling of reservoir horizons of Tornerose discovery in Block 7122, Barents Sea. These issues are highlighted in the research under two major headings:

1.4.1 Compaction and Evolution of Rock Properties

- Analysis of major compaction mechanisms as a function of rock properties and depth across the study area.
- Determine the transition between mechanical and chemical compactions and its effect on dynamic rock properties.
- Identify gross potential reservoir intervals and how they compact relative to shales.
- Estimate the magnitude of Cenozoic exhumation undergone by sediments across the study area and its impact on reservoir quality.
- Comparative analysis of experimentally compacted synthetic mudstones to constrain the naturally compacted sediments.

1.4.2 AVO (Amplitude versus Offset) Modeling

- Evaluate reflectivity as a function of offset at the top of the Stø and Snadd reservoir intervals. Further classify these reservoir sands both at in-situ condition and when they are oil and gas filled. The classification is based on Rutherford and William's classification scheme.
- Quantitatively model different pore fluid saturations and fluid property effects on synthetic NMO corrected CDP gathers and on angle dependent reflectivity.

- Evaluate the relationship between elastic rock properties and AVO/ AVA response.
- Evaluate the variability in cap rock properties and depth dependent AVO/ AVA response.

1.5 Study Area

Hammerfest basin is situated between 70° 50' N, 20°E, 71°15'N, 20°E, 72°15'N, 23°E and 71°40'N, 24°10'E. The basin is relatively shallow and has a NE- SW striking axis. To the south, the Hammerfest basin is separated from the Finnmark platform by the Troms-Finnmark fault complex. To the north, it is separated from the Loppa High by the Asterias Fault complex. To the west it is limited towards the Tromsø Basin by the southern segment of the Ringvassøy – Loppa Fault complex. Its eastern boarder terminates against the Bjarmeland platform.

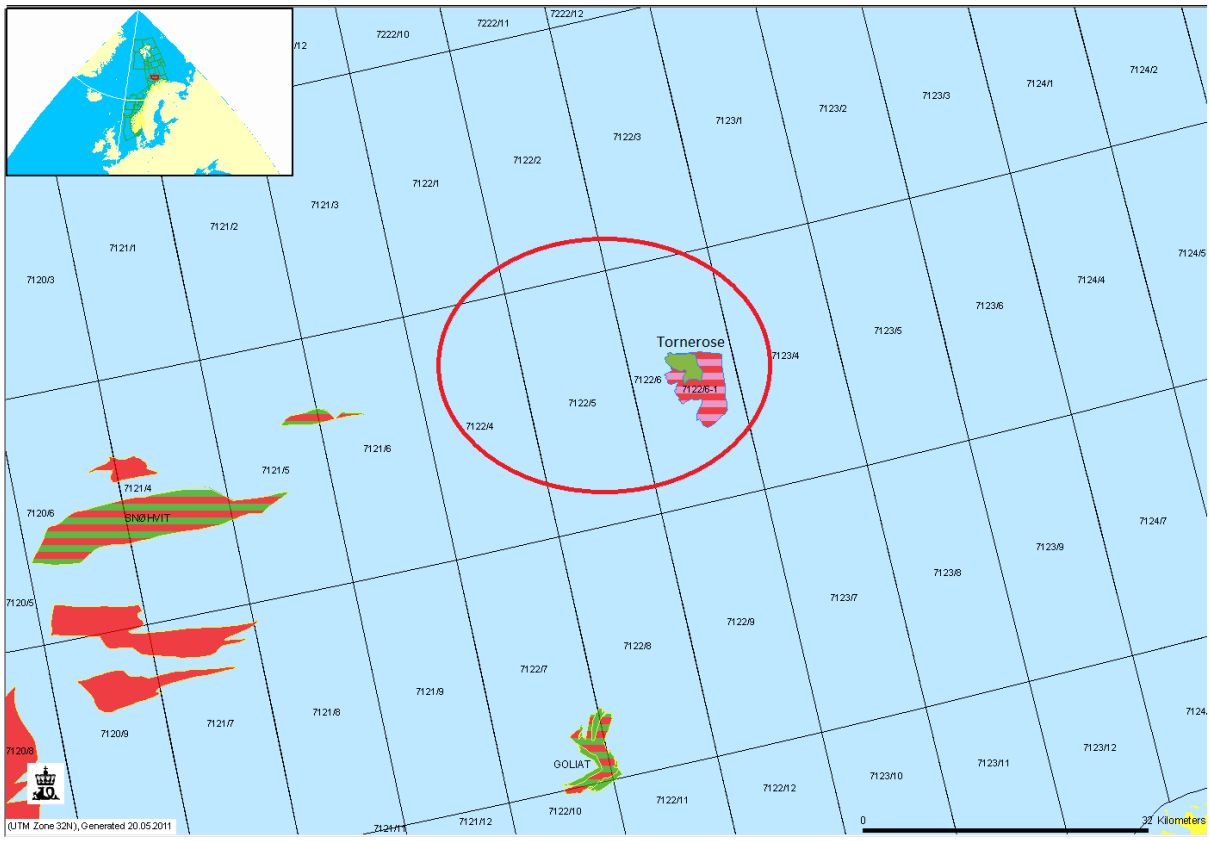

Fig. 1.3 Map of Norway and Barents Sea (inset map) and location of the study area about 45Km NNE of Goliat and about 55Km east of Snøhvit fields. Modified from: NPD Factmaps. (2011).

The Tornerose prospect, found in block 7122, is located about 45km NNE of the Goliat discovery and about 55 Km east of Snøhvit Field (Fig. 1.3), all found in the Hammerfest

basin. Water depth in the area is just over 400 meters. As observed from the well location map (Fig. 1.4), not all of the wells used on this study are found on this prospect. Table 1.1 presents some detail statistics of the prospect as given by the Norwegian Petroleum Directorate (NPD, 2011).

Table. 1.1 Detail field statistics. (Source: NPD. 2011)

Production License	**110 B**
Operator	Statoil AS
Discovery well bore	7122/6-1
Well bore contents	Gas and Condensate
Block	7122
NPDID	45068
Current activity status	Development likely but not clarified
Discover year	1987
Resource class	5 F
Recoverable reserves	Oil: 0.00 (mill Sm3)
	Gas: 7.39 (bill Sm3)
	NGL: 0.00 (mill tonn)
	Condensate: 1.00 (mill Sm3)

1.6 Materials and Methods

1.6.1 Database

A suite of well logs and published and unpublished compaction trends of natural and artificial sediments are used to investigate compaction and rock properties behaviour and AVO modeling of reservoir horizons.

- **Well logs**

  Petrophysical logs from wells 7122/2-1, 7122/6-1, 7122/6-2, 7123/4-1S, 7123/4-1A (side track) and 7122/4-1 are used (Fig. 1.4). These logs are quality controlled for problems such as those related to poor borehole conditions and errors in recording the log as sets out in the logging program found in the well prognosis. These wireline logs include: P- and S- wave velocity (m/s) logs, bulk density (g/cc), gamma ray (API) and neutron porosity (fraction).

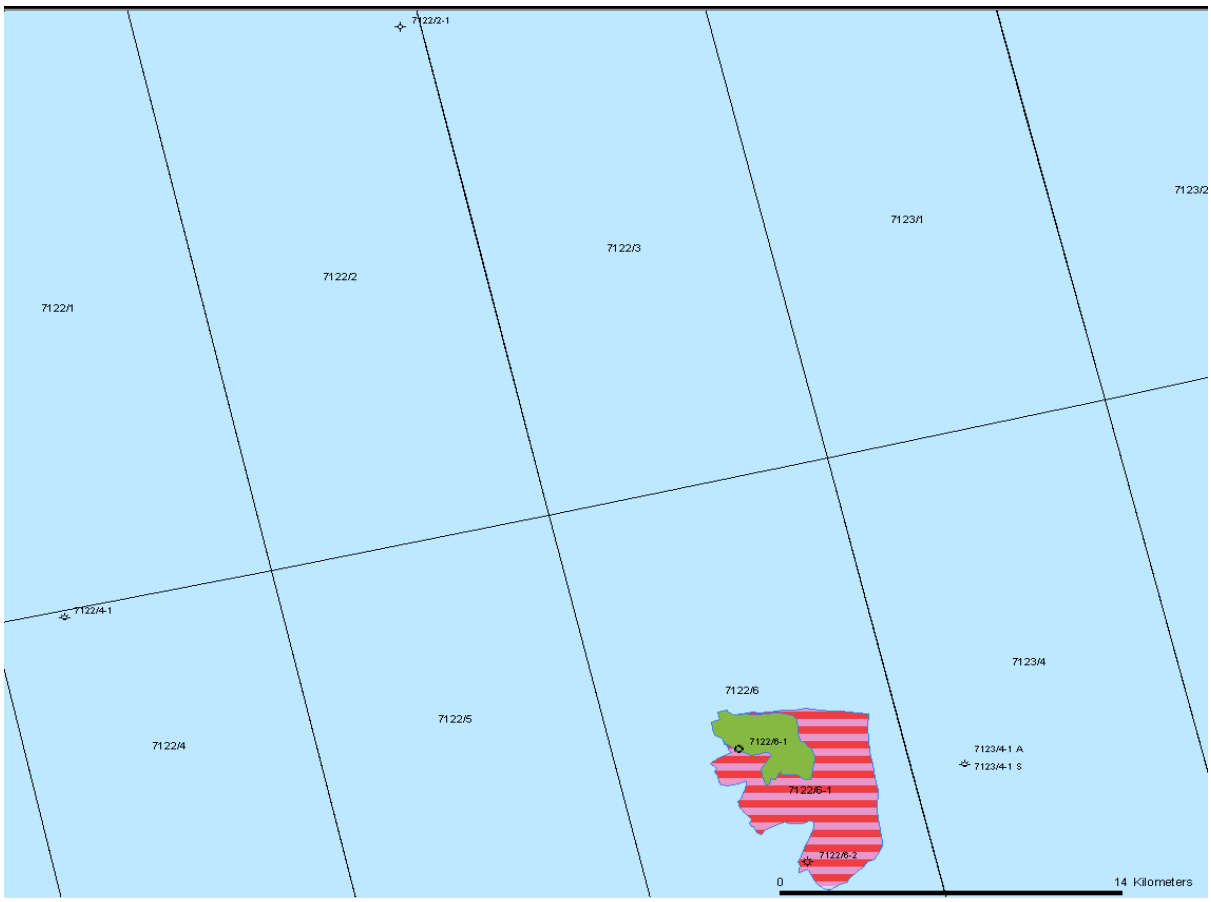

Fig. 1.4 Well bore location map of the study area across the Tornerose prospect.

Wells 7122/2-1, 7122/6-1, 7122/6-2, 7123/4-1S, 7123/4-1A was drilled to prove the presence of additional hydrocarbon reserves in the Tornerose prospect. However the objective of well 7122/4-1 was to test the Åsgard prospect with the primary target being the Middle – Lower Jurassic sandstones of the Stø Formation.

- **Published and Unpublished Experimental Compaction Curves of Synthetic Samples**

Mondol., (2011) (Personal communication): Vp/ Density/ Porosity versus stress/ depth trend of a silt – clay. This data set is derived from an experimentally compacted mixture of Kaolinite – Silt with a 50:50 percent proportion giving a credible mineralogical and textural control such as the effects of grain size on effective packing, on the compacting sediment.

Mondol et al., (2007): Laboratory compaction trends of brine – saturated Kaolinite – Smectite (80:20) and 100% Kaolinite mixtures. The synthetic mudstones are considered as a non-uniform rock type having a specific clay mineralogical composition and grain size.
A constant conversion factor of 10 MPa vertical effective stress per kilometre of burial depth is used to convert laboratory measurements of effective stress to its vertical depth equivalents.
Marcussen et al., (2010): Velocity – depth trend obtained from sub-arkosic to quartzite sandstones with moderate amounts of detrital clays from the Etive Formation in the Northern North Sea.

- **Published Compaction Trends of Natural Sediments**

The following published trends on naturally compacted sediments are also use for comparative analysis:
Japsen (1999): linear velocity – depth trend as a function effective stress for marine shales dominated by Smectite – illite and mainly sensitive to overpressures. Vp (m/s) is given by the following equation:

$$Vp = \frac{10^6}{\left(460\, e^{-\frac{Z}{2175}} + 185\right)} \qquad \text{(Eq. 1.1)}$$

Where Z is the depth (m)

Storvoll et al., (2005): is a first order trend line representing a simplified linear velocity – depth function obtained from velocity data representative of sediments from Loppa High, Nordkapp, Hammerfest and Tromsø basins. It is expressed as:

$$Z = 1.76\, Vp - 2600 \qquad \text{(Eq. 1.2)}$$

Where Z = Depth (m), Vp = P-wave velocity (m/s)

1.6.2 Software

The following applications within the Hampson – Russell software are used;

- **Geoview**

It serves as a starting point of any Hampson – Russell program. Well log data are loaded into Geoview well database through the Well Explorer. This application basically used for two purposes:

(1) It acts as a well log database which can be accessed seamlessly by all other Hampson – Russell applications that use well logs for analysis. Here, well logs are displayed, check shot correction are made, synthetics are generated, wireline logs are also edited and manipulated in Geoview through the elog application. Stratigraphic sections across sections across multiple wells using a specific log type are equally done in Geoview.

(2) Secondly, it serves as a platform from which other Hampson – Russell applications relevant to this study such as Elog and AVO can be launched and are automatically connected to created well log database.

- **Elog**

A well log editing and modeling tool embedded within the Hampson-Russel software suite of applications. It is started from Geoview and used to edit and average logs. Cross plots are also made here and zones of interest defined on the cross plots that can be projected back onto the input logs to visualize its equivalent depth. Necessary log transforms are also done using elog to create different non-existent logs from several empirical relationships with other input logs.

- **AVO**

It is also launched from Geoview. This application is made up of two components: AVO modeling and AVO analysis. AVO modeling has the log editing and manipulating capabilities as elog. This a comprehensive modeling tool used to analyze pre – stack seismic data for evaluating AVO anomalies with input data such as a combination of different log types and synthetic NMO (Normal Move Out) corrected CDP (Common Depth Point) gathers. The pore fluid contents of both the Stø and Snadd reservoir sands are also evaluated through a combination of visual, analytical and modeling processes. Fluid replacement modeling (FRM) based on the Biot – Gassmann equations are also done using this application.

1.6.3 Methods

An introduction to different approaches to achieving the objectives of this research is presented in two folds. However, a more detail methodology with respect to each of the major targets is clearly outlined within each chapter.

- **Compaction and Evolution of Rock Properties**

A combination of techniques will be employed on entire well data to precisely evaluate how dynamic rock properties vary across the field by determining the main compaction mechanisms responsible for these changes with increasing burial depth. With this regard, all the available well data will be analyzed on individual basis. These wireline logs will also be cross plotted to further study some of the major controls on these compaction mechanisms. The entire dataset will be corrected for Cenozoic exhumation and experimental synthetic mudstone compaction curves will then be used to constrain the natural samples.

- **AVO (Amplitude versus Offset) Modeling**

Reflectivity as a function of offset/ angle will be evaluated at the top of the two main reservoir horizons. A wavelet is a key component in modeling. A zero phase Ricker wavelet is used to create and analyze pre-stack synthetics. Generating NMO corrected synthetics is based on the Zoeppritz equations. The main input log types used are upscaled density, P- and S-wave velocity. That is, changes in reservoir pore fluid properties and saturations are modeled. However the AVO modeling is first performed to determine what type of AVO anomaly may be anticipated then a suite of different pore fluid scenarios is also modeled. The effects of these pore fluids and their saturations on AVO response is then investigated through a sensitivity analysis. The implications of cap rock geology, depth and lithology are also investigated.

CHAPTER 2: REGIONAL GEOLOGICAL FRAMEWORK

2.1 Structure and Tectonics

The Barents Sea region has an intracratonic setting with a complex mosaic of basins and platforms. It has undergone several phases of tectonic deformation since the Caledonian Orogenic movements ended in Early Devonian times (Gabrielsen et al., 1990). Structurally, the Barents Sea continental shelf is dominated by NE - SW trending faults, with a few WNW – ESE striking faults. In the southern parts, a zone dominated by ENE- WSW trends is defined by the major fault complexes bordering the Hammerfest and Nordkapp Basin (Fig. 2.1). The western parts of the Barents Sea have been the tectonically most active region throughout the Cenozoic and Mesozoic times (Gabrielsen et al., 1990).

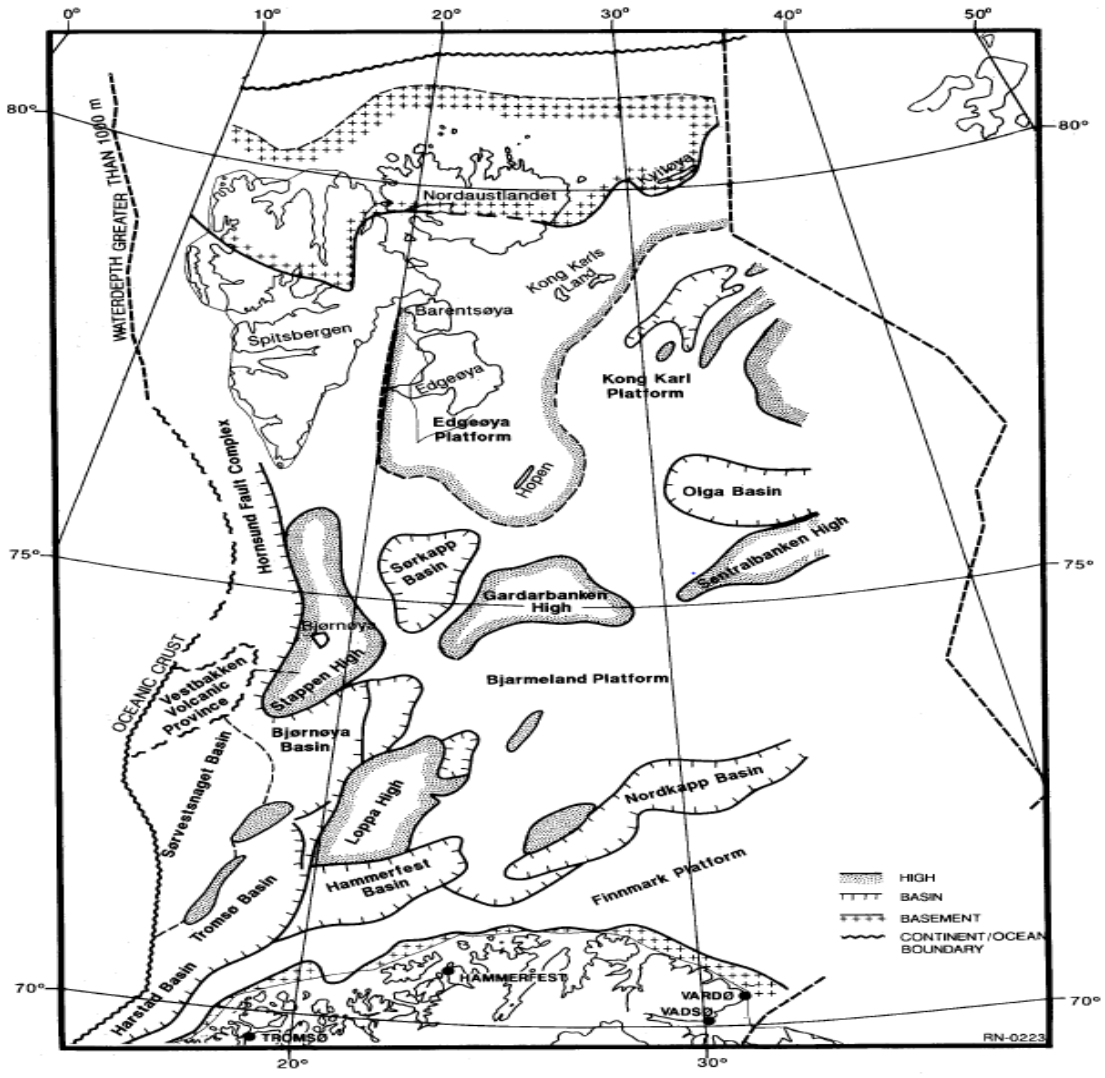

Fig. 2.1 Tectonic framework of the entire Barents Sea region. Source: Gabrielsen et al. (1990).

The Barents Sea is divided into three main geological provinces bounded by major fault zones; based on sedimentary infill, structural style and crustal structure (Gabrielsen et al., 1990). These are; (1) the oceanic Lofoten Basin formed during the opening of the Norwegian- Greenland sea and the Vestbakken Volcanic Provinces in the west; (2) the south-western Barents Sea basin province which is made up of deep Cretaceous and early Tertiary basins such as Harstad, Tromsø, Bjørnøya and Sorvestsnaget Basins; and (3) the eastern region made up of Mesozoic Basins and Highs which remained relatively inactive during the Cretaceous – Tertiary subsidence; these are: Finnmark Platform, Hammerfest Basin, Loppa High and Fingerdjupet subbasin.(Faleide et al., 1993)

The entire area had undergone several episodes of uplift and erosion. However three main phases of uplift have been roughly identified (Ohm et al., 2008) to have occurred at 60 (Paleocene), 33 (Oligocene) and 5 Ma (Pliocene – Pleistocene) with the first two episodes being most significant (Japsen and Chalmers, 2000) (Fig. 2.2). In most published uplift maps of the area, there is no uplift in the western parts and generally increases eastwards, culminating in around the Bjarmeland Platform area and decreases further eastwards. Based on available literature, the major mechanisms of these late Cenozoic events are thought to be: emplacement of magma at the base of the crust leading to isostatic uplift, flow of asthenospheric material into active diapirs, isostacy associated with glacial erosion, phase changes in the lithosphere due to pressure relief and regional compression of the lithosphere (Japsen and Chalmers, 2000).

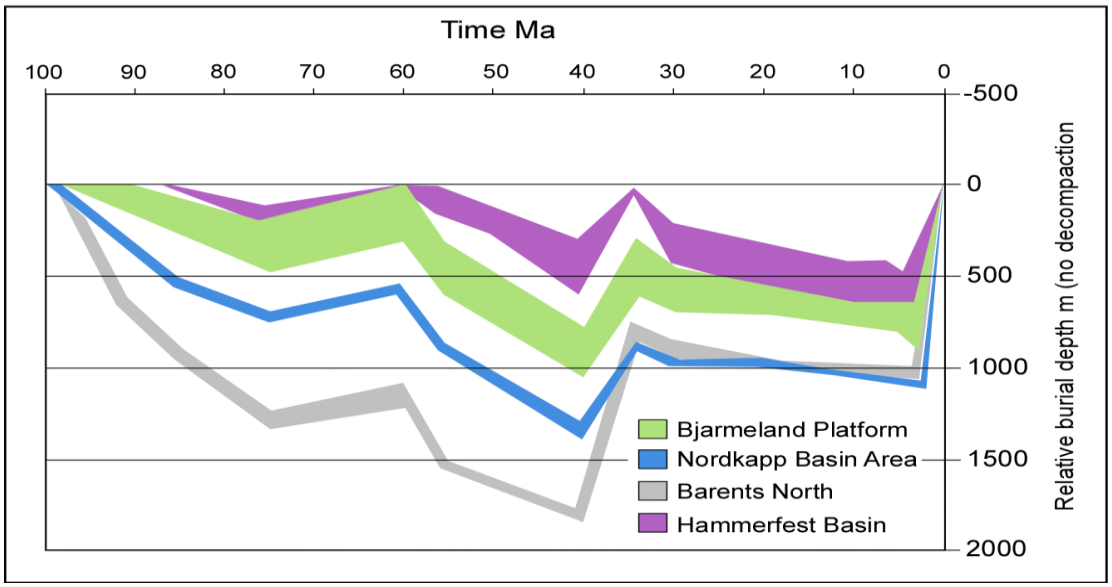

Fig. 2.2. Subsidence curves for different parts of the Norwegian Barents Sea. Three major uplift and erosion episodes are indicated to occur at 60 Ma, 35 Ma and recent. Source: Ohm et al. (2008).

2.2 Stratigraphy

A total of six wells were drilled across the study area and the deepest one is 7122/6-2 with a depth of about 2639m below sea floor (BSF) (Table 2.1). The oldest penetrated formation is the kobbe Formation of mid Triassic age (Fig. 2.3).

Table 2.1. Stratigraphic statistics of five wells across the study area. Source: (NPD, 2011)

Well bore	Total Depth (m) BSF	Oldest penetrated Formation	Age
7123/4-1A	2419	Snadd FM	Late Triassic
7122/6-1	2283	Snadd FM	Middle Triassic
7122/6-2	2639	Kobbe FM	Middle Triassic
7122/4-1	2647	Snadd FM	Late Triassic
7122/2-1	1734	Stø FM	Middle Jurassic

The main sources of sediment input in the area appeared to be the Baltic Shield in the South, the Uralides and Novaya Zemlya to the east (Mørk, 1999). The following Groups are encountered in the area: the Kapp Toscana, Adventdalen, Nygrunnen, Sotbakken and Nordland Groups (Fig. 2.3).

2.2.1 Nordland Group

Only the youngest parts of the group are encountered in this area and across most parts of the Hammerfest Basin. Sands and clays grade into sandstones and claystones. The sand content increases upward. The group has the sea bed as the upper boundary. The sediments are of Late Pliocene to Pleistocene/ Holocene. Depositional environment is characterized by bathyal to glacial marine (Dallan et al., 1988).

2.2.2 Sotbakken Group

The Torsk Formation represents the only recognizable subdivision within this group. The entire group shows a general increase in thickness from the southern margins of the Hammerfest Basin to the south west across the study area. The group is dominated by claystones, minor siltstones, tuffaceous and carbonate horizons. The younger sequences of the group are less preserved due to erosion resulting from Mid Oligocene tectonic activity. Preserved sequences suggest a Late Paleocene to Early / Mid Eocene age.

(Dallan et al., 1988). The claystones were deposited in an outer sub littoral to deep shelf environment following a regional transgression across the Barents Shelf.

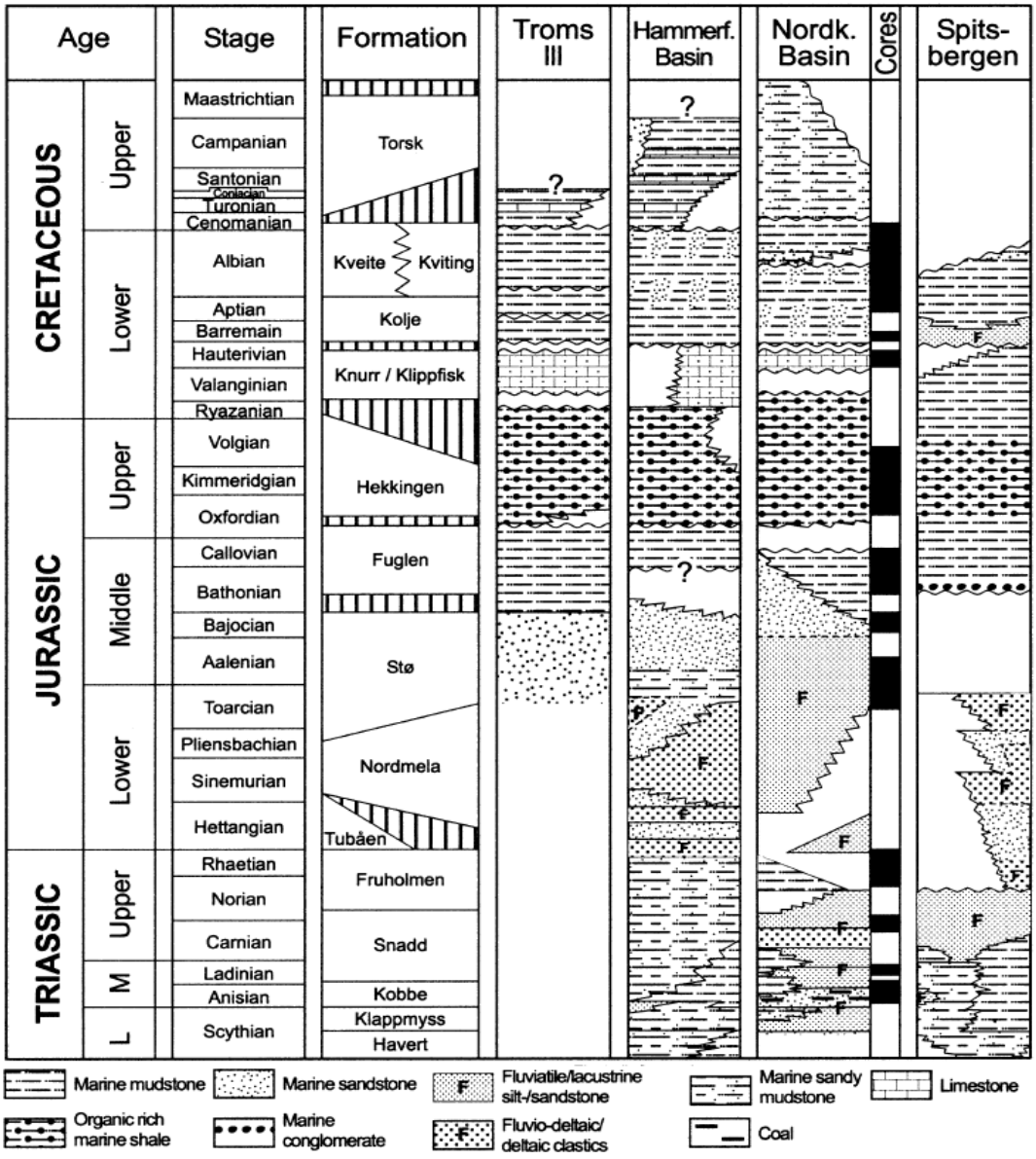

Fig. *2.3 Schematic illustration of Barents Shelf and Spitsbergen lithostratigraphic column. Formation definition is by Worsley et al.(1988). Source: Bugge et al. (2002)*

2.2.3 Nygrunnen Group

Two subdivisions of this group are the Kviting and Kveite Formations. The age of the group spans from Cenomanian to Maastrichtian. Lithologically, they consist of grey claystones with thin limestones intervals. The entire sequence thins eastward across the Hammerfest Basin where condensed calcareous sandy units reveal intermittent deposition principally

during times of maximum transgression.(Worsley, 2008).The claystones are generally attributed to the Kveite Formation while the condensed sequences to the Kviting Formation.

2.2.4 Adventdalen Group

This comprises; shales, siltstones and sandstones as well as condensed carbonate beds of late Jurassic to Early Cretaceous period. During the Late Cretaceous uplift, this group was eroded to varying extents leading to a hiatus comprising only the Cenomanian and Turonian. Subdivisions include the Hekkingen, Knurr, Kolje, kolmule, and Fuglen Formations. Regional transgressions led to cut-off of coarser clastic supply and favoured the deposition of fine grain deep marine black paper shales of the Hekkingen Formation. They represent excellent source rocks for oil and gas in the area with a total organic content of about 20% (Worsley, 2008). The sandstones represent deltaic progradation and shelf environments whereas the coeval condensed limestone interval grades into marls and calcareous mudstones.

2.2.5 Kapp Toscana Group

This Group spans from the Ladinian to Bathonian age. The Stø and Snadd Formations belong to this Group. Other subdivisions are Tubåen, Nordmela, and Fruholmen Formations. These comprise of shales and siltstones and grades upward to the immature sandstones of the Storfjorden subgroup (Dallmann., W. K (1999).

The Kapp Toscana Group has been deposited in a generally near shore deltaic environment. Is it characterised by coastal and marine reworking (Mørk et al., 1982).

These channel and coastal sands were transported from mature provenance areas and their primary reservoir qualities were enhanced during reworking over periods of high stand. The Novaya Zemlya was a significant provenance area (Worsley, 2008). However it was observed that sandstones throughout the region show a convergence of lithologies upward in the sequence, probably reflecting increasing marine reworking and mixing of sediments from multiple provenance area (Riis et al., 2008, Mørk, 1999).Triassic sedimentation was characterised by transgressive\ regressive sequences that were regionally synchronous. Nonetheless, increasing tectonic activity led to a disruption of these sequences (Smelror et al., 2001).

2.3 Petroleum System

A petroleum system describes an orderly sequence (Perrodon, 1992), of natural genetic interplay between a pod of active source rock(s) and all the related oil and gas accumulations. This encompasses all the required elements and processes necessary for existence of these accumulations (Peters and Casa., 1994). The required elements are an active source rock, a reservoir rock, adequate seal (cap rock) and an overburden rock. The processes are summarized as; trap formation, generation of petroleum from kerogen found in organic matter within the source rock(s), subsequent migration along defined pathways and eventual accumulation in a reservoir rock. Petroleum can be re-migrated and accumulated in a reservoir rock that was deposited after accumulation in a previous system practically due to the singular or combined effects of folding, faulting, uplift and erosion. However the critical moment will define the highest probability of entrapment and preservation of petroleum after generation and migration. A play can thus be defined as a group of prospects (potential field sites) and any known related fields having common petroleum sources, migration relationships, reservoir Formations, seals and trap types (White, 1993). According to this definition, in the absence of generated petroleum, there is no prospect.

2.3.1 Source Rocks

The Barents Sea has multiple source rocks, however that which is of particular interest is the Hekkingen Formation of the Adventdalen Group. The Hekkingen Formation is an effective source rock by virtue of its generation and expulsion of petroleum. It is often considered as an equivalent of the Kimmeridge shales in the North Sea. The Hekkingen Formation has a dual – member division consisting of the Lower Alge and the upper Krill member. The Alge member shows extremely high gamma ray values in all five wells and consist of black paper shales in an organic rich material (Fig. 2.4).

The regional Hekkingen Formation with a high Total Organic Content (TOC) of 10 to 15% and high Hydrogen Index of 280 to 350 mg HC/g (NPD Factpage. 2011), imply a very good source rock. The organic matter is of mixed terestrial and marine origin with kerogen type II and III (Ohm et al., 2008). This variation in kerogen type probably inidcates distance to the paleocoastline and terrigeneous inputs coupled with variations in anoxia in the early diagenetic environment (Ohm et al., 2008).

Fig. 2.4. Core photograph of the Hekkingen Formation from well 7228/9-1S. Source: NPD Factpage (2011).

Vitrinite reflectance (R_o) of 0.6% and T_{max} of 435° C (NPD Factpage. 2011) indicates that the well 7123/4-1A probably just enters the oil window at around 1650m BSF, around where the best source rocks are found. However, these organic rich shales have not attained their full hydrocarbon genereation potential due to maturity problems resulting from the negetive consiquences of uplift (Ohm et al., 2008).

The presence of oil and gas shows in some of the wells is a good indication of an active source rock. The occurance of multiple active source rock intervals (Fig. 2.5) from the Triassic to Upper Jurassic with hydrocarbon generation having occured over long geologic time scale has led to the Barents Sea area being described as an overfilled petroleum system (Ohm et al., 2008) however the effects of uplift changes the story.

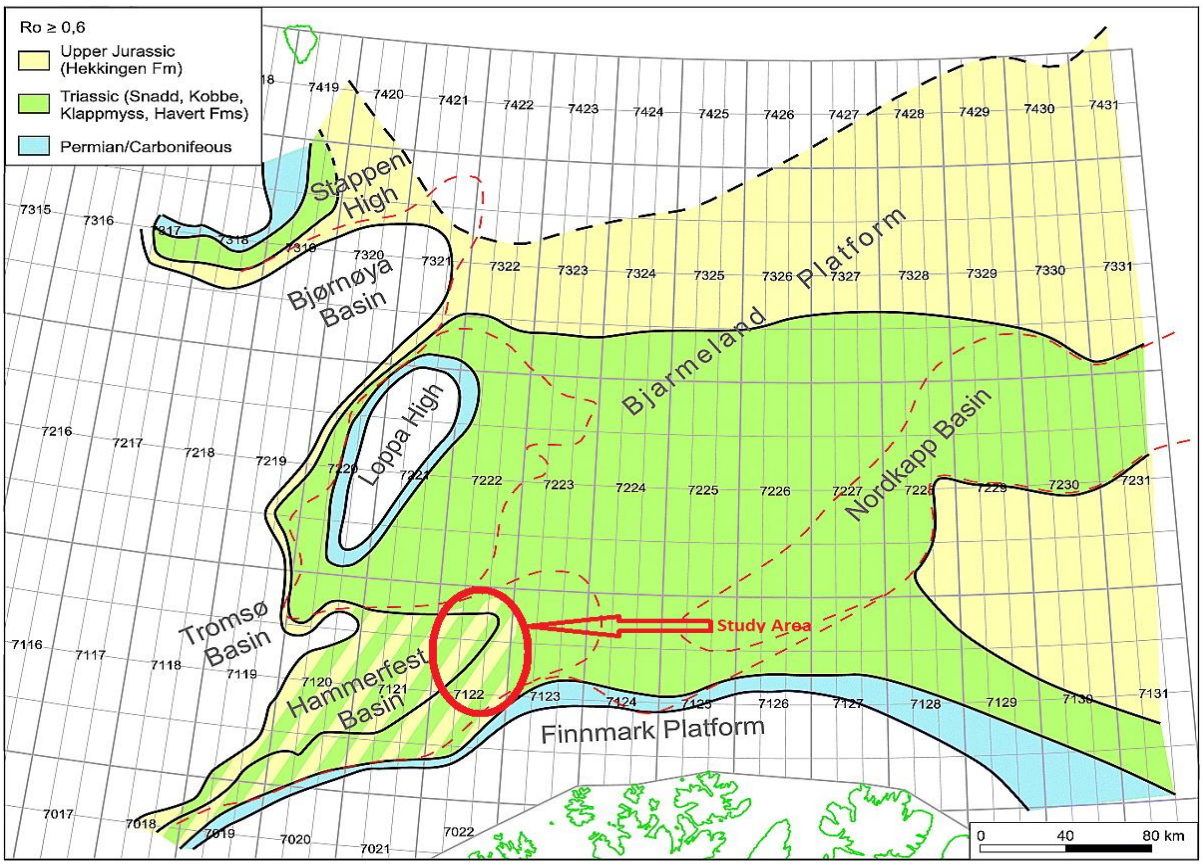

Fig. 2.5. Tentative maturity map depicting oil maturity distribution of Permian, Triassic and Jurassic source rocks. This map is based on maturity data from wells in the area, semi-regional maturity trends of vitrinite reflectance (Ro) versus depth. . The study area is highlighted by the solid red circle showing the occurrence of multiple source rock. Modified after: Ohm et al., (2008).

2.3.2 Studied Reservoir Units

The principal reservoirs of the field lie in the Stø Formation, which is of Pleinsbachian to Bajocian stage and the much older Snadd formation, of Ladinian to Early Norian Stage. Both reservoir units are part of the Kapp Toscana Group.

2.3.2.1 Stø Reservoir

This represents the upper/ shallower reservoir unit of the field. It was penetrated in all six studied wells. A maximum thickness of about 59m was reached in the well 7122/4-1 at a depth of about 2326m along the Hammerfest basin axis and generally thins out towards the east with thicknesses of 40m in well 7123/4-1A and 23m in well 7122/6-1. An apparently diachronous base is observed younging from east to west across the Hammerfest basin (Dallan et al., 1988).

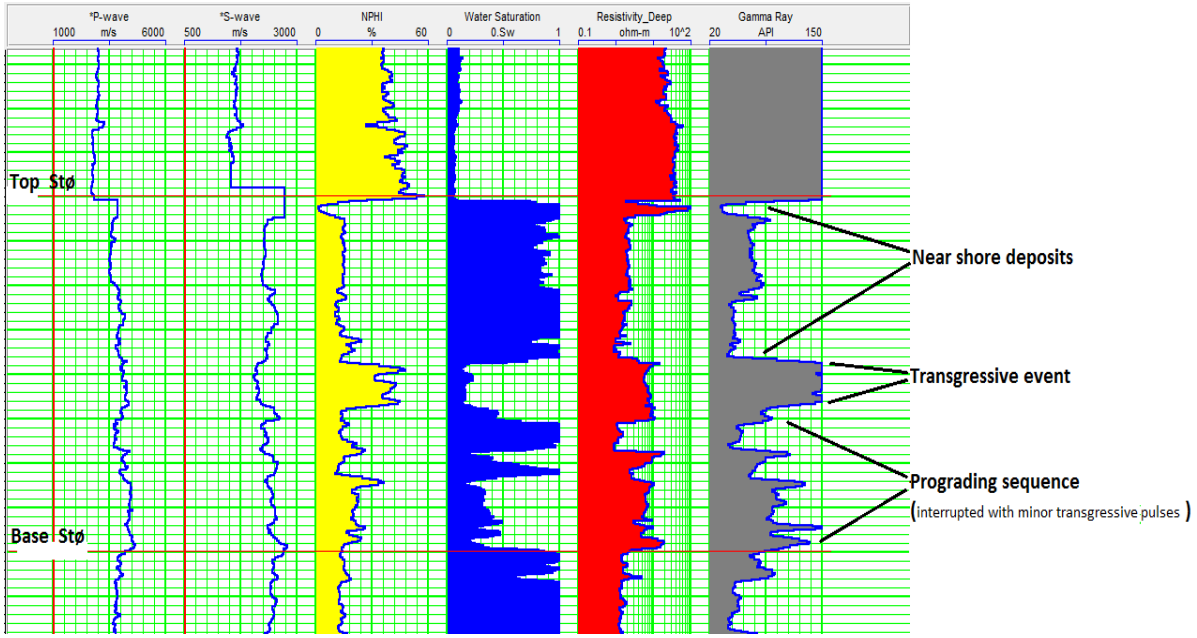

Fig. 2.6 Wireline log character across the Stø Reservoir from well 7123/4-1A. P-wave, S-wave, Neutron porosity, water saturation, resistivity and gamma ray logs respectively. Different depositional facies are clearly identified using the gamma ray log.

The early basal sequence is only present in the western region of the Hammerfest basin. The mid to late sequence represents a maximum transgressive pulse in the area. The upper-most Bajocian sequence is variable due to syn-depositional uplift and differential erosion (Dallan et al., 1988).

The Stø Formation consists dominantly of moderately to well-sorted mineralogically mature sandstones (Fig. 2.7). The porosity and permeability in these sandstones ranges between 19 – 35% and 30 – 3000 mD respectively (NPD Fact page 2011). The entire unit can be subdivided into three depositional sequences with each base defined by transgressive episodes (Fig. 2.6).

Sands of the Stø Formation were deposited in a prograding coastal environment. The depositional environment is interpreted as such on the basis of palynomorphs and trace fossils, with deposition just below the fair weather wave base in a lower shoreface to offshore transition zone (Smelror et al., 2001). Primary sedimentary structures such as current ripple lamination, trough cross beddings and horizontal lamination are common (Fig. 2.7).

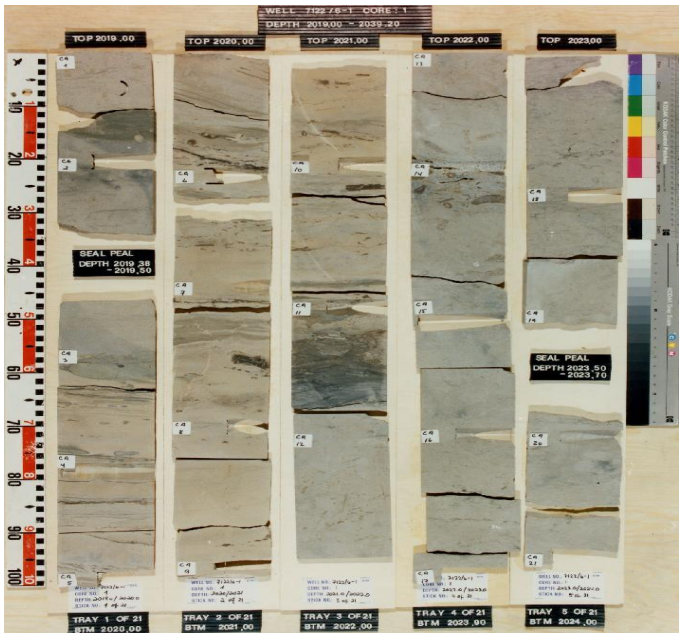

Fig. 2.7 Core photograph obtained around the top of Stø reservoir sandstones from well 7122/6-1 with a core start depth of 1595m BSF and end depth of 1599 m BSF. These sands are quite prolific with excellent reservoir qualities. Source: NPD Factpage (2011).

2.3.2.2 Snadd Reservoir

This represents the deeper reservoir unit. It was penetrated by all studied wells except in the well 7122/2-1. A Ladinian to Early Norian age is suggested (Dallan et al., 1988, Bugge et al. 2002). The considered sandstone unit for this study is found at the very top of the Formation and is water wet (Fig. 2.8).

The Snadd Formation consists of basal grey shales which coarsen up to shales with inter-beds of grey siltstones and sandstones at the top of the formation with laminations and hummocky bedding in the fine grained turbiditic sandstones (Fig. 2.9) (Bugge et al. 2002). Sparse but upward increasing bioturbation in both sequences as well as trace fossils are indicative of open marine environments (Dallan et al., 1988). This is a result of a major transgressive period which submerged most of the Structural Highs and Platforms in the area. Storm derived silts and sands from southern sources such as the Baltic shield are indicated. On the other hand the Carnian sequence represents large scale progradation of deltaic systems over the entire Hammerfest basin given by the motif of two upward coarsening sequences (Riis et al., 2008). This Formation distinguishes itself from overlying Formations in terms of palaeogeographic controls on sedimentation patterns, probably reflecting up doming of the northern shelf margins (Dallan et al., 1988)

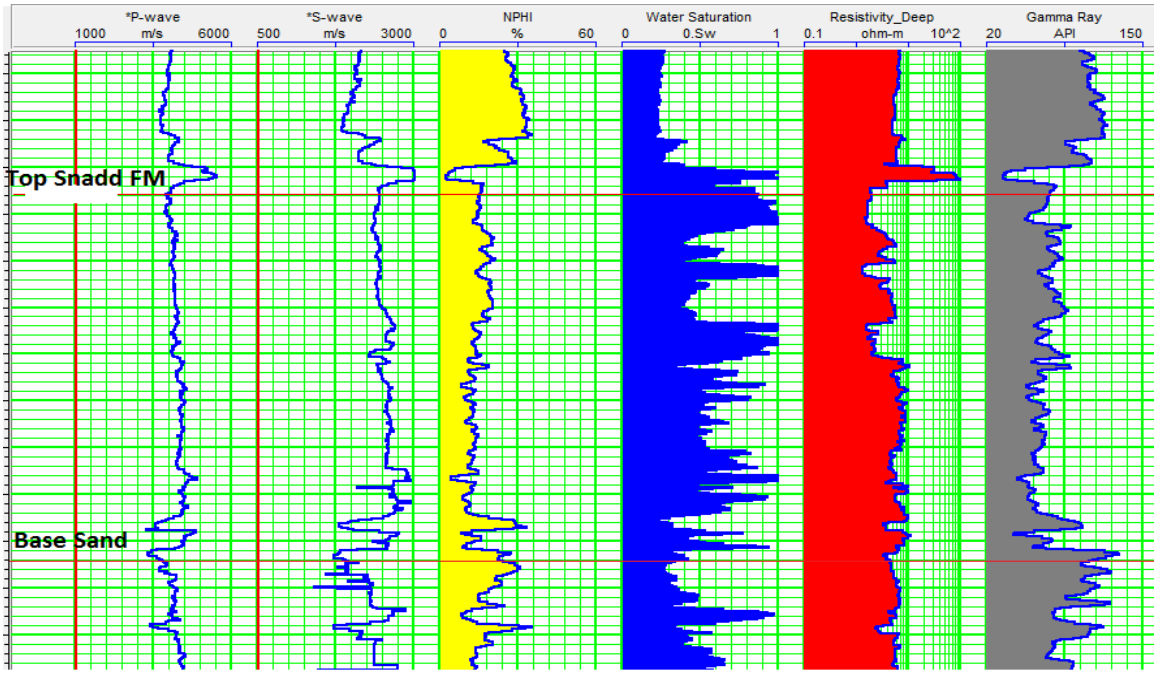

Fig. 2.8 Wireline log responses across the studied Snadd reservoir sand unit found at the top of the Formation from well 7123/4-1A. P-wave, S-wave, Neutron porosity, water saturation, resistivity and gamma ray logs respectively.

Reservoir sands of this Formation are feldspathic to lithic arenites (Polyaeva. 2011). They have a very high susceptibility to diagenetic alterations by virtue of primary depositional variations in grain size, matrix and high feldspar content. These sands are quartz cemented with highly variable but generally poor reservoir qualities, exhibiting a wide range of elastic properties. The low porosity could also be accounted by the probable presence of clay material filling the voids between the quartz grains.

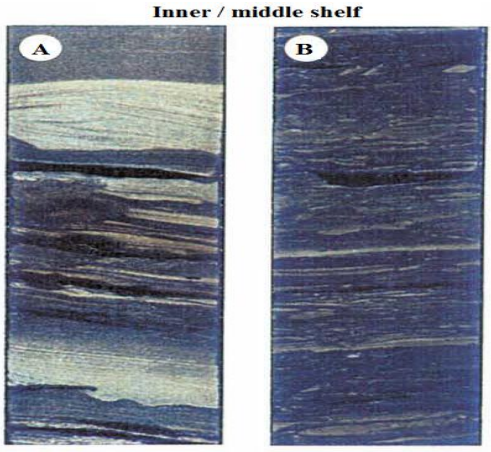

Fig. 2.9 Modified core photo of the Ladinian Snadd Formation from at two different depths from (a) well 7230/05-U-04 AT 64.2m and (b) from well 7230/05-U-04 at 60.7m. Modified after: Bugge et al. (2002).

2.3.3 Trap

Not all well bores used in this study penetrates the Tornerose prospect (Fig. 2.10) though all of them encountered both the Stø and Snadd reservoir units at different locations and depth across the field. The Tornerose prospect is found on one of the relatively positive elements along the Hammerfest basin. This structure is a southward dipping rotated fault block forming a structural closure with the north-eastern side delineated by a major NW-SE striking fault (Fig. 2.10). Hence the trap mechanism can be characterised as a structural trap with a throw of about ± 280m estimated from displaced Formation tops between the wells 7122/4-1 and the well 7122/6-1. On the Åsgard prospect, the trap was formed by a large tilted horst structure dipping towards the North – Northwest. Well 7122/4 – 1 was the first well on prospect. The Stø reservoir is however water wet throughout the study area, across different faulted segments, thereby casting doubt on the sealing capacity of the faults at this depth level.

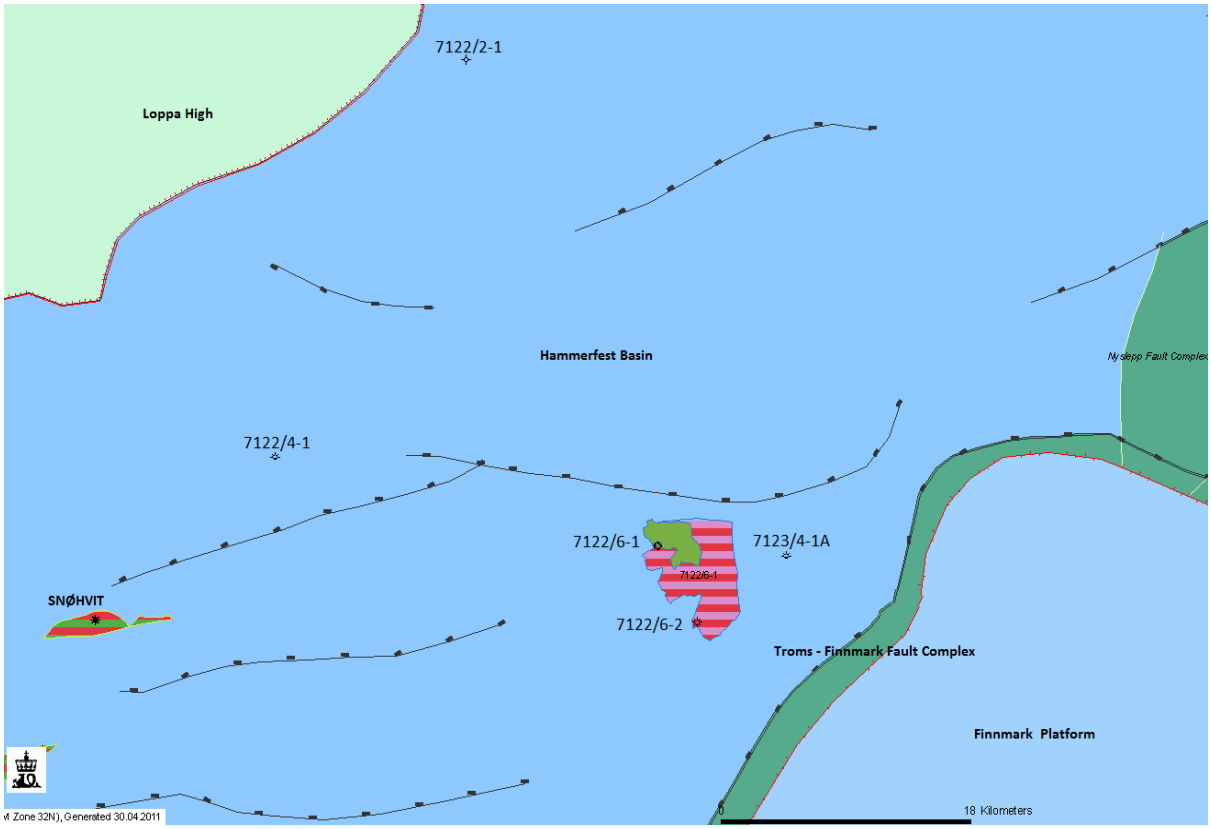

Fig. 2.10 Structural map of the study area illustrating the trap style of the Tornerose prospect on the rotated fault block. Source: NPD Factmaps., (2011).

CHAPTER 3: COMPACTION AND EVOLUTION OF ROCK PROPERTIES

3.1 Introduction

Sedimentary rocks continuously undergo physical and chemical changes as a function of burial depth, temperature and geologic time (low strain rates), also important hydro-mechanical parameters change during burial, erosion and uplift (Bjørlykke et al., 2004, Walderhaug et al., 2001). In a well defined sediment composition, the velocity and density increase with depth (decreasing porosity) in response to compaction processes. Compaction in sedimentary basins involves both mechanical and chemical compaction (Fig. 3.1).

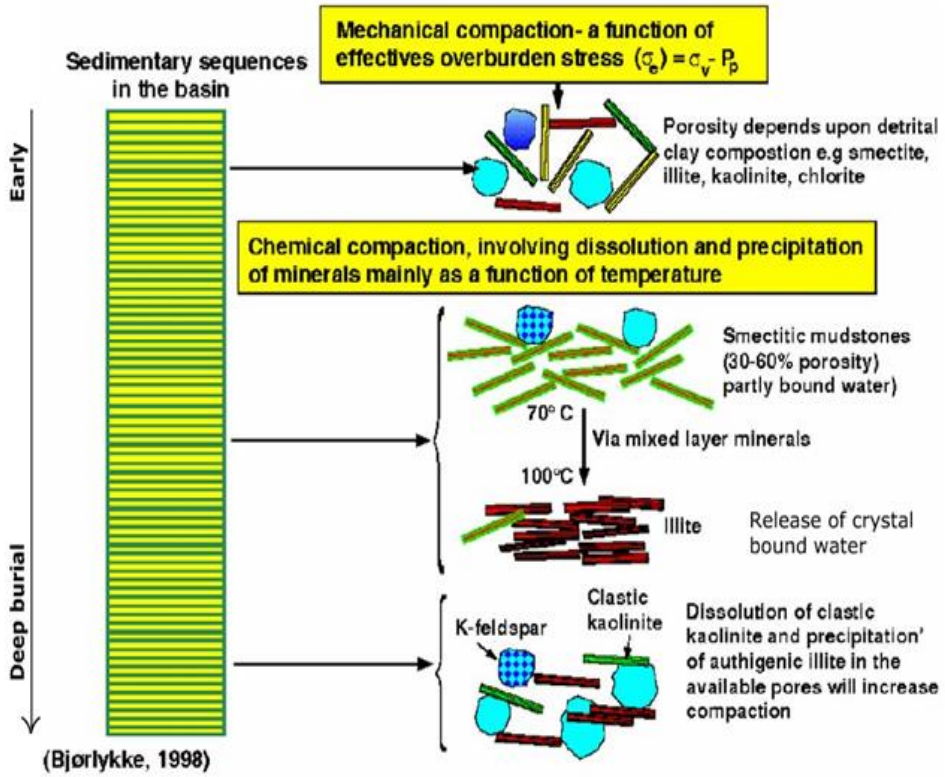

Fig. 3.1 Principal aspects of sediment compaction. With increasing burial depth, sediments are subjected to changes in physical properties as a function of increasing stress and temperature. Source: Bjørlykke (1998).

In some basins the transition from mechanical compaction domain to chemical compaction domain can be gradual while in others it is more or less distinct (Fig. 3.2). Both domains are fundamentally controlled by well defined compaction laws (Bjørkum et al., 1998, Bjørlykke

et al., 1989). Compaction will therefore ultimately lead to a more stable grain frame work and a significant change in elastic properties.

Mechanical compaction follows a sequential processes (Waples and Couples, 1998) which can broadly be separated into four steps: (a) applied load (sedimentation) to a system of sediments and pores, (b) deformation of grain framework and slight porosity reduction (c) increase in pore pressure due to reduction of pore space (d) slightly overpressured pore fluids flow to sites of lower potential energy (if possible). The changes in rock properties as a function of increasing burial depth are largely due to several diagenetic processes which are very much dependent on the primary sediment composition which reflects the textural and mineralogical composition pertaining to a particular sedimentary environment (Bjørlykke et al., 2004).

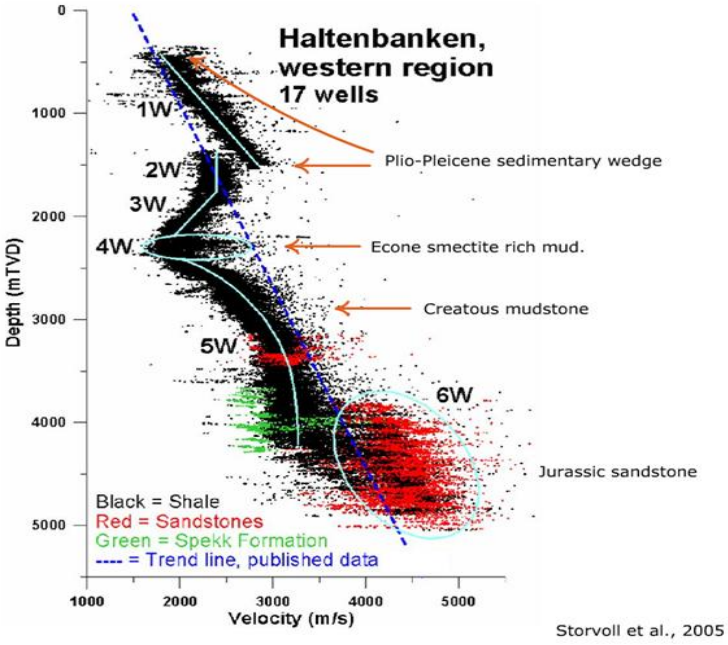

Fig. 3.2 Sonic velocity measurements (every 0.5 – 0.7m with depth) from seventeen wells located in the western region in of the Haltenbanken area- Norwegian North Sea after Storvoll et al. (2005). The estimated trend line (dashed blue line) will be used for comparism with well data from this study area

This chapter focuses on determining the different compaction mechanisms and the transition between the different compaction domains. The major controlling parameters within each of these domains will also be investigated as well as accurately defining good reservoir intervals. Given the burial history of the area, the sediments will be corrected for Cenozoic exhumation after which the experimental and published compaction curves will be used to constrain sediment compaction in the area.

3.2 Theoretical Background

3.2.1 Mechanical Compaction

Mechanical compaction starts immediately after deposition and is mainly a function of the vertical effective stress resulting in an increased stress at grain contacts and thus increased rigidity. It predominates at shallow depth down to 2 – 4 Km depending on the geothermal gradient of the area (Mondol et al., 2007) and involves rearrangement of the grain framework by sliding, orientation and grain breakage. The weight of the sediments making up the overburden including the weight of the fluids in the pore spaces produces a vertical stress. For a given sedimentary basin with minimal lateral lithologic variations, the total vertical stress (lithostatic stress) can be calculated as follows:

$$\sigma_v = \rho s\, gh \qquad \text{(Eq. 3.1)}$$

Where: σv is the total vertical stress, ρs is the average bulk density of overburden sediments, g is the gravitational force and h is thickness of the overburden sediments.

The effective vertical stress, denoted σv′, plays a very critical role in mechanical compaction of sediments with minimal chemical compaction. It is also known as average inter-granular stress by virtue of the fact that it is transmitted through the grain framework. Effective stress is the difference between the total vertical stress and the pore pressure and it increases linearly with depth (under hydrostatic pore pressure conditions):

$$\sigma v' = \sigma v - u \qquad \text{(Eq. 3.2)}$$

Where: σv′ is effective vertical stress, σv is total vertical stress and u is the pore pressure.

The effective vertical stress from the overburden is borne both by the pore pressure (fluid phase) and mineral grain frame work (solid phase) (Fig. 3.3). An increase in the pore pressures definitely reduces the vertical effective stress and hence mechanical compaction.

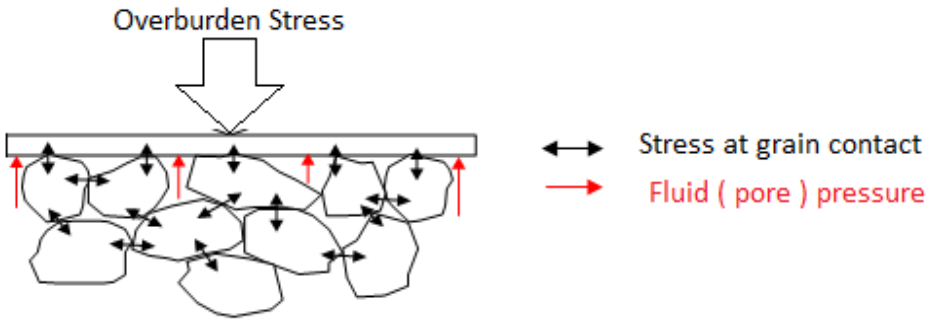

Fig. 3.3. Schematic illustration of the contributions of overburden stress, stress at grain contacts and pore pressure to mechanical compaction.

However, in a sedimentary basin with minimal or no lateral compression, horizontal stresses would be less than or equal to vertical stresses (Osborne and Swarbrick, 1999). As a result, lateral compression is liable to yield high pore pressures in thesame manner as vertical stress can cause overpressuring due to under-compaction.

Other controls on mechanical compaction are the mineralogical composition, grain size and the rate of fluid expulsion from the compacting sediments (Waples and Couples, 1998, Bjørlykke et al., 2004) (Fig. 3.4). The extent of mechanical compaction is important because, as well as increasing the mechanical stability of the sediments, it determines the inter-granular volume (IGV) which is the porosity at the onset of chemical compaction (Bjørlykke and Jahren. 2010).

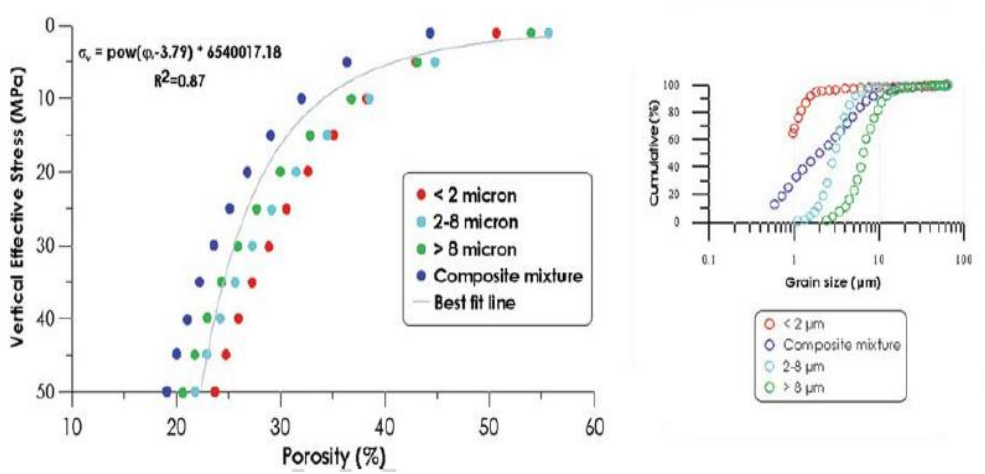

Fig. 3.4. Experimental mechanical compaction of brine-saturated kaolinite aggregates, sorted by grain size after Mondol et al. (2008a). Samples containing less than 2µm sized kaolinite aggregates retained higher porosity compared to all other mixtures. The maximum porosity reduction is observed in the composite mixtures containing all grain sizes, demonstrating the importance of grain size and sorting in determining rock properties.

3.2.2 Chemical Compaction

Chemical compaction usually occurs at deeper parts of sedimentary basins beyond the realm of mechanical compaction, where the reaction kinetics for clay and silicate minerals are extremely slow and therefore often negligible. In carbonate rocks, an important factor controlling compaction is rather the primary content and distribution of aragonite, causing early cementation at shallow depths and low temperature through complex interactions between stress and thermodynamics (Bjørlykke and Jahren., 2010)

In siliciclastic sediments, the solubility of silica seems to be dependent on the degree of entropy in the crystal lattice. At approximately 25°C (shallow depths), the solubility of quartz is 3 – 6 ppm, cristobalite and tridymite (Opal CT) is 6 – 15 ppm and amorphous silica (Opal A) is 150 ppm. Comparatively, silica has a low solubility and solubility gradient. When Opal A and Opal CT dissolve, pore water becomes supersaturated with respect to quartz and starts to crystallize at several nuclei forming authigenic quartz (with a much darker coloration reflecting its biogenic origin) (Bjørlykke and Jahren., 2010)

Chemical compaction involves a further modification of rock properties by dissolution of primary clastic minerals (or amorphous) material which is in disequilibrium and the precipitation of thermodynamically more stable mineral assemblages. These processes prevail at higher temperatures > 70°C – 80 °C, in a normally compacted basin (no overpressure) with a geothermal gradient of 35 – 40°C/Km ,which generally corresponds to depth of about 2.0 - 2.5 Km overburden (Mondol et al., 2007) and 20 – 25 MPa vertical effective stress. The rate of thermodynamic equilibrium is determined by the kinetics of mineral reaction which increases as an exponential function of temperature. As such, time, temperature, detrital mineralogy and texture constitute the major controls on chemical compaction (Bjørkum et al., 1998, Lander and Walderhaug, 1999, Murphy et al., 1989). Chemical compaction will continue even during basin inversion so long as the temperature remains above the maximum threshold for mechanical compaction (Bjørlykke and Jahren., 2010) as illustrated by Figure 3.5.

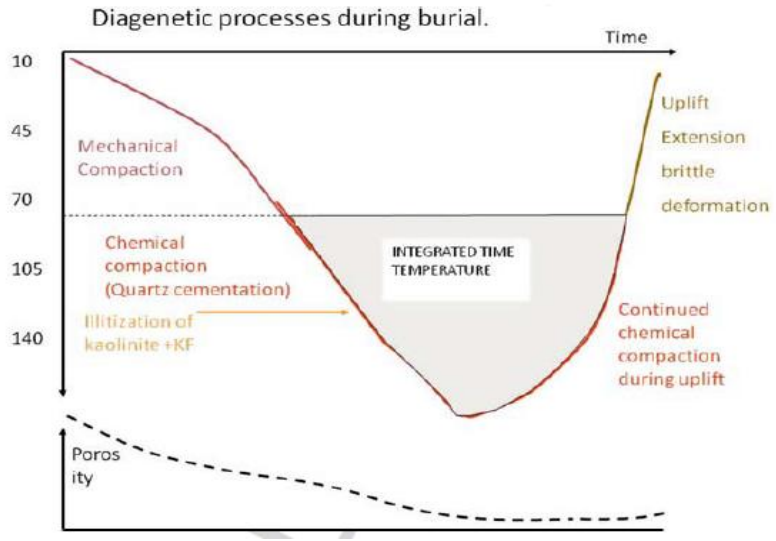

Fig. 3.5 Diagenetic processes, mainly quartz cementation as a function of temperature and time. Note that quartz cementation will continue also during uplift as long as the temperature exceeds 70–80°C. Source: Bjørlykke and Jahren (2010).

3.2.3 Compaction of Clays, Mudstones and Shales

Comprising approximately two thirds of the stratigraphic column, clays, mudstones and shales have very different physical properties depending on the composition of constituent clay minerals. Shale could basically be defined as a mixture of clay, silt and electrostatically bound water. The most common clay minerals are smectite (montmorillonite), illite, chlorite and kaolinite. As observed from experimental compaction of clays (Mondol et al., 2007), their compressibility and shear strength are a function of the salinity of the pore water and the complex interactions between the solid and the liquid phases (Meade, 1963).

Upon deposition, the mechanical compaction of clays is mostly a function of effective stress and involves the mechanical load bearing capacity of individual grains, grain size, pore pressure, pore aspect ratio, specific surface area, as well as surface charge (Djéran-Maigre et al., 1998, Meade, 1964, Grabowska-Olszewska, 2003).

Smectite being extremely fine grained (< 0.1μm) with a very large specific surface area (>120 m^2/g) and a cation exchange capacity ranging from 75 – 125 cmol/kg, has a lower compressibility, than the more coarse grain (>1-10μ) and smaller specific surface (5-30 m^2/g) of kaolinite (Mondol et al., 2007, Mondol, 2008a).

This is due to the lower force per unit area as the applied effective vertical stress is being distributed over its very large area resulting in a very low force per contact area. This difference in compaction as a function of mineralogy (provenance and depositional setting)

will evidently lead to variations in acoustic velocities and other petrophysical properties for a given applied effective stress (Fig.3.6).

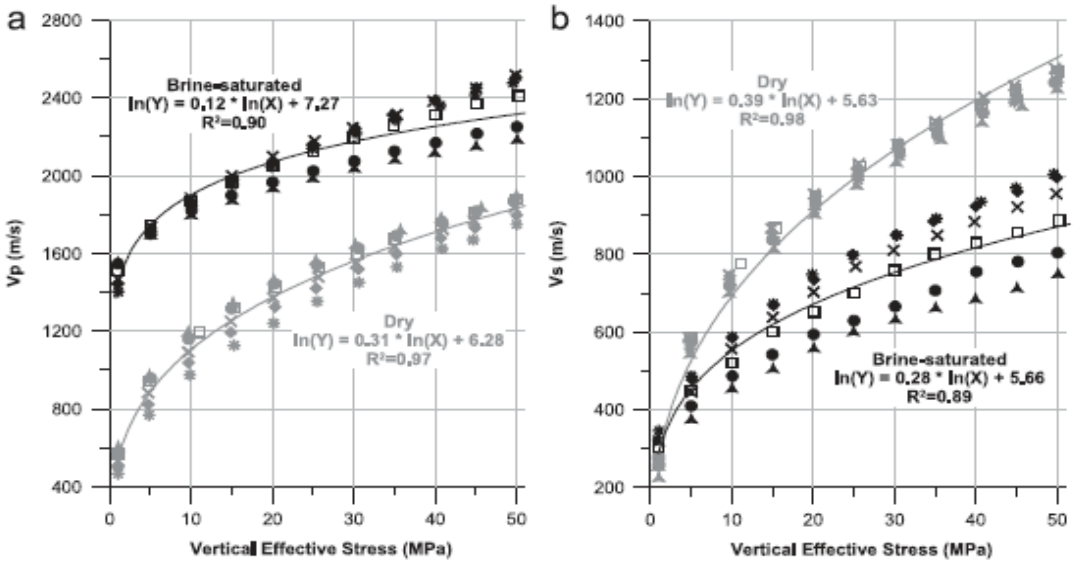

Fig. 3.6 Cross plots of P-wave velocity (a) and S-wave velocity versus the vertical effective stress for dry (in gray) and brine-saturated (in black) clay mixtures. After Mondol et al. (2007). Solid lines show least square fits to the data.

At greater depth and temperatures, chemical compaction takes over. Due to a thermodynamic drive towards more stable mineral assemblages, clay minerals like smectite are replaced by mixed-layer illite at temperatures of about 60°C to 100°C (Thyberg et al., 2009) (Eq.3.3). With increasing temperatures (depth) to about 130 °C, illite is also precipitated from kaolinite in the local presence of potassium feldspars (Eq. 3.4), which serve as a source for potassium (Bjørlykke and Jahren., 2010). The produced silica has to be transported out of the reaction system to ensure continuity of the forward reaction (Bjørlykke, 1998). However, recent evidence show that micro-quartz probably sourced from the released silica could also be precipitated in-situ producing a subtle inter-connected network within a mesh of authigenic clay crystals (Thyberg et al., 2009).

A simplified general presentation of these reactions can be written as follows:

$$Smectite + K^{+} \rightarrow illite + SiO_2 + 2H_2O \qquad \text{(Eq. 3.3)}$$

(Boles. and Franks., 1979)

$$KAlSi_3O_8 + Al_2Si_2O_5(OH)_4 \rightarrow KAl_3Si_3O_{10}(OH)_2 + SiO_2 + 2H_2O$$

K-feldspar *Kaolinite* *Illite* *Quartz* (Eq. 3.4)

(Bjørlykke, 1995)

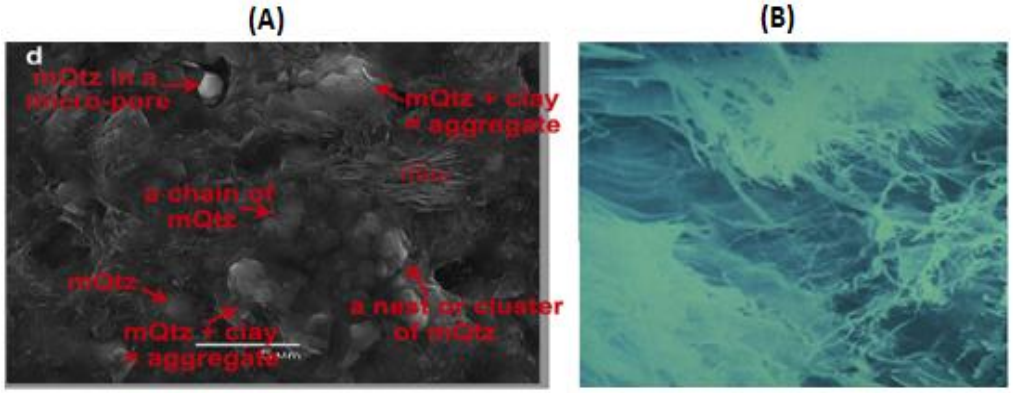

Fig. 3.7. Formation of (A) authigenic micro quartz (mQtz) cement in mudstones from Northern North Sea. Source: (Thyberg et al., 2009). (B) pore filling illite formed either by alteration (dissolution and precipitation) of smectite and/ or from kaolinite and K-feldspars (Bjørlykke, 1995).

Break-down of the feldspar grains (Eq. 3.3 and Eq. 3.4) may lead to further compaction of the grain frame work. The grain frame work is also stiffened due to the precipitation of silica released during the above reaction. The released crystalline water will reduce the salinity of pore water (Abercrombie et al., 1994), leading to a decrease in the electrolytic conductivity and a slight increase in resistivity. However the resistivity generally decreases from the release of crystal bound water.

The transformation from mudstones to shales involves not only an increase in stiffness, acoustic velocity but also marked increase in anisotropy due the preferred orientation of clay minerals. Several authors, (Ho et al., 1999, Bjørlykke, 1998, Fawad et al., 2010) have proposed a link between smectite illitization and the development of preferred clay mineral orientation in mudstones. Based on experimental observations of naturally compacted samples and synthetic mixtures (Fawad et al., 2010, Mondol et al., 2007), P- and S-wave velocities gradually increase with increasing clay content.

High velocities could also be observed at shallow depths due to early cementation from biogenic carbonates and silica.

3.2.4 Compaction of Sandstones

It is necessary to understand the basic components of sandstones before carrying out compaction analysis since both mechanical and chemical compaction processes are to a large extent lithologically dependent.

Sandstones are basically composed of (a) detrital silicate framework grains essentially consisting of quartz grains, with relatively higher mechanical and chemical stability, feldspars (ranging from alkali to plagioclase feldspars), lithic framework grains or other clasts, accessory minerals (such as olivine, pyroxenes), and heavy minerals. (b) a matrix which is very fine material found between the framework grains (c) a cement, binding the framework grains and (d) pores space. Texturally 'clean' sandstones (arenites) have very little quantities (<15%) or no matrix, whereas texturally 'dirty' sandstones (wackes) have >15% matrix (Dott, 1964).

The maximum threshold of mechanical stability of the constituent grains is of major importance during mechanical compaction. Well sorted quartz rich sandstones have a higher compressibility than the corresponding well sorted but fine grain quartz rich sand (Chuhan et al., 2002, Fawad et al., 2010) (Fig. 3.8). However, coarse grain sand will readily fracture than fine grain sand at a given stress level due to high stress at the smaller area of grain contacts. The presence of clay coatings act as a 'lubricant' and cause the sand grains to slide against each other and less likely to fracture and thereby reduce the compressibility than in pure quartz rich sand (Chuhan et al., 2002).

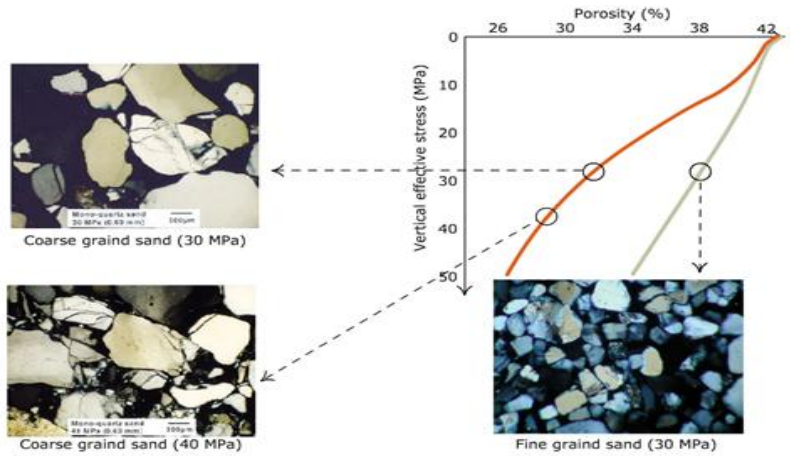

Fig. 3.8. Experimental compaction of fine-grained and coarse-grained sand showing that well sorted fine grained is less compressible than coarse grained sands. (Chuhan et al., 2003).

Chemical compaction results in porosity loss by dissolution and precipitation of minerals (Houseknecht, 1987) and is controlled mainly by temperature hence effective stress plays a very minor role.

The most commonly precipitated cement in sandstone is quartz cement starting between a temperature range of 60°C - 100°C and 2 – 2.5 Km (Mondol et al., 2007, Thyberg et al., 2009). Precipitation of quartz cement (compaction) is a continuous process even during basin inversion and uplift as long as the temperature is above 80°C and there is available porosity (Bjørlykke and Jahren., 2010). The principal precursor of the cement is from the pressure solution of quartz clasts at contacts with illitic clays and micas.

The quantity of precipitated quartz cement is also a function of the grain surface available (IGV from mechanical compaction) coupled with the time - temperature integral with an increased rate by a factor of 1.7 for every 10°C temperature increase (Walderhaug, 1994). This is a surface - controlled reaction by virtue of the fact that the rate limiting process seems to be the rate of nucleation and precipitation in the pore space (Bjørkum et al., 1998).

Grain coatings on clastic quartz grains such as iron oxides, micro-crystalline quartz, detrital clays, chlorite, illite and bitumen (Fig. 3.9A) prevent or slow down the rate of quartz cementation (Ehrenberg and Boassen, 1993, Storvoll et al., 2002, Chuhan et al., 2002)

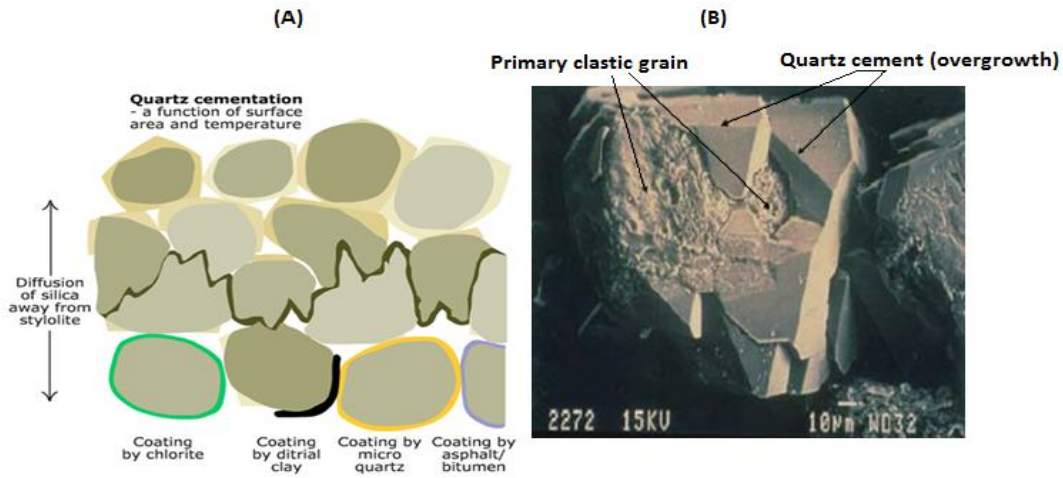

Fig. 3.9. (A) Schematic illustration of Pressure solution of quartz clasts at grain contacts with clays (stylolite). Grain coatings prevent or slow down quartz cementation and preserve porosity at greater depths. (b) Quartz cement with smooth crystal surfaces as overgrowth on clastic grains. Adapted from Bjørlykke and Jahren., (2010).

Carbonate cement in sandstone is also common mostly due to dissolution and precipitation of biogenic carbonates or early aragonite cement at relatively lower temperatures such as in carbonate sands. However the transformation of amorphous silica (Opal A to Opal CT)

occurring at relatively lower temperatures (depth) could also result in porosity loss and high P-wave velocities.

Mechanical compaction in sandstone by grain rearrangement is halted by the precipitation of modest quantities of quartz cement (Bernabé et al., 1992, Vernik and Nur, 1992, Dvorkin and Nur, 1996). This greatly increases the stiffness and reduces its compressibility resulting in an abrupt increase in velocity. Under such conditions, the sandstone may compact along a stress-strain profile for overconsolidated rocks. This behaviour, referred to as 'pseudo-overconsolidation' could be misinterpreted as overconsolidation due to previously higher effective stress (Bjørlykke et al., 2004). There for a priori knowledge of the sediment burial history is essential during compaction analysis.

3.3 Methodology

3.3.1 Correlative Analysis of Petrophysical logs

Well logs contain enormous amount of information which can be utilised to identify different facies, lithology, pore fluids and overpressured intervals. Entire log data is used for compaction analysis rather than averaging as this allows for much more precise interpretation of how rock properties actually vary with depth. A relatively large scale approach is employed whereby investigations are carried out both at Group and Formation levels. The general velocity depth trends for each well will be analysed with other petrophysical logs with respect to the dominating compaction mechanisms and possible controlling factors, after which it is then compared both with each other and with published and unpublished (experimental) compaction curves in clastic rocks. At this level, all available logs are studied in concert.

3.3.2 Crossplots

Several combinations of cross plots are generated for the different wells in order to further ascertain the lateral and vertical distribution of rock properties and reservoir intervals with good quality sandstones, compaction gradients, transition from one compaction domain to the other. The effects of incipient chemical compaction (quartz cement) on dynamic rock properties are also deciphered by these cross plots. These include Vp/ Vs/ Gamma ray/ Porosity/ versus depth, Shear modulus versus porosity and finally a cross plot of Vs versus Vp to adequately define effective reservoir horizons.

3.3.3 Correction for Exhumation and Comparative Analysis

The Barents Sea area experienced Tertiary uplift and erosion known as exhumation is defined as 'the displacement of rocks with respect to a surface'(England. and Molnar., 1990). A correction for exhumation to represent maximum sediment burial depth is necessary to enable more elaborate compaction and comparative analysis with published compaction data.

An experimental compaction curve for a Kaolinite – Silt (50:50 %) from Mondol., (2011) (personal communication) is employed to estimate the magnitude of exhumation. This curve is deemed appropriate over the other available published compaction curves as it gives a good control on the initial mineralogical composition of the compacting sediment. Furthermore, a kaolinite – silt mixture is more representative of naturally occurring shales.

A three step simplistic approach it employed to estimated exhumation:

1.) The transition zone from mechanical to chemical compaction at present day burial depth is deciphered using rock physics crossplots.
2.) Volumetric shale fraction (V-shale) corresponding to mechanical compaction at present day burial depth is calculated across the entire area and cross-plotted as function of depth.
3.) The naturally compacted samples are then projected onto experimentally compacted kaolinite – silt (50:50) mixture. The difference along the depth (m) axis gives an estimate of the magnitude of exhumation the natural samples have undergone.

After correcting for exhumation, well data is analyzed with respect to different compaction mechanisms and controlling factors. The transition zone between mechanical and chemical compaction is then accurately defined at the actual depth (pre – exhumation depth) at which it occurred.

The natural samples are then compared both with experimental compaction curves, natural compaction curves representative of the Hammerfest basin, marine shales and a compaction curve of the Etive sandstones in the North Sea.

3.4. Results

3.4.1 Compaction Trends in the Study Area

Analysis based on petrophysical well logs reveals the two distinct compaction regimes across the entire study area. Mechanical compaction (MC) and chemical compaction (CC). A zone of overpressures (OP) is also observed just below the transition form one compaction domain to the other. Anomalous velocities are indicated by the red circle. Relationships between P-wave velocity (Vp), gamma ray, bulk density, porosity as a function of depth for all the wells are presented in Figure. 3.10.

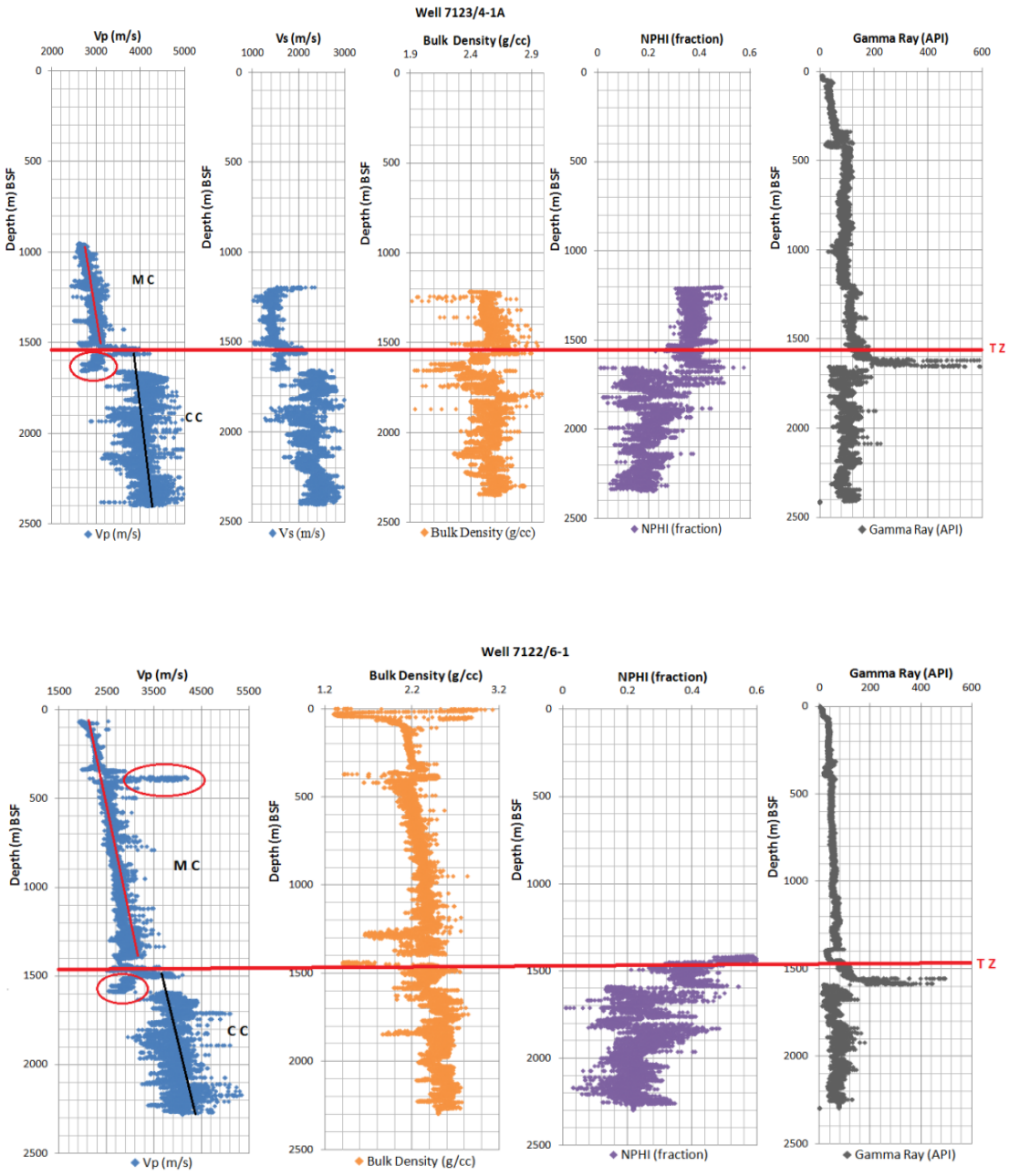

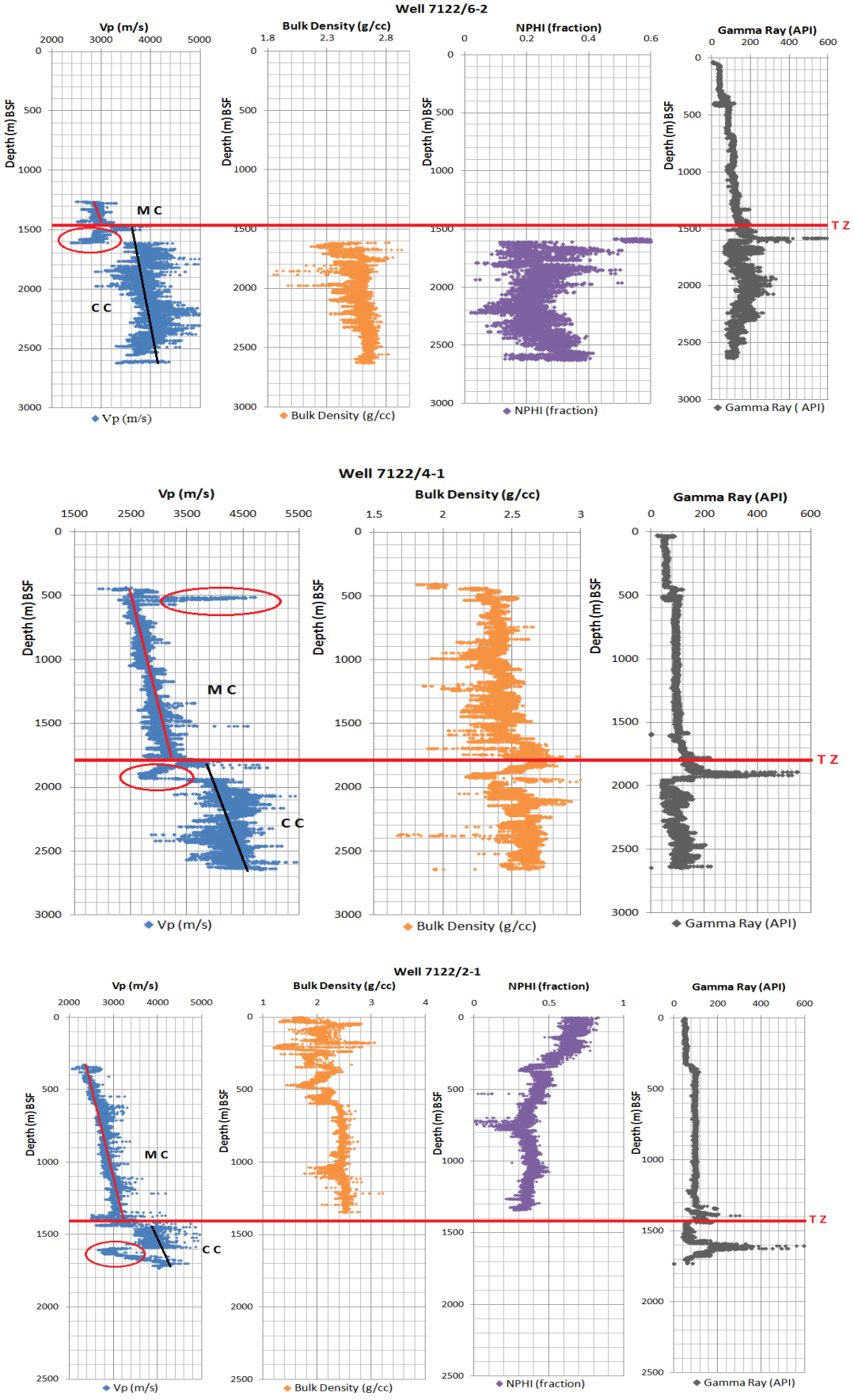

Fig. 3.10. Cross plots of Vp/ Bulk density / Neutron porosity/Gamma ray versus depth for five wells cross the entire study area. Generally two distinct compaction trends are identified on all cross plots.

Well 7123/4-1 is selected as the reference well for a relatively detail compaction analysis because it contains both compressional and shear wave velocity information. Furthermore, according to NPD (Norwegian Petroleum Directorate) it is classified as a dry well with shows of residual hydrocarbons in different zones. This minimises the effects of pore fluids on the acoustic properties. Analysis from this well is cross-referenced with the other well data for correlation. Two compaction trends can be identified (Fig. 3.11) where the interval A1 corresponds to mechanical compaction (MC) and A2 corresponds to chemical compaction (CC).

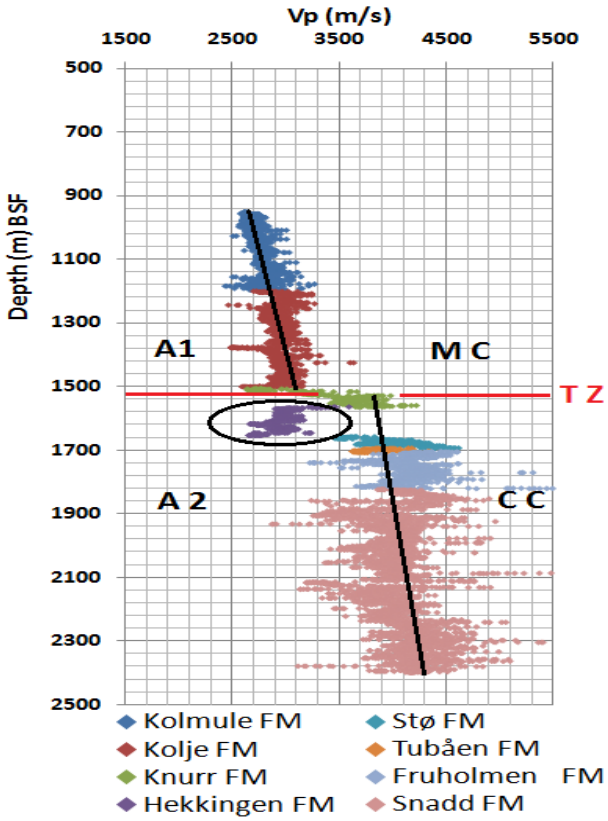

Fig. 3.11. Vp (m/s) - Depth (m) plot for well 7123/4-1A at present burial depth below sea floor (BSF). The various Formations have been separated in to different colours for better illustration. The general trend line (in black) is not for a particular lithology but for the entire well data. The highlighted area (black circle) represents anomalous velocity. The transition zone (TZ) separates mechanical compaction (MC) from chemical compaction (CC)

- **Interval A1**

It consists of velocities from the Adventdalen Group. A similar trend is observed in wells 7122/6-1, 7122/6-2 and 7122/2-1 (Fig. 3.10). The general trend line shows a linearly increasing velocity with depth irrespective of minor variations within some Formations.

In well 7122/6-1, this interval starts with the Nordland Group followed by the Sotbakken Group showing low velocities. In marked contrast to the overlying Torsk Formation, high a velocity is observed in the Kviting Formation (Fig. 3.10) in wells 7122/6-1 and 7122/4-1 at approximately 400m and 500m BSF respectively. This is results both from the early carbonate cement at relatively low temperatures and from limestone interval. The bulk density also increases accordingly. A similar trend is observed the upper parts of the Kolmule Formation consisting of limestones and dolomite stringers.

The rest of the A1 interval (Fig. 3.11) shows a generally increasing velocity with depth (with a small data spread). A corresponding increase in the S-wave log is observed for well 7123/4-1A (Fig.3.10), both resulting from a maximum mechanical compaction from a 1530m overburden corresponding to approximately 15 MPa (Mega Pascal) effective stress from the overburden.

The highlighted area (black circle) on Figure 3.11 shows anomalous velocities from the organic rich Hekkingen Formation. A density inversion is also observed.

- **Interval A2**

This interval starts at about 1530 m (BSF). This comprises the Knurr, Stø, Tubåen, Fruholmen and Snadd Formations. Stø and Tubåen Formations are mineralogically and texturally mature sandstones (Dallan et al., 1988). Though the general trend line depicts a general increase in velocity with depth as in the A1interval, the velocity is remarkably higher.

The rest of the interval shows an increase in velocity with a very broad data spread. Minor variations in compaction trend of the interval A2 coupled with the higher data spread across the study area could be attributed to lateral facies variations and in pore fluids (gas and oil shows without pressure communication) (NPD Factpages. 2011) in the Triassic Formations.

3.4.2 Transition Zone (T Z) from Mechanical to Chemical Compaction

This zone varies greatly across the study area partly due to structural evolution and geometry of the basin given that the wells span from the axis of the Hammerfest basin, close to Loppa High and finally, on a rotated fault block. Adequate identification of this zone is of particular interest as it greatly influences rock properties.

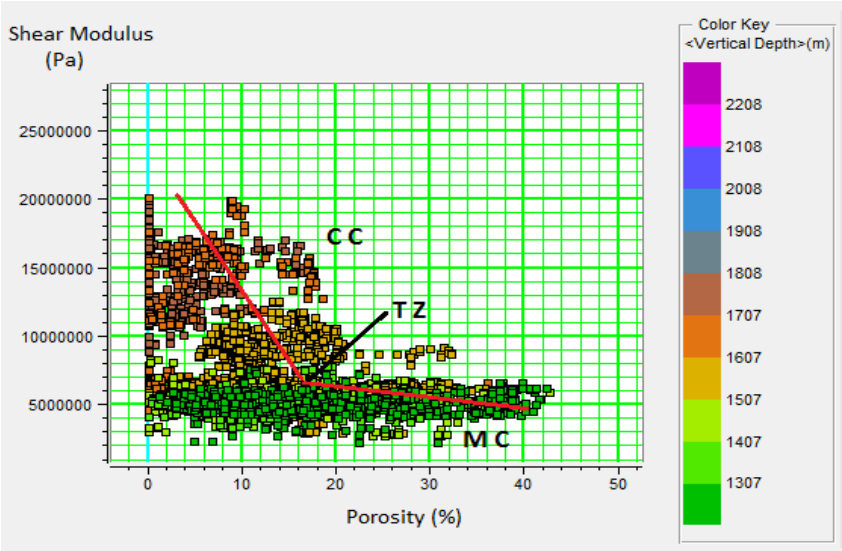

Fig. 3.12. Shear modulus versus porosity (NPHI) for shales only in well 7123/4-1A. Colour coded with depth to illustrate the transition zone (TZ) from mechanical compaction (MC) to chemical compaction (CC) occurring at the 'knee point'.

Figure 3.12 depicts a robust rock physics relationship of shear modulus and porosity for shales only, in well 7123/4-1A. Shear modulus (μ), defined as the resistance to shear (strain) of a rock when a seismic wave is propagated through (stress). It is the product of the density and S- wave velocity squared (ρVs^2). The shear modulus is not sensitive to pore fluids, hence a good frame indicator. Total volumetric shale (V_{shale}) is calculated from the gamma ray log. Pure shales (Vshale) are defined using values in the range of 0.8 – 1.0 using the formula:

$$V_{sh} = \frac{GR_{log} - GR_{min}}{GR_{max} - GR_{min}} \qquad \text{(Eq. 3.5)}$$

The geothermal gradient is estimated as 27°C/ km from the bottom hole temperatures (BHT = 94°C) while considering a surface temperature of about 4°C depending on the water masses (Loeng, 1991).

At present burial depth, the transition zone (TZ) from mechanical to chemical compaction domain in well 7123/4-1A can directly be identified on the cross plots as occurring at a depth of 1530m BSF (''knee point''), corresponding to temperatures of approximately 41.3°C. However, using geothermal gradients of 30°C (Laberg et al., 1998) rather gives a transition temperature of 45.9°C. Considering the effects of uplift imply that this transition actually occurred at greater depths. As such, after correcting for exhumation and using

temperature estimated from the BHT, the transition zone is at 3130m at a temperature of 84.5°C. Due to uncertainties related to borehole condition during recording of the BHT, a geothermal gradient of 30°C (Laberg et al., 1998) is used and this sets the transition zone to occur at a temperature of 93.9°C.The linear trends are indicated to emphasize the TZ from MC to CC for better illustration.

3.4.3 Rock Property Variations

Velocity data for sands and shales are equally plotted as a function of depth in order to investigate the how compaction mechanism varies for these different lithofacies. The results are presented in Figure 3.13

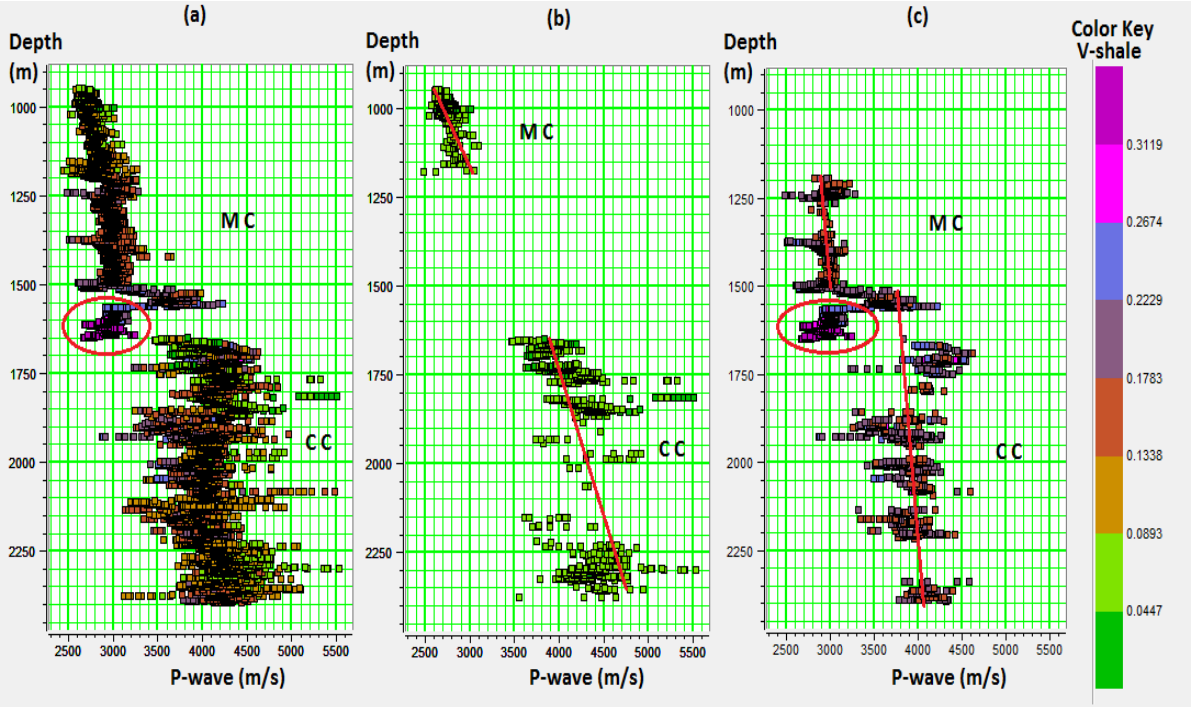

Fig. 3.13 Crossplots of P-wave versus Depth for (a) entire well data, (b) clean sands and (c) shales only, for well 7123/4-1A colour coded with V-shale. The highlighted area in red circle indicates a zone of overpressure in the Hekkingen Formation. Sands compact along a higher gradient than shales. A similar pattern is observed for wells 7122/4-1, 7122/6-1 and 7122/6-2.

Clean Sands and shales will generally show up as low and high gamma values respectively (Fig. 3.13). However, carbonates will also tend to have low gamma values too, but at a relatively shallow depth, they have anomalously high velocity. Sand and shale show compaction along different gradients. This difference in compaction gradients is clearly seen, in this case study, within the chemical compaction domain whereby under similar

temperature conditions and thermodynamic drive for more stable mineral assemblages, the rate of cementation will be different given that the inter-granular volume (IGV) available for quartz cement is different for sand and shale resulting from differential mechanical compaction.

A cross plot of Vs versus Vp is generated in order to accurately define good reservoir intervals across the study area that could be used for further rock property analysis. Vs is a good frame indicator as it is transmitted through the grain framework. When combined with Vp is serves as a good lithology indicator. Clean sands of the Stø Formation have higher Vs than shales at a given Vp level. For example, at Vp = 3750 m/s (Fig. 3.14).

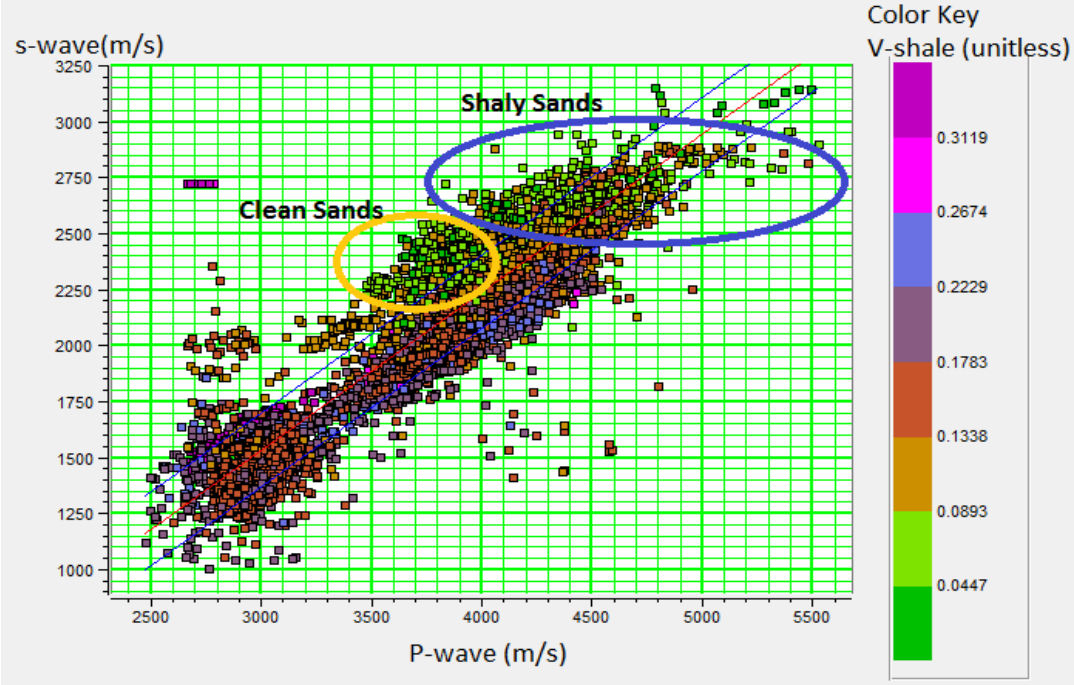

Fig. 3.14 Crossplot of Shear-wave velocity versus P-wave velocity for well 7123/4-1A color coded with V-shale. S-wave velocities show a lithology dependent gradation, hence good lithology indicators.

Vs used in Figure. 3.14 and Figure 3.15 is from direct measurements in Well 7123/4-1A, though there exist several methods (Castagna et al., 1985, krief et al., 1990) for determining Vs in areas where there are no direct measurements. The Triassic Snadd Formation is almost entirely made up of shaly sandstones apart from the clean sands at depths of approximately 2230m BSF (Fig. 3.15), corresponding to the tight Carnian sandstones.

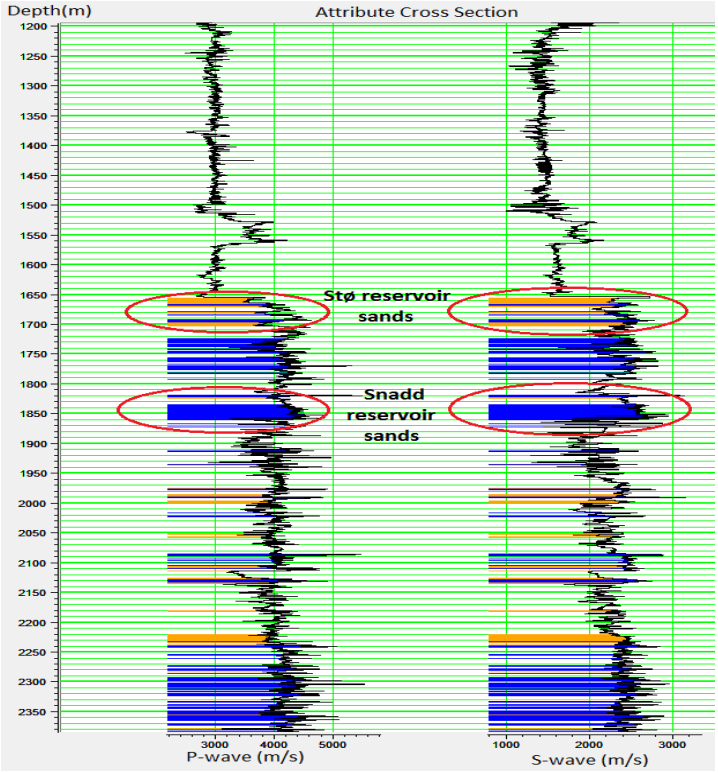

Fig. 3.15 Attribute cross section from the Vs versus Vp cross plot versus depth (m) BSF for well 7123/4-1A, showing the vertical distribution of clean sands (orange) as in the Stø reservoir and shaly sands (blue) as in the Snadd reservoir. The Triassic sequence is dominated by shaly sands.

A comparison of velocity logs and bulk density log for well 7123/4-1 (Fig. 3.16) reveals that at the vicinity of the abrupt velocity increase, the density log does not show a corresponding abrupt increase indicating that a different factor other than density is responsible for the sudden change in velocity.

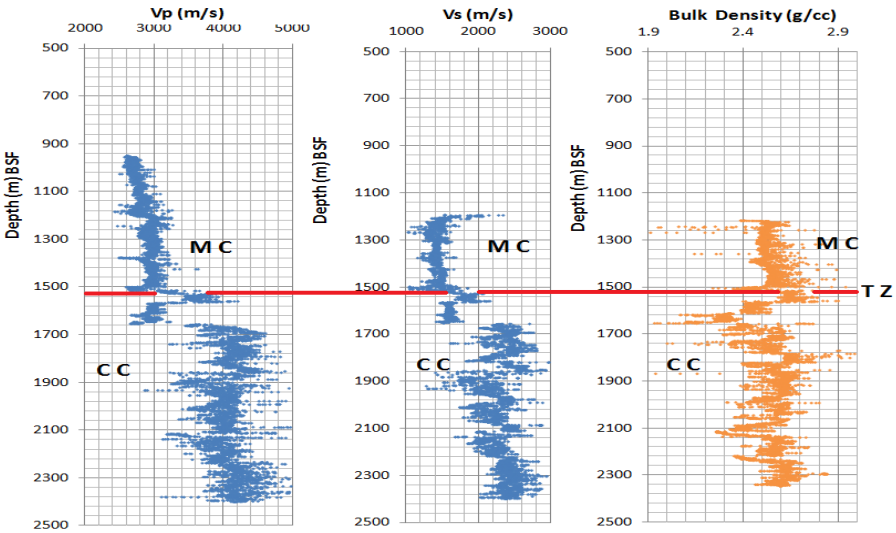

Fig. 3.16 Effect of incipient quartz cement on bulk density, well 7123/4-1 at present burial depth below sea floor (BSF). Vp/ Vs / Bulk Density versus Depth (m) Below sea floor (BSF). The transition zone (TZ) between mechanical compaction (MC) and chemical compaction is marked by the red line.

3.4.4 Correction for Exhumation and Comparative Analysis

Exhumation estimate is done at each well location and an estimated magnitude is found in Table 3.1. Shales, corresponding to mechanical compaction domain are used. The entire sonic log is used during rather than averaging, this allows for a more precise analysis of the velocity variation with depth. When applying this simplistic method to correct for exhumation, the choice of experimental data to use is essential as this could lead to misleading estimates. This is illustrated in Figure 3.17, using mechanically compacted shales only for well 7122/2-1 and experimental compaction curves for Kaolinite – Silt (50:50), Kaolinite – Smectite (80:20) and Kaolinite (100 %) results in exhumation estimates of 1200m, 2500m and 2700m respectively. The mineralogical composition of the experimental data should reflect that of the natural samples, since velocities are also mineralogically dependent.

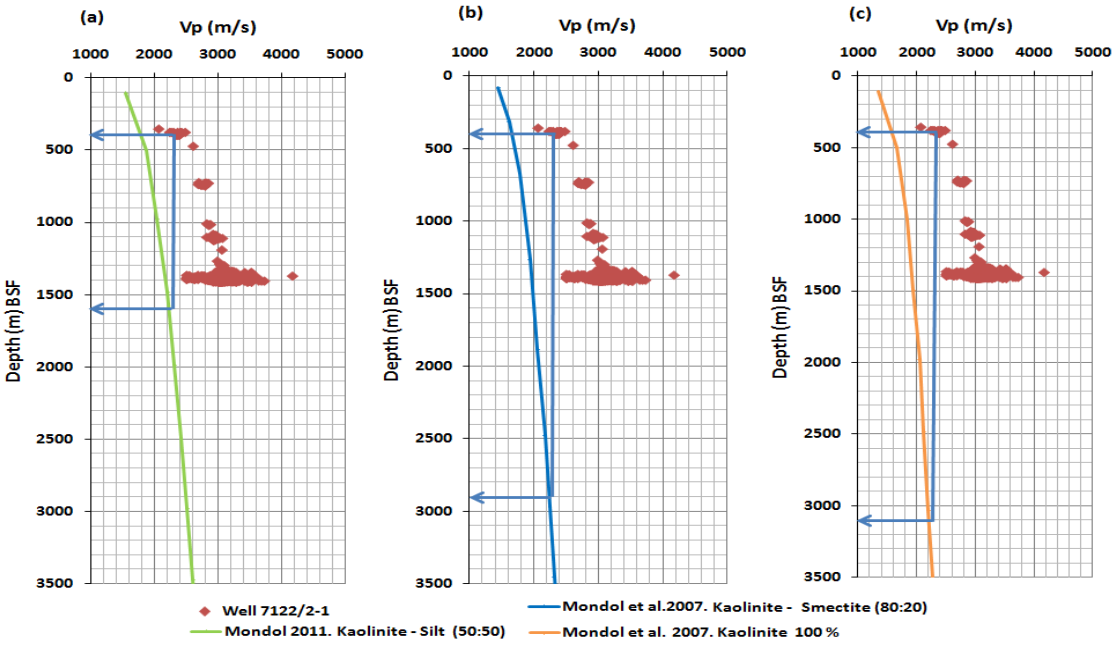

Fig. 3.17 Exhumation estimates for well 7122/2-1 using experimental compaction curves for Clay - Silt and Clay - Clay mixtures. The shales are for mechanical compaction domain only.

Shale being a mixture of clay, silt and electrostatically bound water, the kaolinite – silt (50:50) curve is most appropriate assuming that kaolinite is the most abundant clay mineral in the area though smectite precursors are also present especially in the Torsk Formation. Based on this experimental curve, estimates from different wells are presented below. The lowest estimate from well 7122/2-1 is probably due to its position close to Loppa High. Estimates from individual wells presented below indicate differential magnitude in uplift.

Table. 3.1. Exhumation estimates for four wells based on experimental compaction curve of a Kaolinite - Silt mixture (50:50). Mondol., (2011) (personal communication.

Wells	Exhumation estimate (m)
7123/4-1A	1600
7122/6-1	1500
7122/6-2	1450
7122/2-1	1200
7122/4-1	1600

Comparative Analysis;

Experimental Compaction versus Natural Compaction

Calculated V-shale is for each well corresponding to mechanical compaction domain is compared with experimentally compacted clay – clay and clay – silt mixtures both before and after correcting for exhumation (Fig.3.18). The entire well data is also used for comparison with published compaction curves (Fig. 3.20).

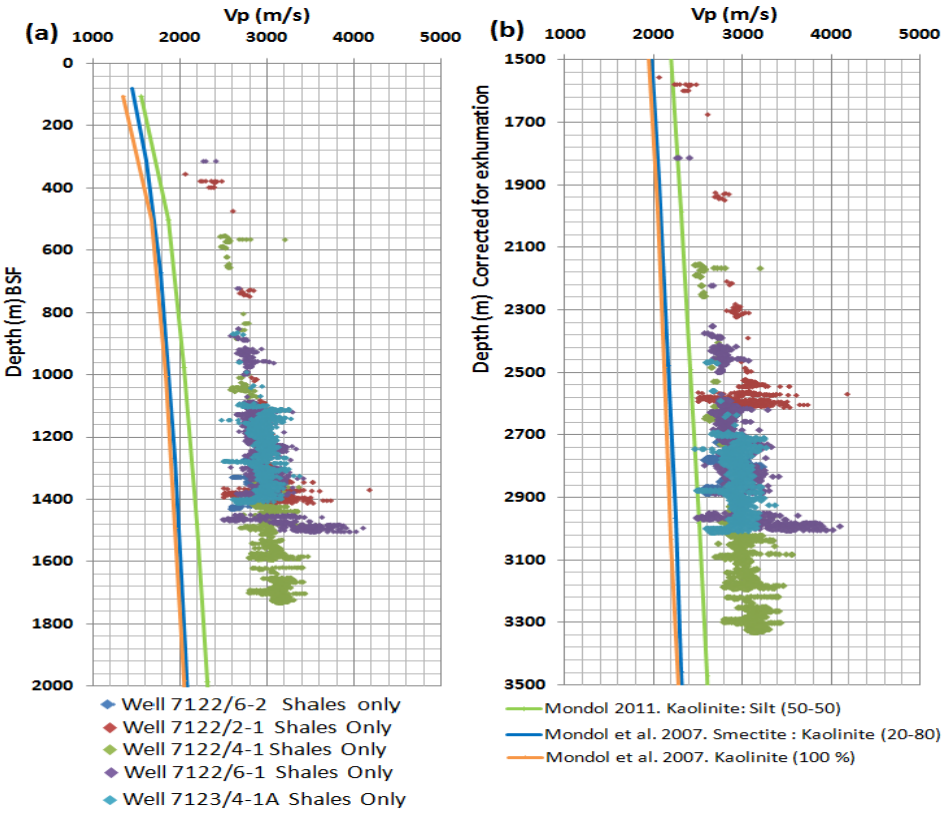

Fig. 3.18 Correction for exhumation using shales only, for five wells corresponding to mechanical compaction. (a) Vp(m/s) – Depth(m)BSF at present burial depth compared with different experimental clay mixtures. (b) Vp(m/s) – Depth (m) after correcting for exhumation and compared with experimental samples.

When using well log velocity data that had not been corrected for exhumation, (Fig 3.18a), the velocity is remarkably higher than that for experimental compaction curves. After correcting for exhumation, it becomes apparent that the naturally compacted shale samples corresponding to mechanical compaction show a generally similar compaction trend with experimental curves, Mondol et. al. 2007, Mondol., (2011) (personal communication), with a progressive increase in Vp with depth (Fi.3.18b).

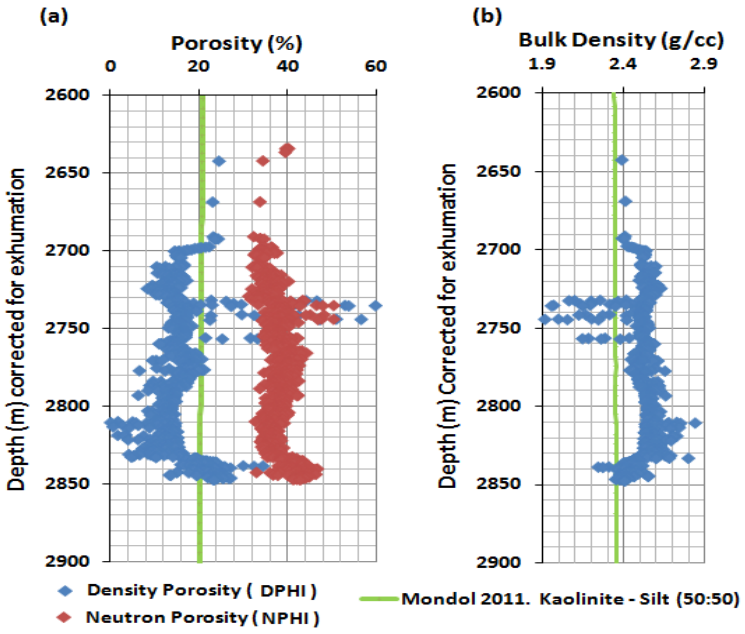

Fig. 3.19 Shales only, corresponding to mechanical compaction after correcting for exhumation. (a) Neutron porosity (NPHI) / Density porosity (DPHI) versus depth compared with experimental porosity-depth curve for a Kaolinite – silt (50:50) mixture. (b) crossplot for bulk density – Depth for shales compared with experimental density curve for a kaolinite – silt (50:50) mixture.

Neutron log is basically a measure of Formation water content which could be bound water, crystallization water or free pore water and gives a measure of the porosity. In shales, water occurs either within the molecular structure or between the phyllosilicate layers. This results in high porosities in shales (Fig. 3.19) and could not be appropriate for comparison with experimental data. Neutron porosity gives a rather good measure of porosity for brine-saturated sandstones. Log derived neutron porosities is expressed mathematically as:

$$\log_{10} \varphi = aN + B \qquad \text{(Eq. 3.6)}$$

Where φ is the true porosity, a, B are constants and N is the reading from the neutron tool.

In contrast to the neutron porosity, using the bulk density of shales as 2.57g/cc and fluid density of 1.09 g/cc, porosity (DPHI) is then calculated from log derived bulk density. However, assuming a constant grain density after filtering out shales only, corresponding to mechanical compaction, a close relationship seems to exist between the bulk density and porosity. This gives a lower porosity when compared with neutron porosity (NPHI)
This relationship is expressed as:

$$\rho b = (\varphi)(\rho f) + \rho m \qquad \text{(Eq. 3.7)}$$

Solving for porosity (φ) gives:

$$\varphi = \frac{\rho m - \rho b}{\rho m - \rho f} \qquad \text{(Eq. 3.8)}$$

Where; ρm is the matrix density, ρb is the bulk density and ρf is the fluid density.

Comparing DPHI/ NPHI with experimentally derived porosity from a kaolinite – silt (50:50) mixture, a fair to slightly lower porosities with DPHI and higher porosity with NPHI becomes evident (Fig.3.19a). Density from the natural samples is also seen to be slightly higher than the experimental curve (Fig. 3.19b) reflecting a well advanced degree of compaction. This could also suggest that these Formation generally have a relatively ≥ 50 % kaolinite content though other factors could also result in higher density other than the clay content. Clay mechanical compaction steadily increases with a corresponding increase in the Kaolinite content (Mondol et al., 2007). As such, a possible contributing factor to the resultant higher velocities from the well data when compared with Mondol., (2011) (personal communication) compaction curve (Fig. 3.18b).

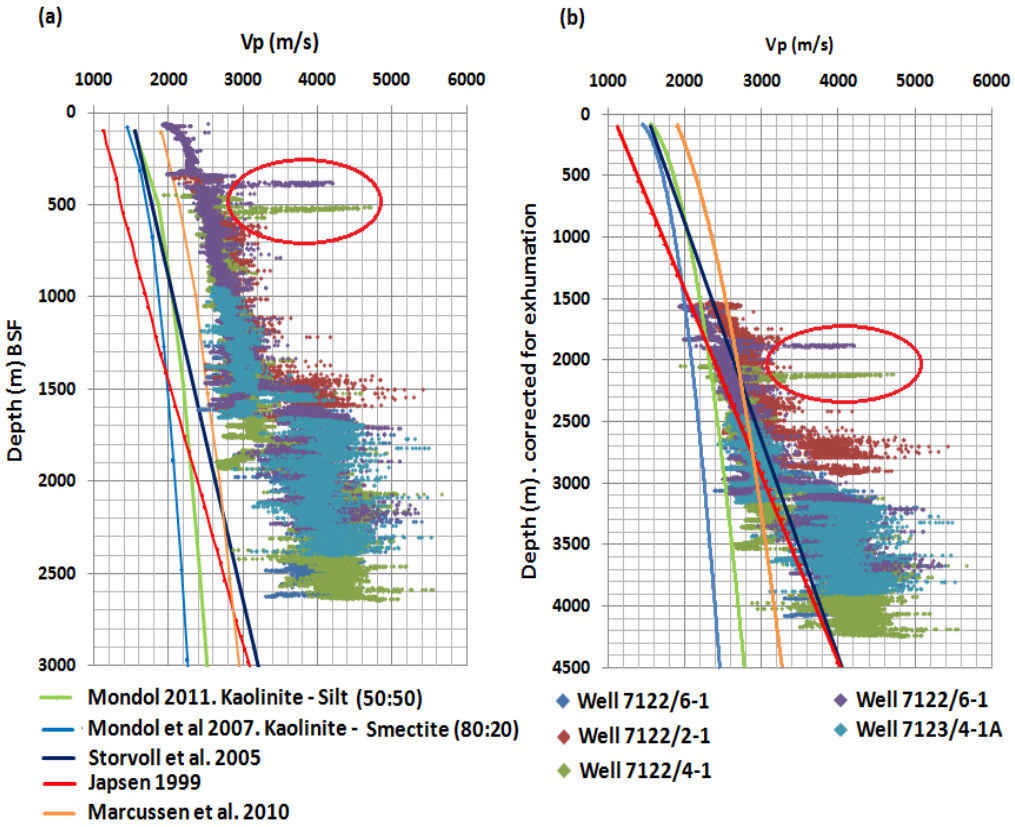

Fig. 3.20 Composite cross plot of Vp – Depth for 5 wells using entire well data. Trend lines from three different published and experimental data have been included for comparison. (a) Present depth below sea floor (BSF). (B) Corrected for Tertiary exhumation. The highlighted area (red circle) represents anomalous velocity from shallow carbonates.

After correcting for exhumation, using the entire data (Fig. 3.20b), velocities from well logs fits excellently with published compaction curve from Mondol. (2011) (personal communication) and Storvoll et al. (2005), but are slightly higher than the Japsen. (1999) curve (with an exception in well 7122/2-1) and the kaolinite – smectite curve, within the fine grained sediments of the Nordland and Sotbakken Groups. Anomalous velocities, highlighted by red circle, at such shallow depths are from limestones of the Kviting Formation showing very low gamma ray values. However, from about 2000m well log derived velocity deviates from Mondol. (2011) (personal communication) curve with higher velocities throughout the mechanical compaction regime but shows a rather good match with Japsen. (1999) and Storvoll et al. (2005) compaction curves. Velocities from the Hekkingen Formation at approximately 3000m are quite lower than data from Japsen (1999), Marcussen et al. (2010) and Storvoll et al. (2005) compaction curves irrespective of such a burial.

From about 3100m, there is a general deviation of the natural samples from all the published and unpublished compaction curves (Fig. 3.20b) stipulating an abrupt change in compaction regime.

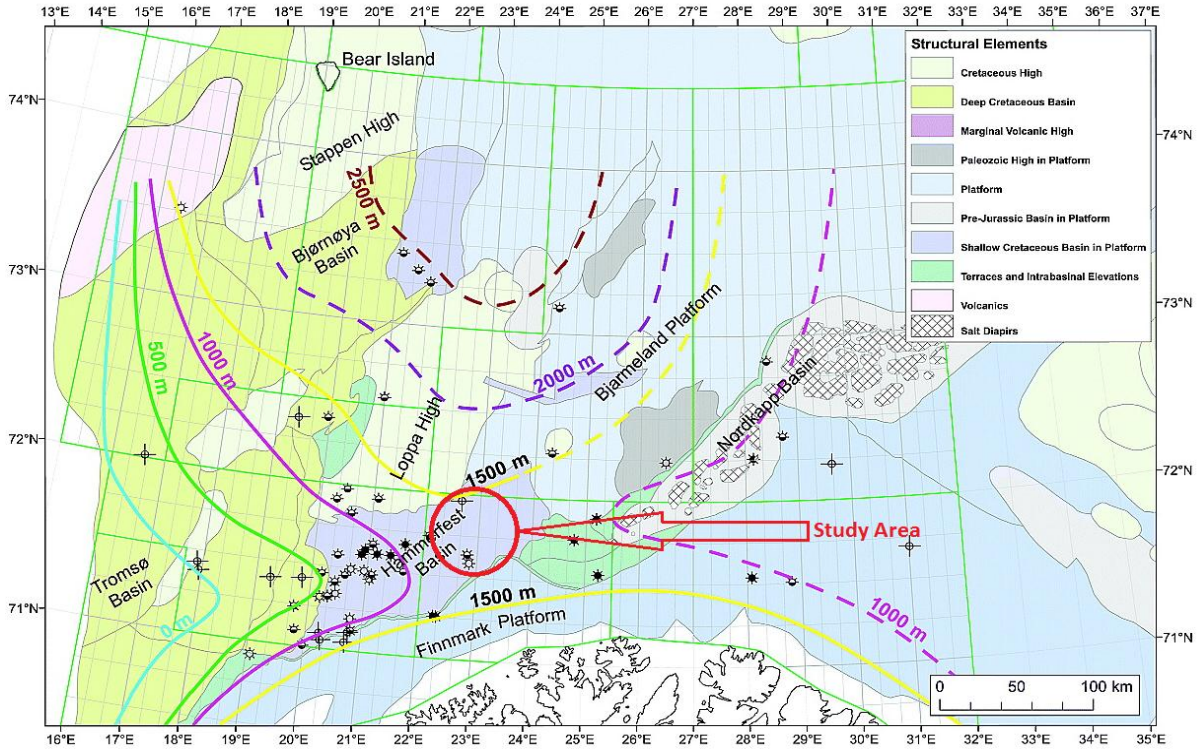

Fig. 3.21 Modified tentative uplift map illustrating the total amount of uplift based on vitrinite data. The area under consideration in this study is indicated by the red circle. Modified from: Ohm et al. (2008).

Figure 3.21 depicts a tentative uplift estimate map (Ohm et al., 2008) based entirely on vitrinite reflectance (R_o) data from 67 exploration wells drilled in the Norwegian Barents Sea with an uncertainty in the order of $\pm$500m. The method employed in this study gives a similar uplift range without quantifying the associated uncertainties (Table. 3.1).

3.5 Discussion of Results

3.5.1 Compaction as a Function of Rock Properties

When analysing data from individual wells, a highly similar pattern in the velocity – depth gradient is observed for all four wells, particularly in the mechanical compaction domain (Fig. 3.10). This probably indicates no major lateral lithologic variations in the inter-well areas. However, the Kviting Formation with a thickness of about 90 m in well 7122/4-1 thins out and completely disappears towards the eastern wells and passes into the Kveite Formation of the same Group which thins out in the opposite direction and is absent in well 7122/4-1. The Fuglen Formation, 29 m, also thins out in towards the east. The 44m thick Nordmela Formation in well 7122/4-1 also gradually thins out towards the east with 11 m in

well 7122/4-1S. Lithologically, the Torsk Formation is composed claystones with basal tuffaceous horizons which could serve as excellent smectite precursors explaining the lower velocities at the start of the A1 interval in Figure 3.11. The thicknesses of the different Formations vary but laterally extensive throughout the study area with the Fuglen Formation as an exception.

At present day burial depths below 1530m BSF in well 7123/4-1A (Fig. 3.11), mechanical compaction is the main process responsible for porosity reduction, increase in density and consequently the velocity constrained by varying mineralogy and texture resulting from differences in depositional environments though there seem to be very little variations in gamma ray logs throughout this depth interval. This compaction regime is dominated by mudstones and shales across the study area (Fig.3.13). Compaction in shales and mudstones is highly controlled by mineralogy and micro-fabric (Fawad et al. 2010). That is if the compacting sediment is grain supported or matrix supported. Increasing vertical effective stress in a generally matrix supported system such as in the Cretaceous, Pliocene and Pleistocene sediments, results in a higher orientation of clay minerals resulting in anisotropy with higher velocities perpendicular to the direction of alignment. The degree of orientation is has been shown (Oertel and Curtis, 1972, Curtis et al., 1980) not only to be a simple function of strain but also by the presence of non-platy particles like quartz. This is however a very complex process (Meade, 1964).

Analysis based on gamma ray logs show no significant lithologic variation around the transition depth from mechanical to chemical compaction implying that these mudstones are relatively homogenous. It can then be resolved that the sharp increase in velocity is not due to a sudden change in lithology but rather a chemically induced change controlled by thermodynamics. This velocity increase at present depths of 1530m BSF ($\geq 45.9^{o}$C), in the reference well 7123/4-1A, could be inferred as corresponding to the precipitated micro-quartz cement released from the transformation of the clay mineral smectite to illite through a mixed layer illite – smectite (IS) (Eq. 3.3). Water released from this transformation (Abercrombie et al., 1994, Boles. and Franks., 1979, Peltonen et al., 2009) resulted in a decrease in the resistivity log (Fig. 3.22) around the transition depth (1530m BSF present depth). The smectite – illite transformation will only occur when pore water silica concentration has been reduced to a normal saturation level relative to the temperature given the assumption that pore water at deposition is supersaturated with respect to silica (Storvoll

and Brevik., 2008). The low silica concentration is thought to be achieved through the opal A to opal CT and quartz transformation. Another important implication of this reaction is the decrease in the volume of solids when soft smectite is replaced by the illite with a more dense mineral structure (Avseth., 2010).

Uplift and erosion are generally followed by a decrease in temperatures. After correcting for exhumation and using a geothermal gradient of 30˚C/Km (Laberg et al., 1998), the transition zone then corresponds to a depth of 3130m and a temperature of about 94˚C which is quite well within the theoretical temperature range for the onset of chemical compaction of clays/ shales at 60 - 100°C (Mondol et al., 2007, Thyberg et al., 2009). This transition zone (TZ) corresponds to a porosity of approximately 18% (Fig. 3.12).

Not all chemical reactions in clays/ shales occur within this temperature range. There is also the kaolinite – illite reaction (Eq. 3.4) which also results in the precipitation of quartz but rather occurring at a much higher temperature of about 130°C (Bjørlykke et al., 2004, Storvoll and Brevik., 2008) which may further increase the rock elastic moduli and further reduce the porosity. This reaction will not commence in the absence of a potassium precursor (Peltonen et al., 2008). It is worthy to note that the quartz released from these reactions could be precipitated in-situ in shales (Thyberg et al. 2009) or could be precipitated out of the reaction system (Peltonen et al. 2009).

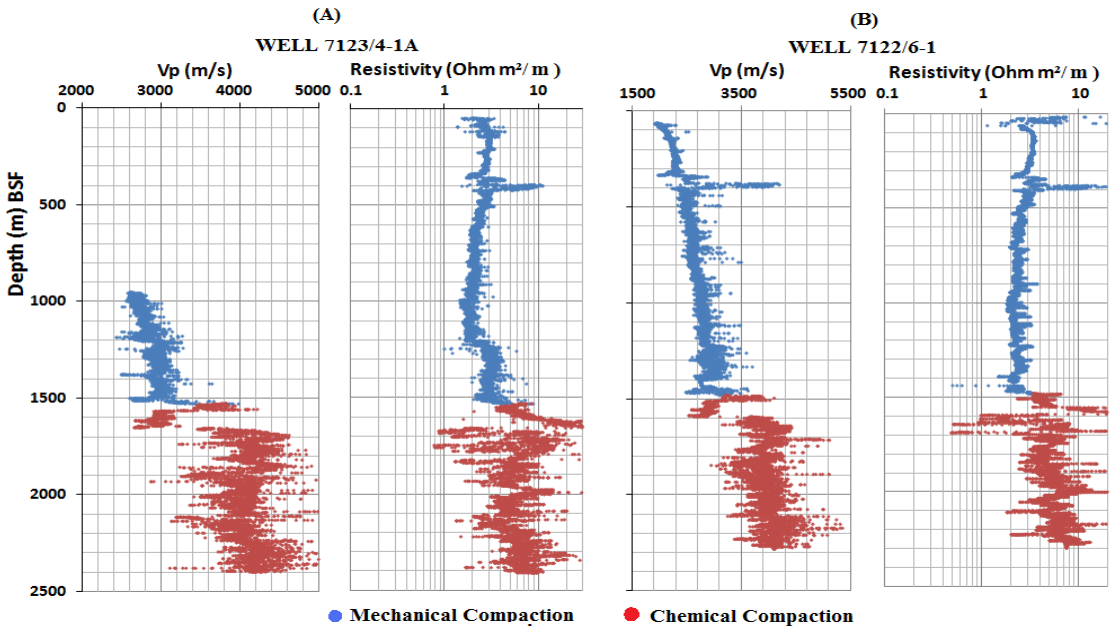

Fig. 3.22 Cross plots of Vp (m/s) and Resistivity (Ωm²/m) logs versus Depth (m) BSF for (A) well 7123/4-1A and (B) well 7122/6-2. Both wells depict a decrease in resistivity around the transition from mechanical to chemical compaction though as seen from the cross plots the depth of this zone is slightly different for both wells. Both well data are put at thesame depth level uniquely for illustration purpose.

The incipient onset of quartz cementation observed by an abrupt increase in velocity, at 1530m does not coincide with a corresponding sudden increase in the bulk density (Fig. 3.16). The quartz cement resulted in an abrupt velocity increase due to grain work stiffening but does not affect the bulk density because the rock volume is not significantly modified at the onset of quartz cementation. Higher densities (porosity reduction) probably caused by quartz cement only becomes evident at about 1800m BSF (Fig. 3.16) in well 7123/4-1A. Porosity loss by mechanical compaction is quite limited and only chemical compaction can result in 0% porosity.

Chemical compaction by quartz cement becomes dominant at present depth of ≥ 1530m in (well 7123/4-1A), and is controlled basically by the time temperature integral (Walderhaug, 1994) and will continue during basin inversion (Bjørlykke et al., 2010) (Fig.3.5). This process occurs in mudstones (Fig 3.7) as well as in sandstones (Fig 3.9) but at different temperature range. In the Stø and Tubåen sandstones, the minor clay rich intervals in contact with quartz grains could have evolved into stylolites (pressure solution) upon burial, providing silica for quartz cementation. The good permeability in the Stø and Tubåen Formation (NPD Factpage. 2011) suggests the probable presence of grain coating coupled with moderate to low amounts of detrital clays serving as stylolite precursors. The high pore pressures in the overlying Hekkingen Formation may also have resulted in a reduced amount of mechanical compaction in the underlying Stø and Tubåen Formations during burial explaining the good reservoir qualities.

Upon close observation form acoustic logs, there is a slight decrease in velocity towards the lower section of the Fruholmen Formation (Krabbe Member) which is essentially shale, underlain by shaly sandstones of the Snadd Formation. This is due likely to a change in lithology (elastic property) from the quartz cemented sandstones of the upper Reke Member to underlying pure shales of the Krabbe Member. This variation is more evident in well 7122/6-1 (Fig. 3.10).

After correcting for exhumation, at depths greater than 3100 m (with the exception of well 7122/2-1), well log derived velocities abruptly deviates further from all published and unpublished compaction curves (Fig. 3.20b). Average velocity in the Kolje Formation is about 3100 m/s at a depth of 2775 m but increases to about 4068 m/s at 3081 m in the Stø Formation leading to a velocity increase of 1293 m/s over a distance of 306 m (Fig. 3.20b). This suggests another mechanism responsible for the change in elastic rock properties

revealed by the rapid velocity increase over a relatively small depth interval. Mechanical compaction from vertical effective stress alone cannot explain such a significant change. Only chemical compaction (predominantly quartz cement) can result in an abrupt change in velocity gradient by stiffening the sediment grain framework while its incompressibility is increased resulting in an increase in velocity.

Present day geothermal gradients do not vary much across the study area with an average of about 30° C /Km (Laberg et al., 1998) coupled with no significant lateral depositional age variation in the Triassic Formations. Thus the high degree of scatter in velocities between 1500 and 2700 m when all four wells are plotted together (Figure 3.20a) is due to the varying burial depths coupled with the lateral and vertical changes in textural and mineralogical composition resulting from different sediment provenance particularly during the Triassic (Worsley, 2008) partly due to the complex interactions between tectonic subsidence, fault reactivation and sediment supply influencing the basin infill (Glørstad-Clark et al., 2010).

A unique burial depth will therefore be misleading to use as reference depth to distinguish between mechanical and chemical compaction in the entire area as we see differences in depth and temperatures for the transition zone (TZ) from one compaction regime to the other (Table 3.2) both at present day and when corrected for exhumation. This is a result of the structural style and differential uplift across the study area even between the relatively closely spaced wells on the Tornerose prospect.

Table. 3.2 Transition zones (TZ) from mechanical to chemical compaction with the corresponding temperatures of transition for five wells both at present day depth and temperatures and after correcting for exhumation respectively.

Wells	TZ depth at Present day (m)	TZ temperature at present day (°C)	TZ depth before exhumation (m)	TZ temperature before exhumation (°C)
7123/4 – 1A	1530	45.9	3130	93.9
7122/6 – 1	1480	44.4	2980	89.4
7122/6 – 2	1460	43.8	2910	87.3
7122/2 – 1	1445	43.4	2645	79.4
7122/4 – 1	1713	51.3	3313	99.4

Analysis showed that sands and shales compact along different gradients (Fig. 3.13). A cross plot of Vs versus Vp actually reveals a lithologic differentiation between sands and shales (Fig. 3.14). Prolific sands of the Stø Formation have higher porosity when compared to the feldspathic lithic arenites of the Snadd Formation with and increased clay content. This increases the probability of clay occurring as pore fills resulting in higher Vp. The clays can also be distributed in the Formation in several ways such as structural clays, coated clays and laminar clays. These different modes of occurrences result in quite different effective medium parameters and consequently on the acoustic velocities. Comparatively, the higher porosity in the Stø formation makes it acoustically softer resulting in lower velocities. Vs and Vp are quite useful both as lithology and pore fluid indicators. An attribute cross section of the Vs versus Vp cross plot reveals that the Triassic Snadd sequence is dominated by shaly sands apart from the tight Carnian sandstone at 2230m BSF (Fig. 3.15). This seems to reflect the complex basin infill history as depicted by Glørstad-Clark et al. (2010). In siliciclastic rocks, this cross plot can be used as a frame indicator.

3.5.2 Exhumation

Employing the difference between present day burial of a reference unit such as, the Stø Formation, and its maximum burial prior to exhumation as the net uplift (Doré and Jensen, 1996) is of particular interest here because this is a major controlling aspect of compaction (both mechanical and chemical), diagenesis, source rock maturation , cap rock integrity and hydrocarbon migration .

Compaction based on well data reveals that below depths of approximately < 3.3 km, after correcting for exhumation, natural shales compact more than experimentally compacted Kaolinite – silt mixtures at the equivalent effective stress level (Fig.3.18b). High velocities of the naturally compacted shale, (Fig.3.18b) after correcting for exhumation, could on one hand be explained by the variability of mineralogy and textural composition of shales such that, velocity – depth trends vary greatly in different types of shales (Storvoll et al., 2005). Also early cement at shallow depths sourced from carbonate stringers (Dallan et al., 1988) and/or biogenic silica (alteration of amorphous biogenic silica Opal A to Opal CT at lower temperatures) found throughout the A1 interval (Fig.3.11) could remarkably influence elastic rock properties. Carbonates have a higher kinetic precipitation rate, as such the dissolution of carbonates may be the rate limiting process, hence its chemical compaction is rather a

function of effective stress (Bjørlykke et al., 2004). Thus chemical compaction of carbonate sediments is very different from siliciclastic sediments. Correcting for exhumation does not actually reverse the chemical changes that these rocks had undergone while at higher depths. Therefore, an aspect of cementation will be present in the natural samples, which cannot be compensated for in the experimentally compacted samples.

This deviation from the compaction curve with a well-characterized mineralogical composition, Mondol., (2011) (personal communication), (Fig. 3.20b), suggests a changing mineralogical and textural composition of the natural sediments with more coarser clastics with depth within the Adventdalen Group supported by similar changes in the density logs. This indicates that at this depth interval, vertical effective stress is the driving mechanism for mechanical compaction constrained by changing mineralogy.

For a well-defined lithology, experimental data can conveniently be used to calibrate natural mechanical compaction trends and provide an enormous insight in predicting the elastic properties and reservoir qualities of rocks buried below 1530m BSF (present depth) in well 7123/4-1A, and across the study area. After correcting for Tertiary exhumation, the higher velocity – depth gradients in the well data than published compaction data is due to overconsolidation explained by the burial history of the area.

However, there are some uncertainties such as with an elaborate estimation of exhumation though the estimates obtained here infer a general increase in magnitude of exhumation towards the east. Some of the frequently applied methods in uplifted offshore areas include evaluating the displacement of rocks within the frame works of tectonics using subsidence curves, thermal analysis using vitrinite reflectance and fission track data, stratigraphy using section correlation, and compaction analysis using well log derived velocity data.

3.5.3 Compaction in Source Rocks

Density increases steadily with depth for all five wells (Fig. 3.10). However, a density inversion from approximately 2.6 g/cc at 1600m to about 1.7 g/cc at 1700 m depth corresponds to the 90m thick organic rich Hekkingen Formation (Fig. 3.11). This results from both the physical properties of kerogen and overpressure. Pore pressures higher than hydrostatic recorded at the top of the Hekkingen Formation (NPD Factpage. 2011) could most likely have been generated during rapidly subsiding low permeability sediments under anoxic conditions such that pore fluid pressure cannot attain hydrostatic equilibrium. This relates to a decrease in vertical effective stress resulting in mechanical under-compaction.

This could probably also partly explain the good reservoir qualities in the underlying Stø reservoir sandstone due to a lower degree of compaction. That is, if higher porosity and permeability is found in this reservoir after correcting for exhumation, at depths > 3km (Fig. 3.20b), then overpressure may likely have started to build up at a relatively shallow depth (approximately < 1.5 km) when the Hekkingen Formation was still undergoing mechanical compaction during a period of relatively rapid subsidence. Expulsion of liquid hydrocarbons from kerogen and mineral dehydration could enhance fluid flux generated by compaction, however this extra fluid flux will have a little impact on overpressure build up (Mondol, 2008b).

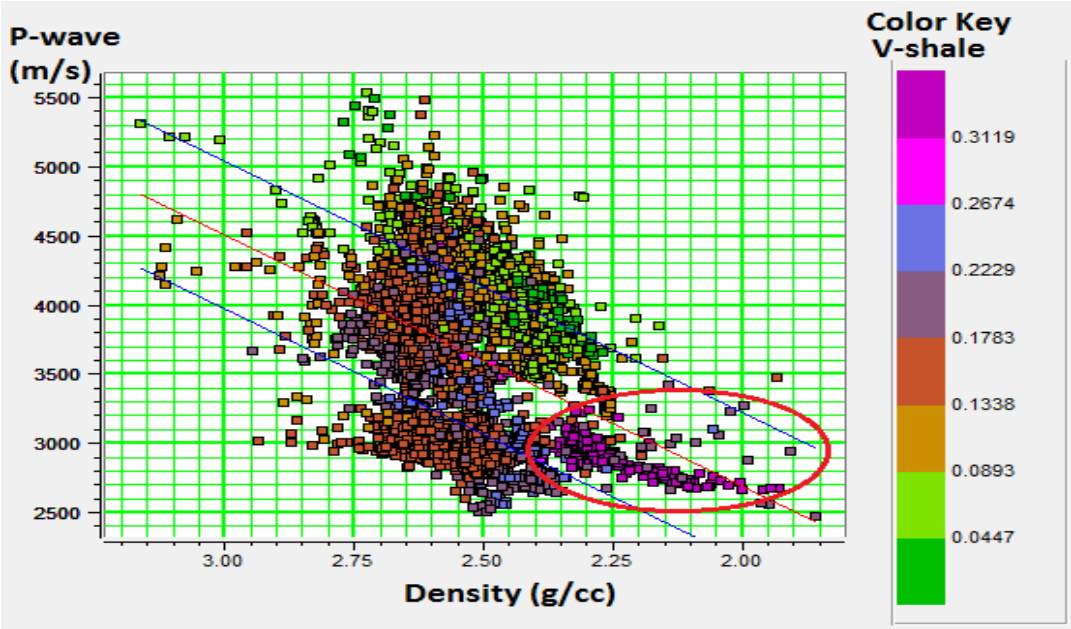

Fig. 3.23 Cross plot of P-wave velocity (m/s) versus Density (g/cc) colour coded with V-shale. The highlighted area (red circle) depicts low density and velocity in the organic rich and overpressured Hekkingen Formation.

Across the entire area, the Hekkingen Formations exhibits the lowest density and velocity (Fig. 3.23). Density and velocity inversion can be due to a number of factors such as the intrinsic physical properties of a three dimension (3D) kerogen network (Philippi and Cordell, 1974), low aspect ratio pores parallel to bedding due to transformation of kerogen to liquid and gaseous hydrocarbon resulting in collapse of the kerogen network (Pepper and Corvi, 1995, Vernik and Liu, 1997). However, kerogen is particulate organic matter and actually load bearing (Palciauskas, 1991) though it is relatively soft compared to the surrounding mineral matrix. With increasing temperatures, oil and gas is generated the kerogen now becomes part of the pore fluids thus a decrease in the volume of solids while

the volume of liquids in the system increases. This also transformation influences the rate of compaction in source rocks with high organic contents as in the Hekkingen Formation.

3.5.4 Uncertainties

Rock property analysis is entirely based on petrophysical well logs. At relatively shallow depths below 1530m BSF, the study area is predominantly composed of mud rocks (Fig. 3.13) from different depositional environments. This implies the clay mineralogy and textural relationships may likely vary as well. This depth level has been deduced to corresponding to mechanical compaction. Several previous studies involving mudstone compaction trends (Fig. 3.24) and physical properties have shown the variability within mud rock compaction depending on the clay mineral type, particle size, total amount of clays, sand and silt particles present (Bjørlykke, 1998; Mondol et al., 2008b; Storvoll et al., 2005). These variations also imply that velocity will also be influenced by the mineralogy, texture and micro-fabric (Fawad et al., 2010).

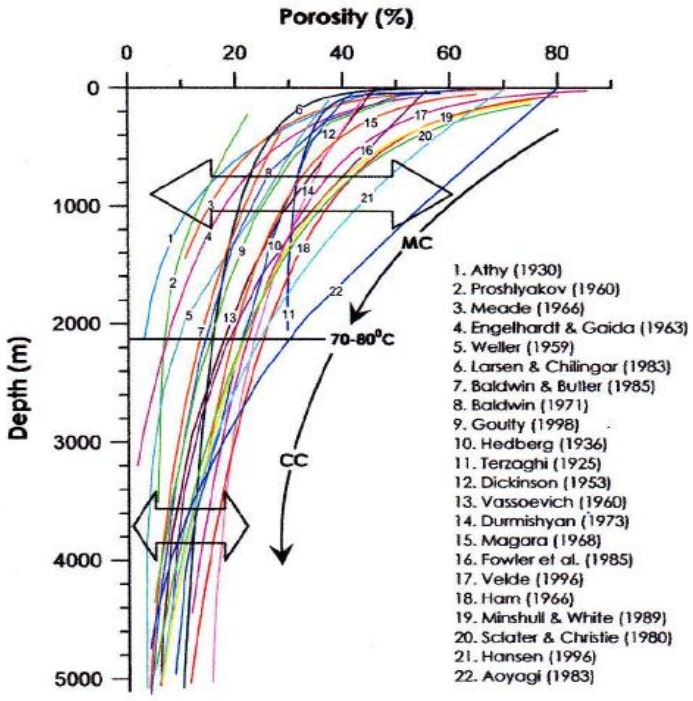

Fig. 3.24 Variability in mudstone compaction trends. Variations are prominent in the mechanical compaction. After Mondol et al., (2008b).

An integrated use of other rock property analytical techniques such as scanning electron microscopy (SEM) and X-ray diffraction (XRD) within this study would give a more

quantitative mineralogical constrain. This would particularly illuminate the suggested smectite to illite transformation (Eq. 3.3) as depicting the transition zone from mechanical to chemical compaction at 1530m BSF (in well 7123/4-1A) and across the study area.

Adequate control of sediment composition and mineralogy will also narrow the margin of uncertainty vis-a-vis estimation of the magnitude of Cenozoic exhumation when employing the approach used herein. A good number of studies have been carried out in the area to quantitatively estimate the exhumation employing varying approaches and results (Liu et al., 1992, Ohm et al., 2008, Corcoran and Doré, 2005). This ambiguity vis-a-vis evaluation and estimates from several other authors (Liu et al., 1992, Ohm et al., 2008, Japsen and Chalmers, 2000) could probably be due to differences in reference baseline and estimation methodology. Incorporating several approaches will reduce the margin of uncertainty.

CHAPTER 4: AVO/AVA MODELING

4.1 Introduction

Seismic wave propagation and eventual signature is a direct result of the seismic properties of the media (rocks) through which it propagates. This is in relation to the sediment depositional environment, extent of compaction and burial history. A good understanding of the geologic framework is of prime importance in carrying out successful amplitude-versus-offset (AVO) or amplitude-versus-angle (AVA) modeling. These seismic properties are; P- and S-wave velocities, bulk density (ρ_b), Vp/Vs ratio, Poisson's ratio (σ), impedances (I_p and I_s), bulk modulus (K), shear modulus (μ) and Lame's parameter (λ).

AVO/ AVA modeling and analysis are the evaluation of reflectivity as a function of offset. It has been widely used initially as a method of validating seismic amplitude anomalies associated with gas sands (Ostrander, 1984). However the success rate has not been correspondingly high as most often the gas sands yielded amplitudes with lower impedance than the surrounding shales and showed reflection coefficients that actually increased with offset. Given that reflections from gas sands show variable AVO characteristics, proper AVO analysis presents a robust tool for determining reflections that are not directly related to anomalous (bright spots) strong reflections on stacked seismic data. There exists several ways to generate, process and analyse AVO synthetic data such as: single-interface modelling, single-gather modeling, 2D stratigraphic modelling and 2D full wave elastic equation modelling (Li et al., 2007). Another approach which is used herein is to develop a half-space model by averaging the elastic properties of the cap rock and reservoir interval of interest. These averaged properties are used in the Zoeppritz (1919) equation.

The main objectives of this chapter are to evaluate reflectivity at the top of the Stø and Snadd reservoir interval as a function of offset/ angle at in-situ condition. The in-situ pore fluids will be replaced with different hydrocarbon fluids with different properties based on the Gassmann's equations and reflectivity at the top of these reservoirs will be re-evaluated. Amplitude anomalies at the top of these reservoir sands with different pore fluid scenarios will then be classified based on the classification scheme put forward by Rutherford and Williams (1989). Sensitivity analysis will be performed using the Stø reservoir interval to investigate the effects of changes in pore fluid compressibility and saturation effects on

synthetic seismograms and AVA character. To achieve these targets, a careful background understanding of seismic theory and AVO modeling is essential.

4.2 Theoretical Background

Several approaches are used in seismic exploration. The most widely used techniques are based on seismic refraction and/ or reflection. However, this study will focus on the seismic reflection method. The following theoretic background gives a succinct and basic understanding of the principles upon which AVO/AVA modeling is based. These principles will directly be applied throughout the methodology while certain assumption will have to be made to be able to constrain the resultant model.

4.2.1. Reflectivity Series

This is can be thought of as a time series of spikes whereby each spike represents a zero offset P-wave reflection coefficient. Reflectivity is one of the fundamental physical concepts in seismic method. It is obtained from the acoustic impedance by dividing the difference in acoustic impedances by the sum of acoustic impedances between two bounding layers. However, acoustic impedance is the product of the velocity and density within each layer. The reflectivity series is often interpreted as the impulse response of the earth's filter.

4.2.2. The Convolutional Trace Model

This model can be thought of as a mathematical combination of two signals in order to obtain a modified third signal. Convolution in time corresponds to multiplying the amplitude spectra and adding the phase spectra in the frequency domain.

However, the simplest version of this model is based on a number of assumptions which are:

- A horizontally layered earth model.
- Normally incident plane waves (implying no shear contributions).
- A stationary source pulse without any change with depth.
- Noise contribution is neglected.

A seismic trace, x(t), being a time measurement corresponding to a source / receiver pair, is a result of a linear convolution between a the source pulse S(t) (wavelet) and the earth's reflectivity series r(t) (Fig.4.1).

$$x(t) = s(t) * r(t) \qquad \text{(Eq. 4.1)}$$

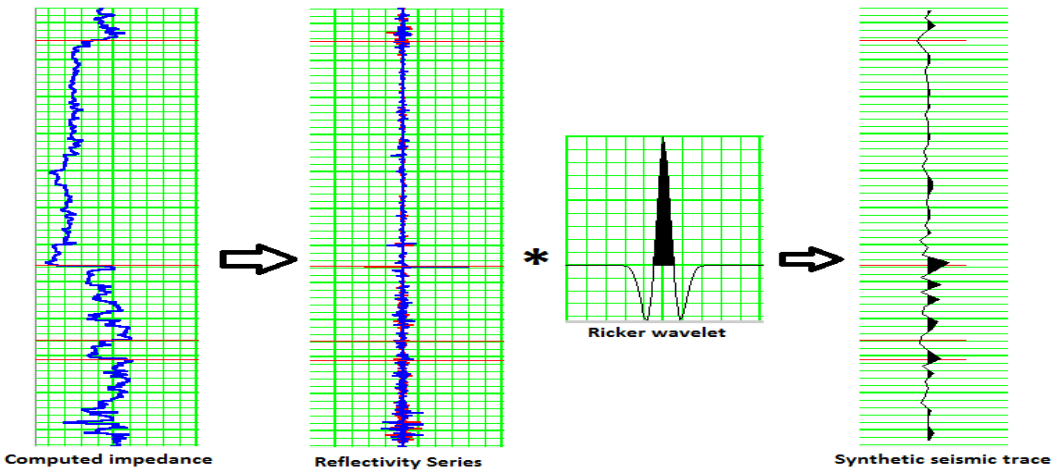

Fig. 4.1. Schematic illustration of the Convolutional trace model. The pulse used is a zero-phase Ricker wavelet with peak frequency at 45 Hz.

4.2.3. Zoeppritz Equation and Aki-Richard Approximation

Variations in reflection amplitudes as a function of offset (angle) are due to mode conversion at a seismic reflector. This depends on the contrast in elastic rock properties across this interface and on the angle of incidence. Zoeppritz equations are in a general approach employed to decipher how these amplitudes vary with offset (angle) for elastic material such that the physical properties of the rocks across the seismic reflector can be deduced. However, these equations (Zoeppritz, 1919) involve a myriad of expressions to relate amplitude to the rock parameters and were thus simplified by the Aki – Richard approximation in order to meet thesame purpose but with a more practical approach.

Zoeppritz Equation

Mode conversion (energy partitioning) occurs when the incident angle is greater than zero as shown below. However according to Snell's law, the angles of incidence(θ_1) and refraction (θ_2) is equivalent to the ratio of the phase velocities(V_1 and V_2) and equal to the refractive indices (n_1 and n_2) respectively. If only P-P reflections are measured, at the reflecting

interface, the measurements will indirectly contain shear-wave information. Snell's law is represented as:

$$\frac{\mathrm{Sin}\theta_1}{\mathrm{Sin}\theta_2} = \frac{V_1}{V_2} = \frac{n_1}{n_2} \qquad \text{(Eq. 4.2)}$$

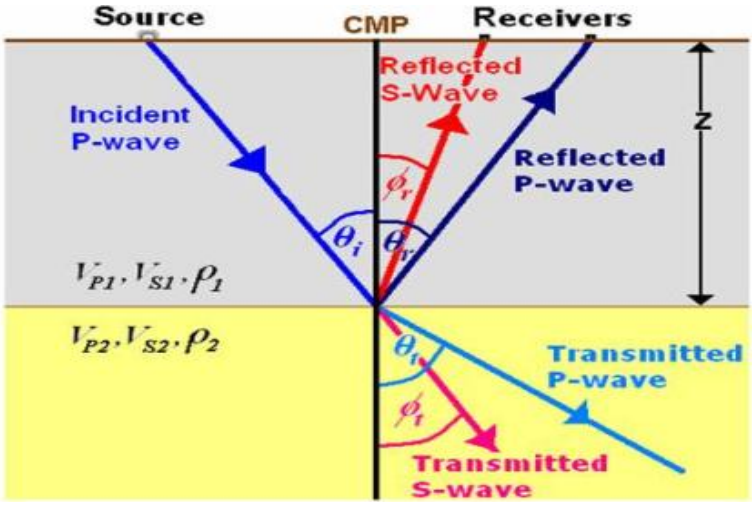

Fig. 4.2 Mode conversion (energy partitioning) of an incident P-wave producing P and S reflections and transmissions. The reflected angle of the converted S-wave is smaller than the reflected angle of the P-wave.

From Figure 4.2, the P-P reflection coefficient is obtained using the Zoeppritz equation. The amplitudes of reflected and transmitted waves are derived based on the concept of conservation of stress and displacement across the interface. These amplitudes are related to the rock parameters through quite complicated algebraic expressions.

Aki - Richard's Approximation

This is a liner approximation that assumes small perturbations in elastic properties. It is written in three terms involving P-wave velocity (Vp), S-wave velocity (Vs) and density (ρ). Average properties and property differences between two media are used in the expressions. The difference between the Zoeppritz exact solution and the Aki-Richard's approximation is quite small when the zero offset reflectivity is << 1 (Li et al., 2007). Using a linearized approximation and keeping only first order terms, (Aki and Richards, 1980) the P-P reflection coefficient $R_{pp}(\theta)$ is given as follows:

$$R_{pp}(\theta) = \frac{1}{2}\left[\frac{\Delta V_p}{V_p} + \frac{\Delta\rho}{\rho}\right] - 2\left(\frac{V_s}{V_p}\right)^2\left[2\frac{\Delta V_s}{V_s} + \frac{\Delta\rho}{\rho}\right]\sin^2\theta + \frac{1}{2}\frac{\Delta V_p}{V_p}\tan^2\theta \qquad \text{(Eq. 4.3)}$$

For small angles, tan θ ≈ sin θ and the ratio $V_p/V_s = 2$. Equation 4.3 is further simplified by the Wiggens or Gelfand's approximation as:

$$R_{pp}(\theta) = R_p + G\sin^2\theta \quad \text{(Eq. 4.4)}$$

Where R_p is the AVO intercept and G is the gradient.

$$G = R_p - 2R_s \quad \text{(Eq. 4.5)}$$

R_p and R_s represent the zero offset reflection coefficients for P- and S-waves respectively and are expressed as:

$$R_p = \frac{1}{2}\left[\frac{\Delta V_p}{V_p} + \frac{\Delta\rho}{\rho}\right] \quad \text{(Eq. 4.6)}$$

$$R_s = \frac{1}{2}\left[\frac{\Delta V_s}{V_s} + \frac{\Delta\rho}{\rho}\right] \quad \text{(Eq. 4.7)}$$

The averaged properties and differences used in these expressions are given as:

$$V_p = \frac{(Vp_1 + Vp_2)}{2} \quad \text{(Eq. 4.8)} \qquad \Delta V_p = Vp_2 - Vp_1 \quad \text{(Eq. 4.9)}$$

$$\rho = \frac{(\rho_1 + \rho_2)}{2} \quad \text{(Eq. 4.10)} \qquad \Delta\rho = \rho_2 - \rho_1 \quad \text{(Eq. 4.11)}$$

$$V_s = \frac{(Vs_1 + Vs_2)}{2} \quad \text{(Eq. 4.12)} \qquad \Delta V_s = Vs_2 - Vs_1 \quad \text{(Eq. 4.13)}$$

Two separate sections can then be generated from these AVO quantities. That is an Intercept (R_p) stack and a gradient (G) stack. However combined R_p and G sections can also be constructed whereby bright spots are enhanced with weaken normal lithologic events. That is:

$$R_P + G = 2(R_P - R_S) \quad \text{(Eq. 4.14)}$$

Shear wave reflectivities are enhances accordingly as follows:

$$R_S(R_P - G) = 2R_s^2 \quad \text{(Eq. 4.15)}$$

4.2.4 AVO Reservoir Sand Classification Scheme

The Amplitude Versus Offset (AVO) signature of gas sands are largely controlled by the normal incidence reflection coefficient (R_o) and the contrast in Poisson's ratio at the interface between the cap rock (shales) and the reservoir sands (Rutherford and Williams, 1989). The P-wave reflection coefficient varies greatly with angle of incidence. At small incident angles, the relative changes in the reflection coefficient are seen to be large when the contrast in Poisson's ratio between the two media is large (Ostrander, 1984) . As it is the case with parts of the study area, the contrast in Poisson's ratio between the Hekkingen and Stø Formations is quite large resulting in detectable amplitude changes.

Poisson's ratio denoted (σ) is defined as a measure of the compressibility of a material perpendicular to applied stress. Alternatively, it is the ratio of latitudinal to longitudinal strain. For an isotropic elastic material, dynamic determination of Poisson's ratio can be calculated as it relates to the P-wave (Vp) and S-wave (Vs) velocities through the following equation:

$$\sigma = \frac{\left(\frac{Vp}{Vs}\right)^2 - 2}{2\left[\left(\frac{Vp}{Vs}\right)^2 - 1\right]} \quad \text{(Eq. 4.16)}$$

Reflection coefficient (R) is the ratio defining the amplitude (energy) of a reflected wave to the incident wave. For a normal incident wave, the reflection coefficient (R) has typical values ranging from −1 to +1 and can be expressed as:

$$R = \frac{(\rho_2 V_2 - \rho_1 V_1)}{(\rho_2 V_2 + \rho_1 V_1)} = \frac{Z_2 - Z_1}{Z_2 + Z_1} \quad \text{(Eq. 4.17)}$$

Where;

ρ_1 is = density of medium 1, V_1 is = velocity of medium 1, Z_1= Acoustic impedance of medium 1

V_2 is = density of medium 2, V_2 is = velocity of medium 2 and Z_2 = Acoustic impedance of medium 2

For non-normal incidence angles, there exist four independent variables (Ostrander, 1984) exist at a reflecting/ refracting interface controlling the reflection and transmission coefficients between two isotropic materials: (a) the Vp ratio between the two media, (b) the density ratio between the two media, (c) Poisson's ratio in the upper medium and (d) Poisson's ratio in the lower medium

Based on Zoeppritz (1919) equations, Rutherford and Williams grouped gas sands into three classes each of which is defined by their normal incidence reflection coefficient. Only the shale/ sand reflectivity is considered and several factors such as bed tunning, attenuation and propagation effects are not considered in the classification scheme. The different classes are summarised as follows:

Class I: High Impedance Sands

The impedance is higher than the surrounding shales with a large positive value for the zero offset reflection coefficient at the shale/ sand interface. This decrease in magnitude with offset and a polarity change at large offsets / angles. The sands are quite mature, having undergone moderate to high compaction. They are normally associated with areas onshore though in uplifted areas such as in the Barents Sea region, such sands could be expected.

Class II: Near-zero Impedance Sands

The impedance is quite small and identical to that of the encasing material with reflection coefficients values close to zero. It is either a small positive or negative value. This is often difficult to detect in the presence of noise. A large fractional change in reflectivity occurs from near to far offsets. If the reflection coefficient at zero offset is positive, then a polarity change occurs. These sands are often moderately compacted and consolidated. They are generally associated with areas both onshore and offshore.

Class III and IV: Low Impedance Sands

The impedance is lower than the encasing medium. Amplitude anomalies 'bright spots' occur on stacked seismic data with large reflectivities for all offsets. The fractional changes in amplitudes as a function of offset are generally small. No polarity change occurs. For class III, amplitudes increase with offset whereas for class IV, amplitudes decrease with offset (positive AVO gradient). Both are associated with marine environment

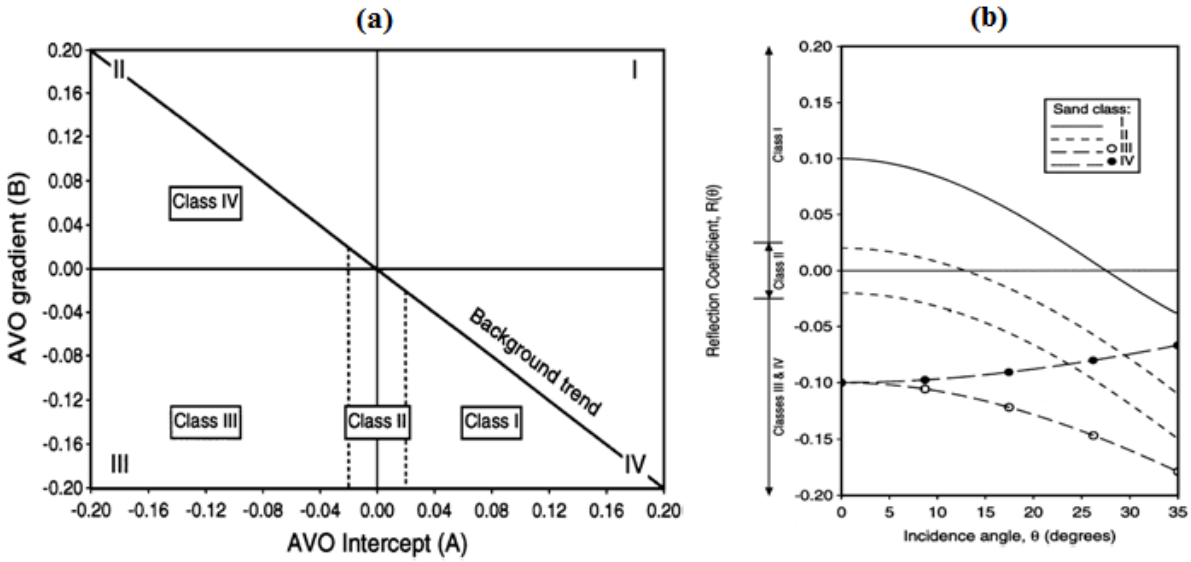

Fig. 4.3 (a) AVO intercept (A) versus Gradient (B) cross plot showing four quadrants. (b) Plane wave reflection coefficients at the top of each Rutherford and Williams (1989) classification of gas sand after (Castagna et al., 1998)

4.2.5 Gassmann's Theory and Fluid Substitutions

The essence of fluid substitution is to model and quantify various fluid scenarios which might explain the observed AVO response. There exist several empirical and heuristic methods of performing fluid substitution, each with its underlying assumptions and limitations. The method employed is based on the Gassmann's (1951) equations. The Gassmann (1951) equation incorporates the saturated bulk modulus (K_{sat}) of a rock to its porosity (φ), the bulk modulus of the porous rock frame (K^*), the bulk modulus of the mineral matrix (K_o) and finally the bulk modulus of the pore-filling fluid(s) (K_{fl}). That is:

$$K_{sat} = K^* + \frac{\left(1-\frac{k^*}{K_o}\right)^2}{\left[\frac{\varphi}{K_{fl}} + \frac{(1-\varphi)}{K_O} - \frac{K^*}{K_o^2}\right]} \qquad \text{(Eq. 4.18)}$$

Modelling the effects of a given fluid type on the AVO signature requires that the reservoir be drained of its initial pore fluid in order to determine the bulk modulus of the porous rock

frame after which fluid substitution is employed and the bulk modulus of the rock saturated with the substituting (new) fluid is calculated. K^* remains unchanged after fluid substitution.

Despite the robustness and general nature of this equation, it is based on a number of assumptions which are: the rock is homogenous, isotropic, well connected pore network; the saturating pore fluid is homogenous. The assumption on fluid immiscibility and homogeneity are thought to be accomplished by systems which have attained phase equilibrium over geologic time (Smith et al., 2003). Final assumption is, low seismic frequencies to allow for pressure equalization on a scale greater than pore dimension and less than the wavelength of propagating wave.

The bulk modulus of an isotropic rock is the ratio of hydrostatic stress to volumetric strain and obtained from wire line log analysis using P- and S-wave velocities and bulk density (ρ_b) measurements by employing the following equation:

$$k_{sat} = \rho_b \left(V_p^2 - \frac{4}{3} V_s^2 \right) \quad \text{(Eq. 4.19)}$$

The bulk density (ρ_b), being an important input parameter in performing fluid substitution, is however related to the fluid density (ρ_{fl}), porosity (φ), and grain density (ρ_g) through the following equation which can also be solved to obtain the porosity:

$$\rho_b = \rho_g(1 - \varphi) + \rho_{fl}\varphi \quad \text{(Eq. 4.20)}$$

Given the parameters in Equations 4.19 and 4.20, P-wave velocity is however calculated as:

$$V_p = \sqrt{\frac{K_{sat} + \frac{4}{3}\mu}{\rho_b}} \quad \text{(Eq. 4.21)}$$

Fluid parameters also have to be analyzed carefully as this yield misleading outputs for the bulk modulus after fluid substitution. Therefore a priori knowledge of both the in-situ and substituting fluid's bulk modulus (K_{fl}) and density (ρ_{fl}) is necessary. Following the

assumption of a homogenous saturation, fluid parameters are calculated using the iso – stress (Reuss) harmonic average for a two phase water-hydrocarbon system as:

$$K_{fl} = \left[\frac{S_w}{K_w} + \frac{(1-S_w)}{K_{hc}}\right]^{-1} \quad \text{(Eq. 4.22)}$$

For the fluid density, we have:

$$\rho_{fl} = S_w\rho_w + (1 - S_w)\rho_{hc} \quad \text{(Eq. 4.23)}$$

Where: K_w is the bulk modulus of water, Sw is the water saturation and K_{hc} is the bulk modulus of hydrocarbon fluid.

Mineralogical composition of the rock is required to calculate the bulk modulus of the mineral matrix (K_o). This is commonly obtained from core samples, in the absence of which the constituent mineral fractions are approximated using the gamma ray log (V_{clay}) considering only quartz and clay end members. K_o is calculated from the volume fractions of the rock and elastic moduli of the various phases using several effective medium models such as Voigt-Reuss-Hill (VHR) average or the Hashin – Shtrikman (HS) average.

The shear modulus (μ) defined as the ratio of shear stress to shear strain is a rock frame parameter which is rather independent on the pore fluid(s), there by remains unchanged after fluid substitution. It is computed using the following equation:

$$\mu = \rho_b Vs^2 \quad \text{(Eq. 4.24)}$$

Consequently, Shear wave velocity can be calculated by rewriting Equation 4.24 as:

$$V_s = \sqrt{\frac{\mu}{\rho_b}} \quad \text{(Eq. 4.25)}$$

4.3 Methodology

The main inputs for the forward seismic modeling are P- and S-wave velocity and density. Half-space models are developed by averaging these parameters both in the cap rock and reservoir interval of interest. Shear – wave velocity (Vs) is an important frame indicator as a stand-alone parameter. When combined with compressional –wave velocity (Vp), it could serves as a lithology indicator in seismic modelling and AVO analysis. Though not often measured, Vs information about a target reflector can still be determined indirectly. A pressure wave incident at a target reflector generates four waves: transmitted Vs and Vp, and reflected Vs and Vp.

4.3.1 Shear Wave Velocity (Vs) Estimation

Measured Vs log is available only from well 7123/4-1A. In wells 7122/6-1, 7122/6-2, 7122/4-1 and 7122/2-1, a Vs log is generated using Vp log as an input parameter. This is done using equations by Castagna et al. (1985) and Krief et al., (1990) in this study.

Castagna et al., (1985): The 'mudrock line' derives Vs by applying a linear transform to an input Vp log. Velocities are in kilo meter per second (Km/s)

$$Vs = 0.862\,Vp - 1.172 \qquad \text{(Eq. 4.26)}$$

This equation demonstrates a quite simple systematic and straight forward relationship between Vp and Vs particularly for water bearing clastics whereby Vs is approximately linearly related to Vp and the Vp/Vs ratio decreases with increase in Vp (Castagna et al., 1985).

Krief et al., (1990): however put forward a linear relationship between the squares of Vp and Vs in clean Formations expressed as:

$$Vs^2 = a\,Vp^2 + b \qquad \text{(Eq. 4.27)}$$

Where 'a' and 'b' are regression coefficients for different lithologic zones

The measured Vs in well 7123/4-1A is compared with Vs as given by the Castagna et al., (1985) ($V_{s\text{-Castagna}}$) and Krief et al., (1990) ($V_{s\text{-Krief}}$) equations. The purpose is to

approximate which of the calculated Vs closely fits the measured Vs and could be used for analysis in areas without any measured Vs. Upon close examination of these logs (Fig.4.4a) within the target zone(s), no definite pattern as to which of the predicted Vs closely fits the measured Vs. For further investigation, an amplitude picks analysis is done using each of the Vs types at the top Stø reservoir at in-situ scenario (Fig. 4.4b), while keeping all other parameters constant. It becomes apparent that $Vs_{\_Castagna}$ has a relatively closer fit with the measured Vs from zero offset to 750m offset after which it becomes higher but still with a relatively better match. Though both Vs predictors show a good correlation with each other for all offsets, higher amplitudes than the measured Vs are observed for increasing offsets. $Vs_{\_Castagna}$ is used for further analysis in areas where there is no measured Vs as it showed relatively better correlation with the measured Vs.

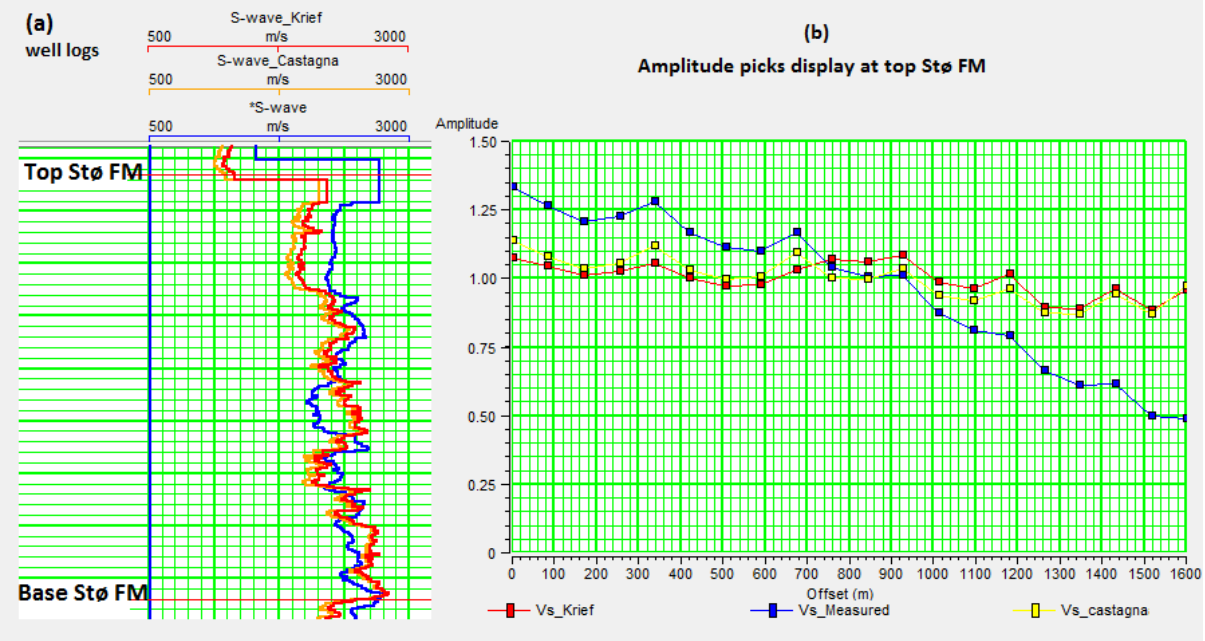

Fig. 4.4 Similarities and differences a between measured Vs, Vs_Castagna and Vs_Krief (a) comparison based on wireline logs within the Stø reservoir (b) comparison of the amplitude response at the top of the reservoir.

4.3.2 Water Saturation (S_w)

S_w is the fraction of pore volume filled with water. Based on Archie's equation, it is computed using the Formation resistivity factor, the resistivity of the Formation water and the true resistivity of the Formation from the wireline log. However the Formation resistivity

factor is dependent on the porosity and two empirical constants one of which is multiplicative and the other is an exponent. These constants are formation dependent.

$$S_w = \sqrt{a\varphi^m \frac{R_w}{R_t}} \quad \text{(Eq. 4.28)}$$

Where: a is cementation factor, φ is porosity, m is cementation exponent, R_w is resistivity of Formation water and R_t is true resistivity.

4.3.3 Density to Porosity Transform

Density to porosity transform is applied to well 7122/4-1 where porosity (φ) is calculated by using a matrix density (ρ_{ma}) of 2.65, a fluid density ($\rho_{fl)}$ of 1.09g/cc and the observed log density (ρ_{log}) as follows:

$$\varphi = \frac{\rho_{ma} - \rho_{log}}{\rho_{ma} - \rho_{fluid}} \quad \text{(Eq. 4.29)}$$

4.3.4 Wavelet

A wavelet is a mathematical representation of a source function. It is both time varying and complex in shape and can be analyzed as a time series in the time domain or in the frequency domains as a phase or amplitude spectrum. Ideally, a wavelet would be a spike in time with a flat amplitude spectrum. There are several types of wavelets, two of which are commonly used.

Minimum phase wavelets: whereby the energy concentration is at the start of the wavelet. There is no negative energy at time zero, implying that the wavelet is causal.

Zero phase wavelets: it is time symmetrical (non-causal) with negative energy arriving before time zero. Though physically not realistic, it is used by virtue of its resolving power.

The Ricker zero phase wavelet is used herein to generate synthetic seismograms. It consists of a central peak and two side lobes. It has a dominant frequency at 45Hz, a sample rate of 2(ms) and a wavelet length of 200m. Basically this wavelet is defined by its peak frequency in the amplitude spectrum or the dominant period in time. The wavelet period is the time interval from one trough to the other. A broad amplitude spectrum results in a more compressed pulse in time indicating an increase in the resolution (Fig. 4.5a). A zero phase

wavelet is desirable because since the energy is concentrated at a positive peak, a convolution with a reflection coefficient yields a better resolution of the reflection.

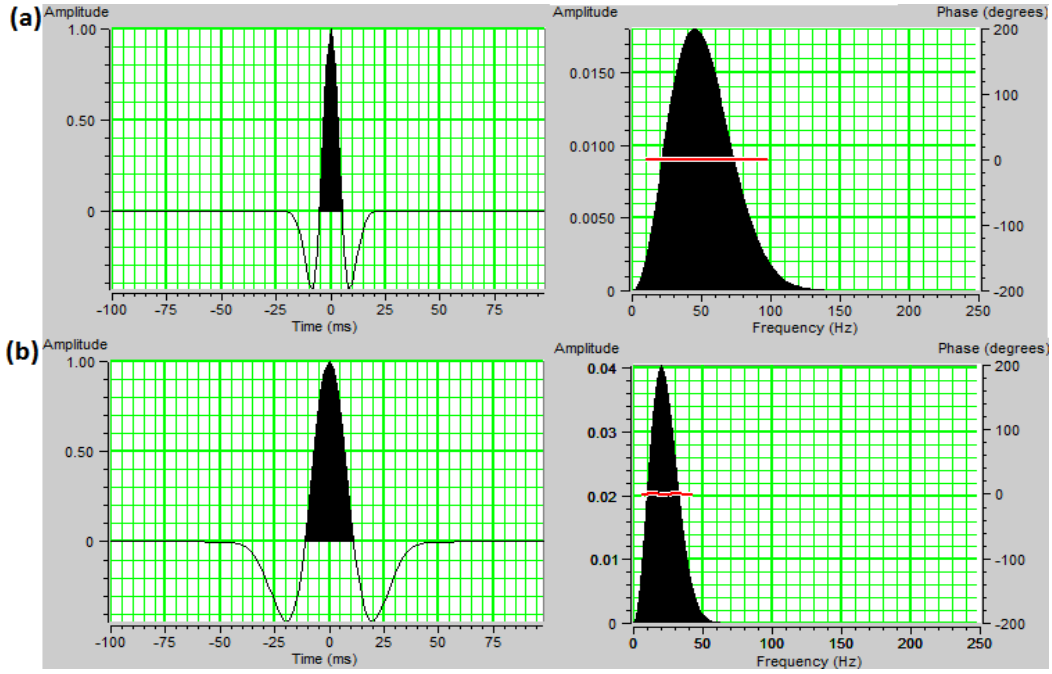

Fig. 4.5 Ricker zero phase wavelets in time and frequency domain for different parameters. (a) The dominant frequency is at 45Hz, sample rate of 2(ms) and wavelet length of 200m. It is used in this study. (b) Is a 20Hz wavelet, with a sample rate of 2(ms), a wavelet length of 200m.

4.3.5 Upscaling

Seismic frequency in the Hertz (Hz) range samples large portions of the sub-surface. Thus, elastic properties from seismic data are those averaged over relatively large intervals. Inherent to generating synthetic seismograms is the process of relating the logging frequencies to seismic wavelengths since synthetics correlate well bore-derived rock properties to seismic data. This poses a problem of difference of scale between the logging frequency in the Kilo Hertz (KHz) range and seismic data in the Hz range. There are several blocking models such as the Backus average and traveltime (slowness) average.

Vp, Vs and bulk density logs are blocked in order to keep the low frequency variations thereby allowing the definition of interfaces between various facies. This is most important for this data type as it is observed that the choice of the block size will greatly condition the synthetic output and eventually influence the AVO signature leading to erroneous interpretations. A block size difference of just 3m gives a completely different amplitude

response (Fig. 4.6). A maximum block size of 25m is considered as this corresponds approximately to the vertical seismic resolution. Therefore careful editing of elastic logs and consistency with other petrophysical logs is of prime importance in AVO modelling. To create a reliable model, up scaled parameters should be representative of the actual geologic conditions.

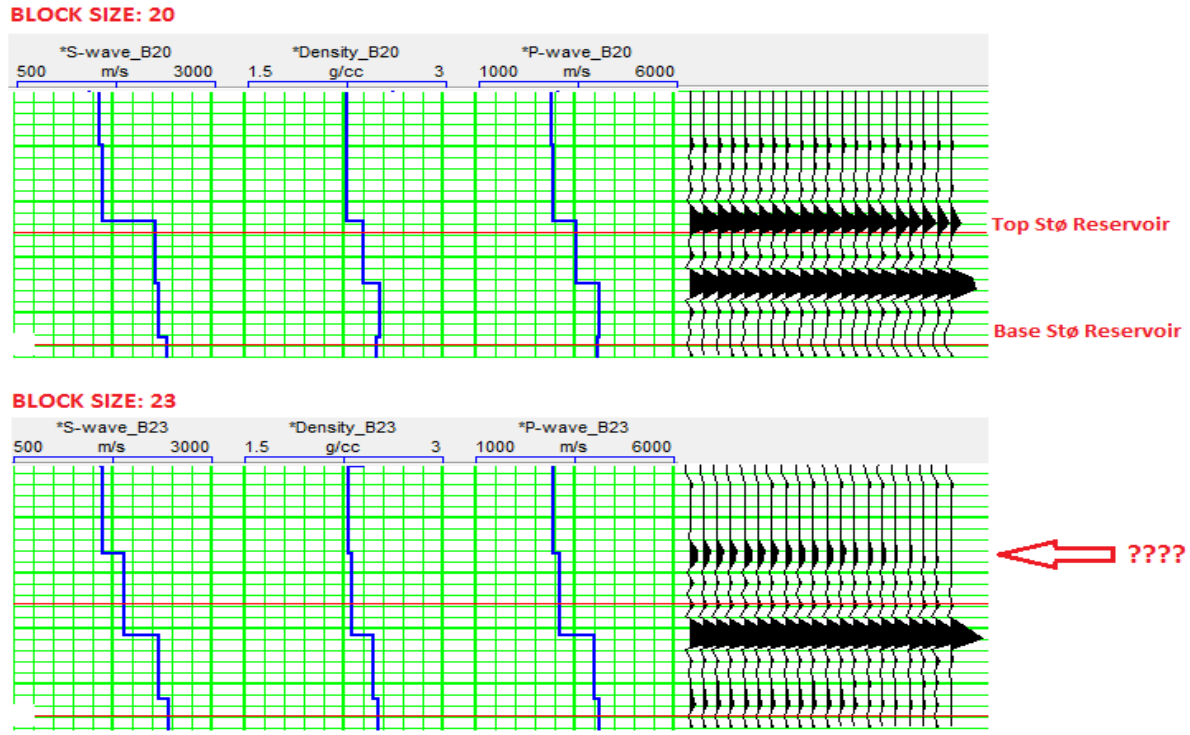

Fig. 4.6 Illustration of the implication of block size on NMO corrected synthetic CDP gathers and eventual AVO signatures. A block size of 20m results in a high impedance AVO signature. While a block size 23m yields a low impedance AVO signature.

4.3.6 AVO/ AVA Modeling

The algorithm used to generate the synthetic seismogram from the blocked logs is based on the Zoeppritz equation. The output synthetic seismogram is directly in reflectivity values and NMO-corrected. Geometrical spreading, transmission loses, anisotropy, thin bed effects and other propagation factors known to affect AVA response are not considered. This method creates and offset or angle dependent synthetic using ray tracing to calculate the incidence angles and the Zoeppritz equation to theoretically calculate the amplitudes.

Amplitude values originating from the top Stø and Snadd potential reservoirs are manually picked and plotted as a function of reflection offset/ angle (Fig. 4.4b). These are however considered as scaled estimates of the P-P reflection coefficient (R_{PP}). By curve-fitting these

picked amplitude values to the theoretical R_{PP} values given by the Zoeppritz equations, estimates of P-wave reflectivities are obtained.

AVA analysis is carried out on reflectivity values from the top Stø and Snadd reservoirs using the two term Aki-Richards approximations to the Zoeppritz equation. The results are plotted based on the Rutherford and William's reservoir sands classification scheme (Fig. 4.3). This procedure is performed for the in-situ scenario of both reservoir intervals.

Pore fluid substitutions based on the Gassmann equations, for extreme cases are performed to model 90% gas and 90% oil scenarios for the Stø reservoir. The assumed 10% water saturation in both models is to approximate for irreducible water saturation. During the substitution of the in-situ fluid by 90% gas, the following petrophysical parameters are used: the matrix is considered to be clean sandstones by default with a bulk modulus of 40 GPa, shear modulus of 44 GPa, and a matrix density of 2.65 g/cc. The hydrocarbon gas type is default such that the bulk modulus is 0.021 GPa and density of 0.1 g/cc.

For the 90% Oil scenario, the matrix properties are kept constant as in the gas case. However the oil properties are also considered by default to have a modulus of 1GPa and a density of 0.75 g/cc.

For the Snadd reservoir, the purpose of modelling Brine – filled reservoir is to nullify the possible influence of varying quantities of gas and oil showings at different depth levels present in the Snadd Formation as reported by the Norwegian Petroleum Directorate. This gives control over the reservoir fluids to enable a further investigation of lithology and depth effects on the resultant AVA response based on the assumptions upon which the model is developed. The properties of brine used are: density of 1.09 g/cc and a modulus of 2.38 GPa.

After substituting the in-situ fluids, the AVA response for each pore fluid model is investigated and the results are plotted using thesame classification scheme as in the in-situ scenario for both the Stø and Snadd reservoirs.

Sensitivity analysis is performed using the Stø reservoir interval with well 7123/4-1A, to investigate how changes in acoustic and elastic rock parameters, influence seismic response eventual AVO signatures. The in-situ scenario (brine) is successively substituted with 10%, 50% and 90% gas saturations. The respective synthetic seismograms are generated and AVA analysis carried out.

4.4 Results

Due to scaling during the conversion of amplitudes to reflectivities, the following scale is adapted particularly for this study to enable classification of the resultant AVA responses:

Table. 4.1 Adapted range of reflectivity values used to classify AVA response.

Reflectivity range	Classification
− 0.035 − 0	Class II
0 − 0.035	Class II P
0.035 − 0.07	Class I

4.4.1 Stø Reservoir

A plot of Rp as a function of angle up to 40° for the top Stø reservoir at in-situ scenario (Fig. 4.7) shows varying but high Rp values from wells 7123/4-1A and 7122/6-1. In Well 7122/6-2, Rp is relatively lower and well 7122/4-1, located about 39km to the west of the other three wells, towards the Snøhvit field, the Stø reservoir rather displays very low Rp. A classification of the AVO response of the Stø reservoir sands at in-situ scenario, oil – filled and gas – filled scenarios are summarized in Table 4.2.

Table. 4.2 Top reservoir sand reflection coefficient versus angle behaviour of the Stø reservoir for different fluid scenarios

Wells	Scenario	Class	Quadrant	Intercept	Gradient
7123/4-1A	In-situ	I	IV	+	-
	Oil	Weak II P	IV	+	-
	Gas	II P	IV	+	-
7122/6-1	In-situ	I	IV	+	-
	Oil	Weak II P	IV	+	-
	Gas	II P	IV	+	-
7122/6-2	In-situ	Weak II P	IV	+	-
	Oil	Weak II P	IV	+	-
	Gas	II P	IV	+	-
7122/4-1	In-situ	II P	IV	+	-
	Oil	II	IV	-	-
	Gas	II	IV	-	-

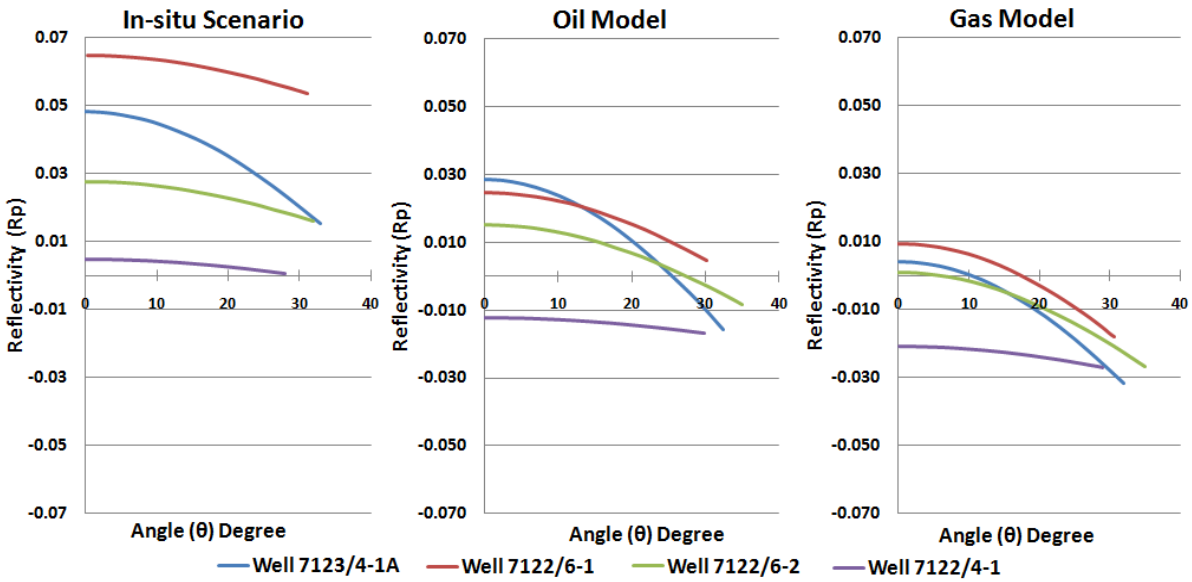

Fig. 4.7 AVA cross plot for four wells at top Stø reservoir at in-situ scenario, Oil model and Gas model with a maximum offset of 40 degrees. Three of the wells yield class I AVO response at in-situ scenario while well 7122/4-1 shows a class II AVO response.

The reflection coefficients progressively decrease from in-situ scenario to Oil model and finally gas model for all four wells with different magnitudes. Well 7122/4-1 actually displays a negative intercept both in the oil and gas models (Fig. 4.8).

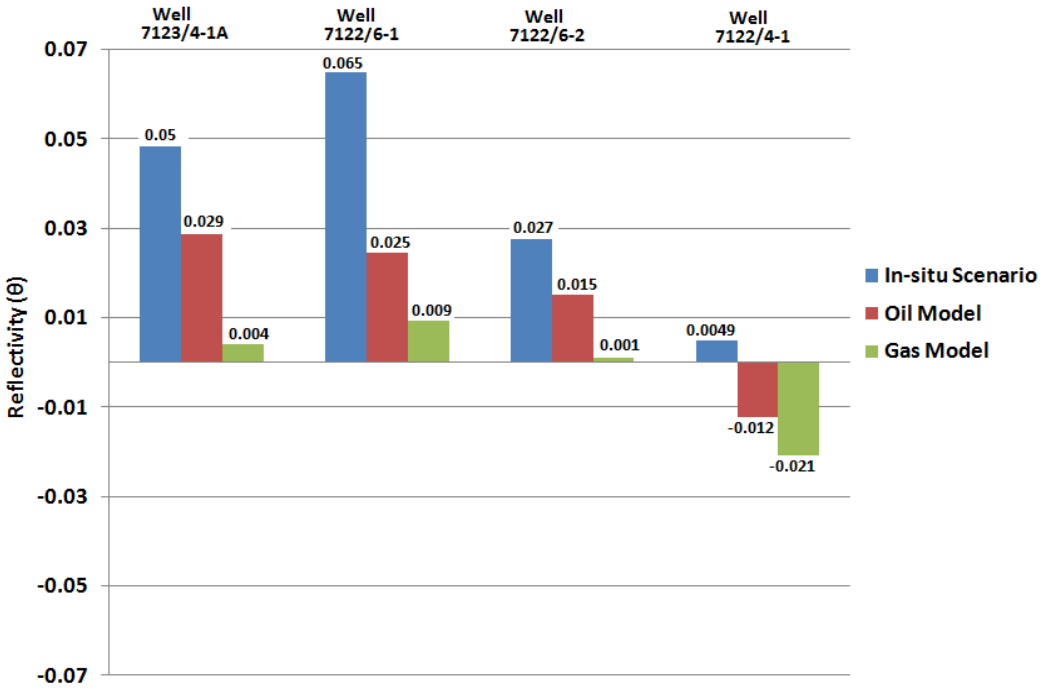

Fig. 4.8 Quantitative analysis of zero-offset reflectivity of four wells at: in-situ scenario, oil model and gas model.

4.4.2 Snadd Reservoir

AVA analysis is also carried out at the top of the Snadd Formation that represents the deeper reservoir horizon in the study area. The AVA responses indicates that these sands have very low (near zero) impedance contrasts with the overlying Akkar Member of the Fruholmen Formation. The reflection coefficients show very small variations from one well to the other apart from well 7122/6-1 which is relatively high. After substituting the pore fluids with 100% brine the output yielded a class II response for all four wells but with an increased magnitude, with respect to the in-situ scenario, both at zero offset and with increasing angle (Fig. 4.9). The purpose of modelling a brine-filled reservoir to eliminate the possible influence of gas and oil showings, then further investigate the possible effects of lithology and depth on the AVO response based on the models assumptions.

Table.4.3 Top reservoir sand reflection coefficient versus angle behaviour of the Snadd reservoir for different fluid scenarios.

Wells	Scenario	Class	Quadrant	Intercept	Gradient
7123/4-1A	In-situ	II P	IV	+	-
	Water	II P	IV	+	-
7122/6-1	In-situ	Weak II P	IV	+	-
	water	II P	IV	+	-
7122/6-2	In-situ	II P	IV	+	-
	water	II P	IV	+	-
7122/4-1	In-situ	II P	IV	+	-
	water	Weak II P	IV	+	-

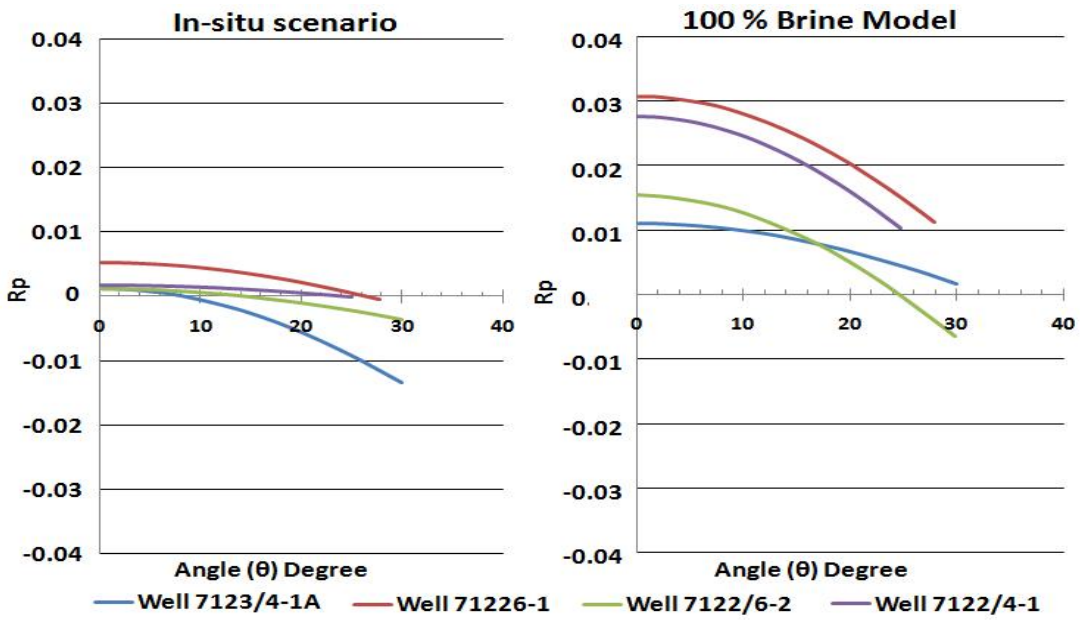

Fig. 4.9 AVA cross plot for four wells for top Snadd Formation at in-situ scenario and after substituting the pore fluid with 100% Brine.

In order to quantitatively illustrate the magnitude of variations in reflectivity, zero offset P-wave reflection coefficients of the all four wells for the two fluid scenarios are plotted as shown in Figure 4.10. It shows a relatively large increase in reflectivity with varying extents (for different wells) suggesting an indication of the possible effects of oil and gas shows on the AVA response.

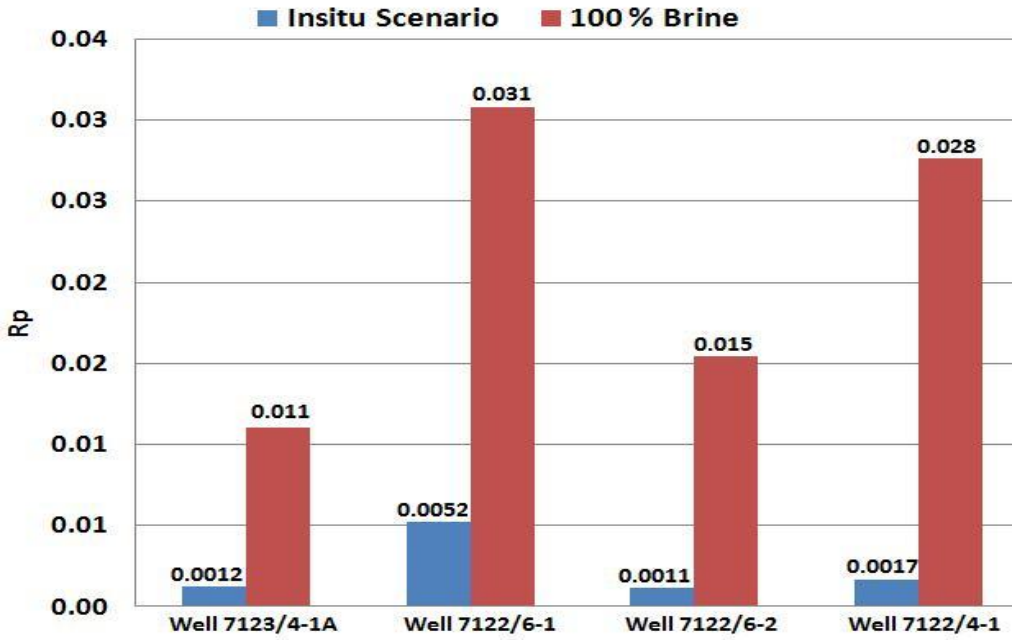

Fig. 4.10 Illustration of zero offset reflectivity for four wells at in-situ scenario (blue) and at 100% brine saturation (red).

4.4.3 Sensitivity Analysis

Using well 7123/4-1A, an investigation of the dependence of seismic signatures and eventual AVO responses on acoustic and elastic rock properties by varying the pore fluid saturation using a two phase water – gas system gives quite interesting results. At the in-situ scenario, the Stø Formation displays a positive reflection coefficient at normal angles of incidence. Introduction of an initial 10% gas significantly results in a visible and direct change in the seismic response. However, increasing gas saturation to 50% yields a very mild change on the synthetics when compared with the 10% scenario. Further increase in the gas saturation to 90% does not lead to a clear change on the synthetics at the top of the reservoir (Fig. 4.11).

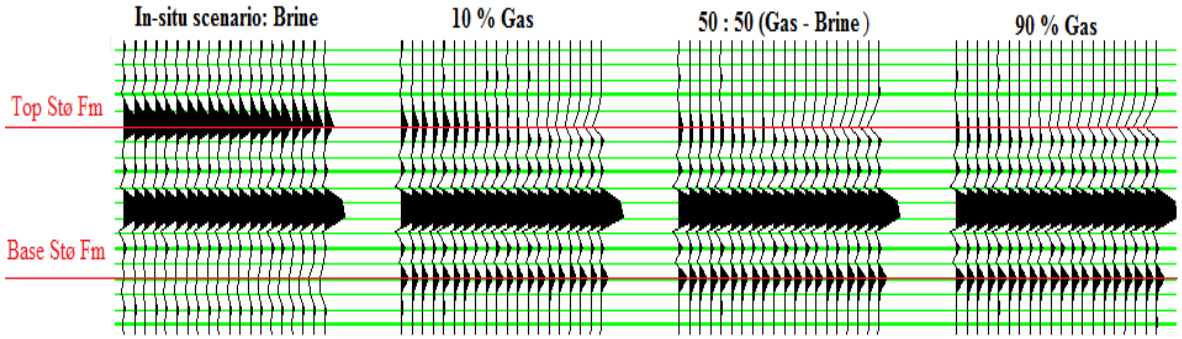

Fig. 4.11 Comparison of seismic responses to changes in reservoir fluid property and saturations from in-situ fluid (brine) to 10%, 50% and 90% gas saturations respectively. The offset range is from 0m to 1600m in all cases. Note the large change from in-situ scenario to 10% gas saturation.

To quantify fluid saturation effects, on the AVO response, relative percentage changes in Vp, Vs, bulk density and Poisson's ratio for the different gas saturations are calculated and the results are displayed in Figure 4.12. A 10% gas saturation results in a dramatic decrease in Vp by a factor of −16.05%. The Poisson's ratio decreases by a factor of −59.79% and the density by −1.06 %. At gas saturations of 50% gas (brine 50%) and 90% gas, the relative decrease in Vp is −15.72% and a further small decrease by −13.97% respectively. The difference in Poisson's ratio decrease between gas saturations of 50 to 90% is quite small (0.96) compared to gas saturations of 10 to 50% (9.25). Density decreases with increasing gas saturation. Vs on the contrary increase steadily, with small increments for the various gas saturations.

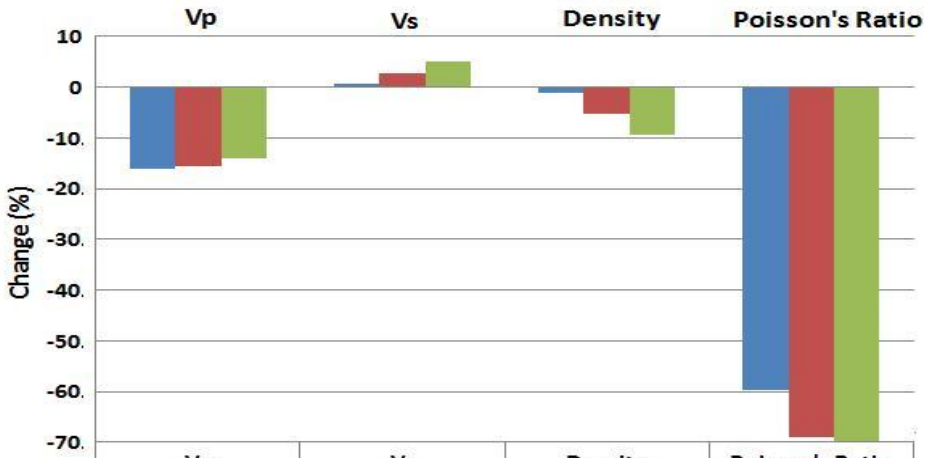

	Vp	Vs	Density	Poisson's Ratio
10% Gas	-16.05	0.53	-1.06	-59.79
50% Gas	-15.72	2.75	-5.28	-69.04
90% Gas	-13.97	5.12	-9.51	-70.11

Fig. 4.12 Fluid saturation effects on dynamic elastic properties of the Stø reservoir sands.

Figure 4.13 depicts a class I AVO response as high acoustic impedance than the overlying Hekkingen Formation which is the cap rock. With the introduction of 10% gas, the impedance of the sands drops with a phase change at 19 degrees. Continuous introduction gas into the reservoir systematically further decreases the impedance with corresponding reduction in the angle of phase change to an angle of 10 degrees at a gas saturation of 90%.

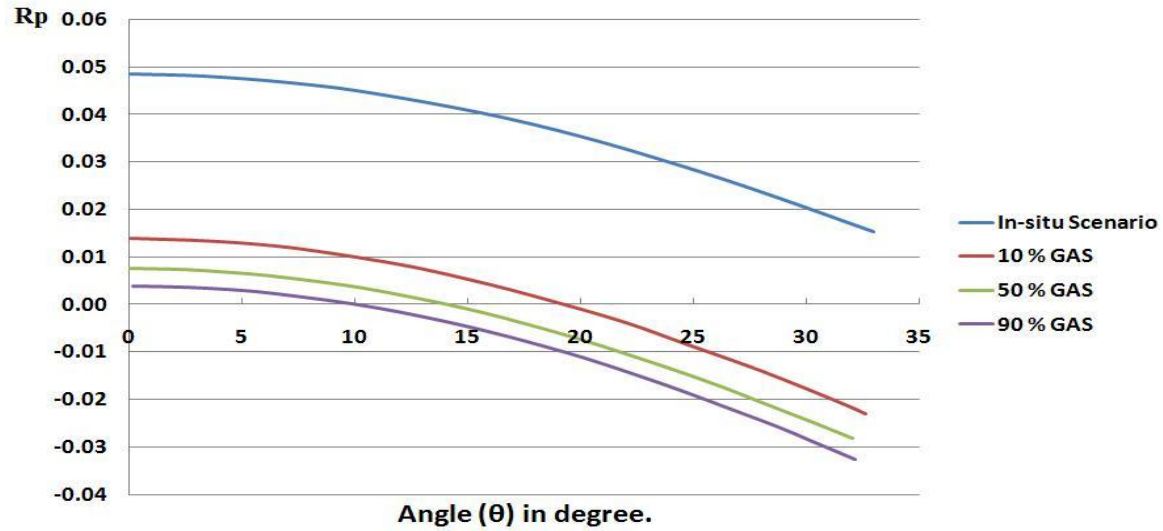

Fig. 4.13 Influence of changes in reservoir pore fluid and saturation on AVO response for Stø reservoir.

4.5 Discussion of Results

4.5.1 Cap Rock Properties

Typically, there is a large contrast in V_p/V_s ratio between clean sands and shales. Prolific sandstones of the Stø reservoir are capped by Jurassic shales of the Hekkingen formation in wells 7123/4-1A, 7122/6-1 and 7122/6-2 (weak class II P). This organic rich cap rock is much less dense with significant velocity and density inversion. Its elastic properties are much lower than the underlying reservoir sands thereby giving a strong positive reflector which decreases in magnitude with offset (Fig. 4.14). Hence a class I AVO response for these three wells at in-situ scenario. Well 7122/6-2 displays a weak class II P. In well 7122/4-1 the cap rock is rather the 29m thick Jurassic Fuglen Formation. These are pyritic mudstones with interbedded thin limestones (Dallan et al., 1988), high densities and acoustic properties. As such, the elastic contrast at the interface with the underlying Stø reservoir

sands is quite small. This inevitably results in a strong class II P AVO anomaly for the in-situ scenario.

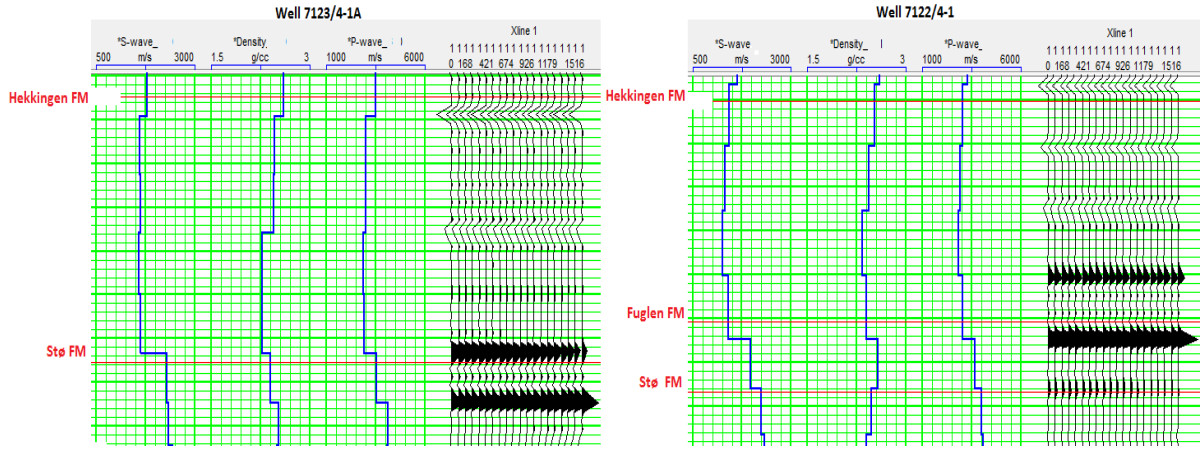

Fig. 4.14 Lateral variations in cap rock properties and its influence on AVO interpretation

Considering the interface between Triassic heterolithic Snadd reservoir sandstones and the Akkar Member of the Fruholmen Formation as caprock at in-situ condition, there is no major lateral change in the cap rock. The acoustic impedance contrast is quite small resulting from similar elastic properties across the interface. This similarity in elastic properties reflects the degree of heterogeneity within the Snadd reservoir with relatively high shale content (Fig.4.15), thereby yielding very low impedance AVO response for all wells.

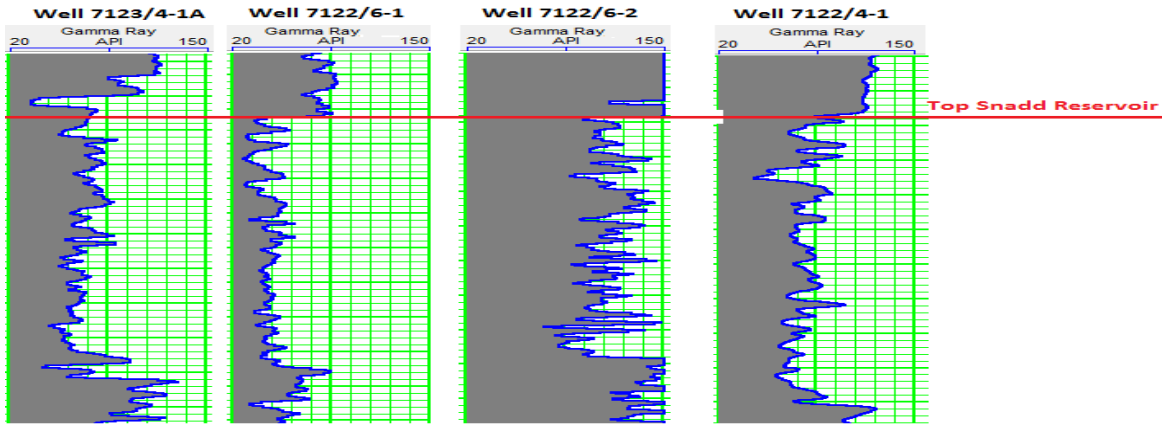

Fig. 4.15 High gamma ray measurements across the studied Snadd reservoir for five wells. Reservoir heterogeneity is largely related to different sediment provenances during the Triassic.

Therefore, the AVO response of the Stø reservoir is largely controlled by the cap rock properties. The Hekkingen – Fuglen interface in well 7122/4-1 could be misinterpreted as corresponding to thesame interface of Hekkingen – Stø in well 7123/4-1A as a result of the lateral lithological variation of the cap rock (Fig. 4.14).

4.5.2 Pore Fluid Property and Saturation Effects on AVO Response

So far mainly the effects of changes in elastic property across the cap rock – reservoir interface on the AVO response have been considered. An equally important issue is the effects of changes in fluid properties on AVO response after the pore fluid saturant is changed (Fig. 4.7). Brine is highly incompressible therefore substituting it with more compressible fluids such as oil and gas reduces the incompressibility of the Stø sandstones. Thus the bulk modulus of the brine – saturated reservoir sands is higher than that of the gas model. This result in the Vp of the brine-saturated in-situ scenario to be considerably higher than that of the gas model. Vs increases slightly as a result of the density reduction (Eq. 4.25). This reduces the Vp/Vs ratio with ΔVp and $\Delta\rho$ becoming more negative. The Poisson's ratio also consequently drops algebraically with an increase in pore fluid compressibility. Thus considering the top Stø reservoir reflection (Fig. 4.7), successively replacing the in-situ pore fluid (Brine) with oil and finally gas causes both Rp and G to become more negative (Eq. 4.6 and Eq. 4.5) with different magnitudes, than for the corresponding fully brine (in-situ) saturated sands. This results in a decrease in reflection coefficients with angle of incidence and a reverse in polarity at angles of $< 19^{o}$ after introducing an initial 10% gas into the reservoir (Fig. 4.13). The change in pore fluid compressibility caused a maximum velocity variation of 16.05 % (Fig. 4.12), however previous work (Hicks and Berry, 1956) predicted a maximum velocity variation in the range of 15 to 20 %. Substantially changing the Poisson's ratio between the Hekkingen Formation and Stø reservoir, by changing the reservoir pore fluid properties, results in large decrease P-wave reflection coefficient (more negative) with angle of incidence.

Table. 4.4 Pore fluids saturation effects on Vs and shear modulus.

Pore fluid saturation (%)	Vs (m/s)	Shear Modulus (GPa)
In-situ (Brine filled)	1612.43	5.88
10% gas	1621.00	5.89
50% gas	1656.72	5.90
90 % gas	1694.90	5.90

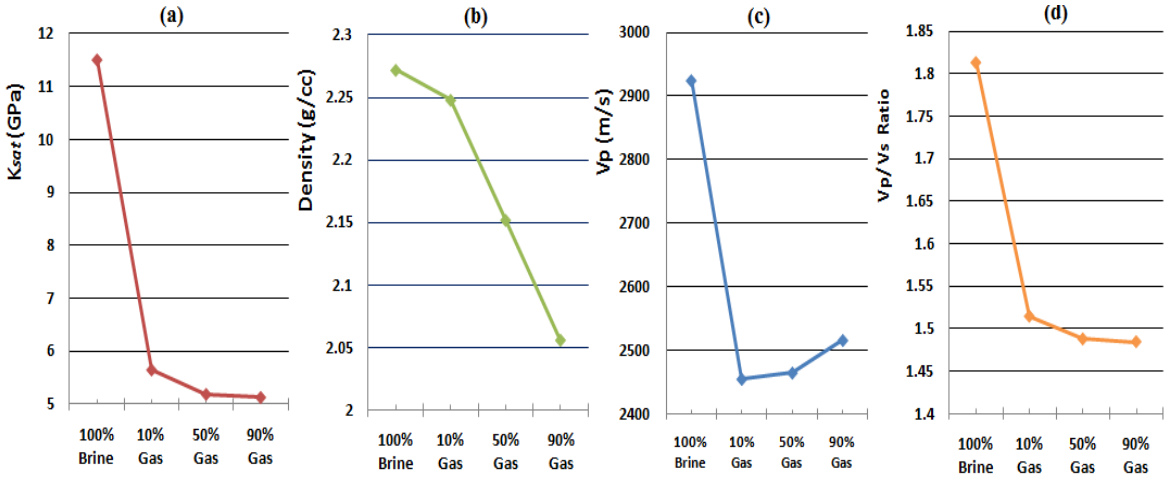

Fig. 4.16 Cross plots of (a) Ksat (b) Density (c) P-wave velocity (d) V_p /V_s ratio as a function of gas saturation.

Employing a two phase, water – gas, system to investigate the effects of saturation is of particular interest as the two fluids have contrasting properties. Brine and oil is usually considered to have similar acoustic impedances. Considering Equation (4.19), an initial introduction of 10% gas results in a dramatic drop in the saturated bulk modulus (K_{sat}) while the density experiences only a comparatively slight decrease (Fig.4.16). This is reflected by initial decrease in Vp seen both on seismic (Fig.4.11) and AVO response (Fig.4.13) with a significant decrease in R_p as a function of angle (θ). Between gas saturations of 50 – 90%, Ksat seems to stabilize while the density is still in sharp decline, suggesting that at these saturations density is the controlling factor given that the shear modulus and other factors influencing Vp are constant. Vs increase slightly while the shear modulus remains practically unchanged (Table. 4.4). With a small increase in Vs, the change in Vp/Vs ratio is small and the Poisson's ratio change at these same saturations is very little with a value of 0.01(Fig. 4.12) resulting in a relatively smaller difference in the AVO response when compared with the 10% gas saturation (Fig. 4.13). Vp/Vs ratio have been demonstrated to be characteristically > 2.0 for water – saturated unconsolidated rocks and values of < 2.0 indicated either well – consolidate rock or the presence of gas in unconsolidated sand (Gardner and Harris, 1968). The present results do not only confirm that Vp/Vs ratio are < 2.0 (Fig. 4.16d) in consolidated rocks but also establishes a possible variation trend for increasing gas saturation in the Stø reservoir based on this model.

4.5.3 Facies Variations and Depth Dependent AVO Signature

AVO anomalies result from a combined fluid and lithology (Smith, 1987) effects, however depth is also an important factor that should be considered during AVO analysis. The relatively high reflection coefficients in well 7122/6-1 (Fig. 4.10) could be inferred as portraying the sand content of the Snadd reservoir at this well location (Fig. 4.15) at in-situ condition due to high a impedance contrast with the caprock. Investigating lithology effects by flooding the reservoir with 100% brine will of course give higher Rp values as earlier demonstrated. However focus is on whether the variations of the relative magnitudes of these values are a direct result of lateral variation in lithofacies, depth or rather a combination of both factors.

Lithologic heterogeneity induces a similarity in elastic and acoustic rock properties across the reflecting / refracting interface between the Fruholmen Formation and the Snadd reservoir sands (Fig. 4.15). Generally, Vp/Vs ratio is higher for shales than for 'clean' sands. Increasing the shale content in 'clean' sands will give a more dense packing of grains thereby portraying a higher Vp/Vs ratio in the resulting 'shaly sands'. As a result, with similar Poisson's ratio across the reflecting/ refracting interface, one would expect small changes in reflection coefficients (Koefoed, 1955).

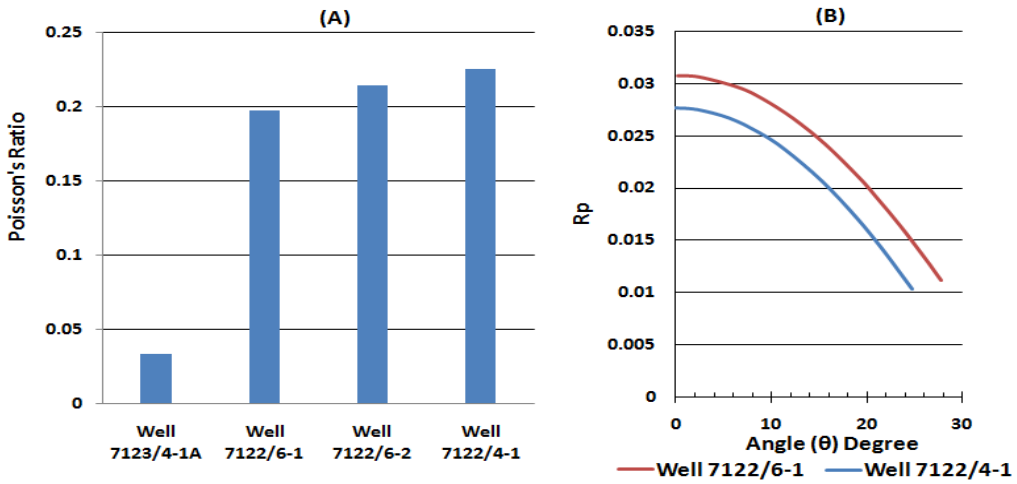

Fig. 4.17 (A) Poisson's ratios for different wells depicting an indication of significant lateral facies variation within the Snadd reservoir sandstones. (B) AVO response for thesame reservoir sands with same pore fluids but located at two widely different depths in wells 7122/4-1 and 7122/6-1.

At well 7122/4-1, the considered reservoir sands at the top of the Snadd Formation are at a depth of 2267m BSF while at well 7122/6-1, these sands are encountered at 1767m below sea floor making a difference in depth of 500m. This difference depth corresponds to a vertical effective stress of 5 MPa considerable enough to yield significant amount of mechanical compaction.

Velocities and densities vary considerably as a function of depth. This depth dependence is interpreted as a result of normal compaction (no overpressures) and diagenesis. Considering the brine model for wells 7122/4–1 and well 7122/6–1 (Fig. 4.17b), the AVO intercept becomes more negative in well 7122/4 –1 with depth, indicating that the acoustic impedance contrast between the Fruholmen shales and Snadd reservoir sands increases with depth accordingly. An explanation for this difference could be deduced from the differences in rates of compaction of shales and sandstones. That is, the density of Fruholmen shales in well 7122/4–1 is probably higher than in well 7122/6–1 given the extra 5MPa vertical effective stress though compaction of shales and mud rocks is a complex process of physical and chemical changes during burial.

The AVO response of the Snadd reservoir could probably be influenced by lateral facies variations and burial depth. This facies variation and depth dependent variation in the AVO response of brine filled sands may provide background knowledge for modelling different hydrocarbon scenarios.

4.5.4 Models Uncertainties

In a more advanced study, one would have to specify the percentage content of the different minerals in the reservoir rock matrix and use an averaging scheme to compute the effective bulk moduli. The same applies to the fluid properties where the bulk moduli could be computed using Patchy fluid mixing reflecting actual natural systems. The possibility that velocities of consolidated porous rocks are affected by the extent of pore fluid homogeneity (Gregory, 1976) though is taken care of by the initial assumptions (Gassmann, 1951) upon which the fluid replacement models are based.

The assumptions upon which these models are developed could however be invalid in anisotropic (Brown and Korringa, 1975) and heterogeneous material with contrasting elastic properties (Berge et al., 1998) due to violation of the assumption on pore connectivity and homogeneity of the rock particularly within the heterogeneous Snadd reservoir. Factors such as fluid-cement intergrannular acoustic coupling (micro-cracks in cement), and chemical interactions and pressures could also influence or dominate the effects of fluid saturation on rock with low porosity (Gregory, 1976). Isolating the effects facies variation from depth would be more accurate given a good control on mineralogy and pressure variation with depth.

CHAPTER 5: SUMMARY AND CONCLUSIONS

5.1 Summary

The Barents Sea is a complex mosaic of basins and platforms with substantial hydrocarbon reserves. Intracontinental sedimentation had been active from about 240 million years ago (Doré and Jensen, 1996) to early Cenozoic after which it bordered the developing Atlantic and Arctic oceans. Sedimentary Groups encountered in the study area include the Kapp Toscana, Adventdalen, Nygrunnen, Sotbakken and Nordland Groups.

An important aspect of the burial history of these sediments is the Cenozoic uplift which had about three different episodes (Ohm et al., 2008). This had a tremendous impact on the Hammerfest basin sedimentation and the hydrocarbon systems therein. Some of these include; the apparently higher source rock maturity for current burial depths for source rocks that were in the oil window prior to uplift and the low maturity at current depths for source rocks that had just entered the oil window prior to uplift. In certain cases, there probably could have been a seizure of hydrocarbon generation in areas that experienced the most uplift, higher reservoir diagenesis, though permeability may rather slightly increase in a tight reservoir sandstones due to rock elastic expansion due to a change in stress regime, cap rock fracture and a lower seal integrity (except in highly ductile materials), oil and gas redistribution or re-migration. As such, evaluation of the study area as a 'normal' subsiding basin would be misleading with ultimately unrealistic overestimation of rock dynamic properties.

The Tornerose prospect is found in block 7122 on one of positive elements along the Hammerfest basin axis. The structure is a southwards dipping rotated fault block with a NW – SE strike. This rotated fault block forms a structural closure as the main trapping mechanism. Based on the displacement of Formation tops, this fault has a throw of about 280m. The discovery well bore is the well 7122/6-1 with Gas and Condensates as contents. However the Stø and studied Snadd reservoirs are water wet.

Vertical effective stress generally increases as a monotonic function of depth thus; sediments become more compacted and consolidated. Siliciclastic sediments undergo a progressive and systematic change in intrinsic properties starting from the time the loose sediments are deposited at the sea floor where the compact mechanically, principally controlled by vertical effective stress , down to higher depth whereby with increased temperatures, chemical

compaction is the dominant porosity reduction process. These processes follow different gradients for both sandstones and shales.

Analysis of vertical and spatial variation in rock properties was carried out both at Formation and Group stratigraphic levels. Evaluation of compaction mechanisms and rock properties in within the context of this study had been met with a number of challenges and uncertainties as Formation evaluation entirely based on analysis of petrophysical logs and available literature.

No quantitative mineralogical analysis was available in this study. The lack of such data is unfortunate since mechanical and chemical compaction in mud rocks is greatly influenced by mineralogical and textural relationships (Fawad et al., 2010). Analysis of the gamma ray log in concert with other log types, as used in this thesis, provides mainly information on gross lithologic variation.

The well data are from different faulted segments across the area with a long tectonic history. Therefore, application of this simplistic method to estimate the magnitude of Cenozoic exhumation would not be able to isolate displacement due to regional uplift and displacement due to local fault related basin inversion. Quantification of the magnitude of these exhumation events gives a critical insight on the evolution of rock properties and adequate assessment of hydrocarbon systems. The method employed in this work to quantify these events had been quite straight forward and based on an experimental compaction curve of a well characterized synthetic kaolinite – silt (50:50) mixture from Mondol., (2011) (Personal communication).

AVO modelling is extensively employed in hydrocarbon exploration strategies. The core of AVO/ AVA modeling within the context of this study had been to evaluate reflectivity as a function of offset both at in-situ condition and at different pore fluid scenarios within the Stø and Snadd reservoirs. Investigation of the influence of some major factors that could possibly control the AVO response at the top of the Stø and Snadd reservoirs yielded some interesting results from which several conclusions could be deduced. The normal incidence reflection coefficient and contrast in Poisson's ratio between two bounding media to a greatly determines the resultant AVO response. This contrast in Poisson's ratio could arise from a number of factors such as facies variation, pore fluid properties, depth and porosity. Only the effects of the first three factors have been investigated within this study.

There are pros and cons associated with each of the AVO models presented herein. The cons are however closely associated with the some of the basic assumptions upon which the models were built.

5.2 Conclusions

Despite various assumptions and limitation associated with the different models and approaches employed within the context of this study, the following conclusions can be made:

- Two distinct compaction trends are found across the study area. These are namely: mechanical and chemical compaction. Porosity reduction by mechanical compaction of siliciclastic sediments dominates down to 1530m BSF at present burial depth. This process is governed by vertical effective stress. At depths > 1530m BSF, chemical compaction is the main porosity reduction process controlled by a time – temperature integral. Sands and shales compact along different gradients with sands showing a higher compaction gradient than the shales.

- At present burial, the transition from mechanical to chemical compaction domain in the reference well 7123/4 – 1A occurs at a depth of 1530m BSF and a present day temperature of about 45°C. After correcting for Cenozoic exhumation, this transition occurs at a depth of 3130m and at a temperature of 93°C. This is inferred to as corresponding to the chemical transformation of smectite to illite. Accurate determination of this zone is of great value when predicting reservoir quality (porosity, permeability, and cementation) particularly within the approach of this study where temperature information is absent.

- Experimentally compacted synthetic mudstones of kaolinite – silt (50:50), is shown to be very a valuable tool to constrain naturally compacted mudstones from the study area. Comparatively higher density/ velocity – depth gradients are due to the presence of non – clay constituents such as shallow biogenic silica and carbonates formed at low temperatures. Hence the good fit with other published data on naturally compacted samples. Experimental data has also proven to be a useful tool in estimating the magnitude of Cenozoic estimation in the area.

- The magnitude of exhumation is in the range of 1200 to 1600m across the study are without quantifying the uncertainties that are associated with the application of the method employed for correction. An integrated approach involving several techniques in estimating the magnitude of Cenozoic exhumation will definitely reduce the margin of uncertainty.

- The good reservoir qualities found in the Stø formation given the suggested burial may be related to the high pore pressures in the overlying Hekkingen Formation which could have reduced the amount of mechanical compaction in the Stø Formation.

- Averaging of petrophysical logs for the AVO analysis and modeling is of prime importance as an inaccurate block size would definitely result in a misleading AVO response. Averaged logs should be representative of the actual geologic conditions for the models to be reliable.

- The Stø reservoir sandstones display class I AVO response in wells 7123/4-1A, 7122/6-1, weak class II P in well 7122/6-2. In well 7122/4-1, a strong class II P AVO response is displayed at in-situ condition. Substituting the in-situ reservoir fluid with 90% oil gives a weak class II P AVO response for wells 7123/4-1A, 7122/6-1 and 7122/6-2. Well 7122/4-1 rather displays a class II response with a negative reflection coefficient. Substituting the in-situ fluids with 90% gas gives a class II P AVO response for wells 7123/4-1A, 7122/6-1 and 7122/6-2. Well 7122/4-1 displays a more negative Rp. The resultant successive changes in intercept and gradient for the different models are largely due to the changes in pore fluid compressibility after fluid substitution.

- At in-situ condition, in areas where the Hekkingen Formation is the cap rock, the Stø reservoir sandstones yield a class I AVO response. However, in areas where the Fuglen Formation rather serves as the cap rock, these sands display a low impedance class II P AVO response. The Stø reservoir sandstones are quite homogenous with good reservoir qualities throughout the study area. The disparity in AVO characteristic of the Stø reservoir is largely influenced by the variability in the cap rock properties across the study area. This gives a useful insight into the controls of

cap rock properties on an AVO response and should be considered during AVO analysis.

- The studied Snadd reservoir sandstones at the Top of the Formation is characterised by a class II P AVO response at in-situ condition across the study area. The low impedance contrast with the overlying Fruholmen formation is a direct result of the compositional heterogeneity of these sands with high clay content resulting in small contrast in elastic rock properties across the reflecting interface between these two Formations.

- Increase in depth influences the AVO response of the Snadd reservoir by reducing the elastic contrast across the reflecting interface with the cap rock (Fruholmen FM). The Intercept becomes more negative. This is related to increase in the degree of compaction resulting from vertical effective stress.

- Reservoir pore fluid replacement with an initial introduction of small gas saturations causes pronounce reduction in elastic moduli diagnostically significant on seismic. Changes in gas saturations, between 50 and 90 %, are not too evident on seismic due to the low sensitivity of seismic at high gas saturation. AVO analysis gives a quantitative measure of these systematic changes at all gas saturations with a corresponding decrease in the AVO intercept and consequent angles of polarity change considering an initial class I AVO response. However these results establish possible AVO variation trends for increasing gas saturation within the Stø reservoir sandstones.

- From a broad perspective, the various models presented in this thesis give a quick preliminary AVO evaluation of the Stø and Snadd reservoirs. With an expanding data base, more constrains could be incorporated into these elementary models.

References

ABERCROMBIE, H. J., HUTCHEON, I. E., BLOCH, J. D. & DE, C. P. 1994. Silica activity and the smectite-illite reaction Geology 22**,** 539 -542.

AKI, K. & RICHARDS, P. G. 1980. Quantitative seismology : Theory and methods W. H. Freeman and Co., 2.

AOYAGI, K., KAZAMA, T., Sekiguchi, K., Chilingarian, G.V., 1985. Experimental compaction of Na-montmorillonite clay mixed with crude oil and seawater, Water.Chemical geology, 49, 385 – 392.

ATHY, L.F., 1930. Density, porosity, and compaction of sedimentary rocks. American Association of Petroleum Geologists Bulletin 14 (1), 1–24.

AVSETH, P. 2010. Explorational Rock Physics – The Link Between Geological Processes and Geophysical Observables. In Petroleum Geoscience: From Sedimentary Environments to Rock Physics. Springer Berlin Heidelberg 2010. 403 – 426.

AVSETH 2005. Quantitative Seismic Interpretation: applying rock physics tools to reduce interpretatin risk. Cambridge University Press.

BALDWIN, B., BUTLER, C.O., 1985. Compaction curves. American Association of Petroleum Geologists Bulletin 69 (4), 622–626.

BALDWIN, B., 1971. Ways of deciphering compacted sediments. Journal of Sedimentary Petrology 41 (1), 293–301.

BERGE, P. A., THIMUS, J. F., ABOUSLEIMAN, Y., CHENG, A. H. D., COUSSY, O. & DETOURNAY, E. 1998. Pore Compressibility in rocks. Biot Conference on Poromechanics: Universite Catholique de Louvain**,** 351 - 356.

BERNABÉ, Y., FRYER, D. T. & HAYES, J. A. 1992. The effect of cement on the strength of granular rocks. Geophys. Res. Lett., 19**,** 1511-1514.

BIRD, K. J., CHARPENTIER, R. R., GAUTIER, D. L., HOUSEKNECHT, D. W., KLETT, T. R., PITMAN, J. K., MOORE, T. E., SCHENK, C. J., TENNYSON, M. E. A. & WANDREY, C. J. 2008. Circum-Arctic Resource Appraisal: Estimates of Undiscovered Oil and Gas North of the Arctic Circle. U.S Geological Survey 1.0**,** 3049.

BJØRKUM, P. A., OELKERS, E. H., NADEAU, P. H., WALDERHAUG, O. & MURPHY, W. 1998. Porosity prediction in quartzose sandstones as a function of time, temperature, depth, stylolite frequency, and hydrocarbon saturation AAPG Bulletin, 82**,** 637.

BJØRLYKKE, K. 1995. Geochemical constraints from formation water analyses from the North Sea and the Gulf Coast Basins on quartz, feldspar and illite precipitation in reservoir rocks Geological Society of London, 86**,** 33.

BJØRLYKKE, K. 1998. Clay mineral diagenesis in sedimentary basins — a key to the prediction of rock properties. Examples from the North Sea Basin 33**,** 15.

BJØRLYKKE, K., CHUHAN, F., KJELDSTAD, A., GUNDERSEN, E., LAUVRAK, O. & HGFEG, K. 2004. Modelling of sediment compaction during burial in sedimentary basins. In: OVE, S. (ed.) Elsevier Geo-Engineering Book Series. Elsevier.

BJØRLYKKE, K., HØEG, K. & MONDOL, N. H. 2010. Introduction to Geomechanics: Stress and Strain in Sedimentary Basins in,. Petroleum Geoscience. Springer Berlin Heidelberg.

BJØRLYKKE, K. AND JAHREN, J. 2010. Sandstones and Sandstone Reservoirs. In Petroleum Geoscience: From Sedimentary Environments to Rock Physics. Springer Berlin Heidelberg 2010. 113 – 140.

BJØRLYKKE, K., RAMM, M. & SAIGAL, G. C. 1989. Sandstone diagenesis and porosity modification during basin evolution International journal of earth sciences 78**,** 243.

BOLES., J. R. & FRANKS., S. G. 1979. Clay diagenesis in Wilcox sandstones of Southwest Texas; implications of smectite diagenesis on sandstone cementation. SEPM Journal of Sedimentary Research, 49**,** 55 - 70.

BROWN, R. J. S. & KORRINGA, J. 1975. ON THE DEPENDENCE OF THE ELASTIC PROPERTIES OF A POROUS ROCK ON THE COMPRESSIBILITY OF THE PORE FLUID. Geophysics, 40**,** 608-616.

BUGGE, T., ELVEBAKK, G., FANAVOLL, S., MANGERUD, G., SMELROR, M., WEISS, H. M., GJELBERG, J., KRISTENSEN, S. E. & NILSEN, K. 2002. Shallow

stratigraphic drilling applied in hydrocarbon exploration of the Nordkapp Basin, Barents Sea. Marine and Petroleum Geology, 19**,** 13-37.

BUTT, F. A., DRANGE, H., ELVERHØI, A., OTTERÅ, O. H. & SOLHEIM, A. 2002. Modelling Late Cenozoic isostatic elevation changes in the Barents Sea and their implications for oceanic and climatic regimes: preliminary results. Quaternary Science Reviews, 21**,** 1643-1660.

CASTAGNA, J. P., BATZLE, M. L. & EASTWOOD, R. L. 1985. Relationships between compressional-wave and shear-wave velocities in clastic silicate rocks. Geophysics, 50**,** 571-581.

CASTAGNA, J. P., SWAN, H. W. & FOSTER, D. J. 1998. Framework for AVO gradient and intercept interpretation. Geophysics, 63**,** 948-956.

CHUHAN, F., KJELDSTAD, A., BJØRLYKKE, K. & HOEG, K. 2002. Porosity loss in sand by grain crushing - experimental evidence and relevance to reservoir quality Marine and petroleum geology, 19(1)**,** 39-53.

CHUHAN, F., KJELDSTAD, A., BJØRLYKKE, K. & HOEG, K. 2003. Experimental compression of loose sands: relevance to porosity reduction during burial in sedimentary basins Canadian Geotechnical journal, 40(5)**,** 995-1011.

CORCORAN, D. V. & DORÉ, A. G. 2005. A review of techniques for the estimation of magnitude and timing of exhumation in offshore basins. Earth-Science Reviews, 72**,** 129-168.

CURTIS, C. D., LIPSHIE, S. R., OERTEL, G. & PEARSON, M. J. 1980. Clay orientation in some Upper Carboniferous mudrocks, its relationship to quartz content and some inferences about fissility, porosity and compactional history. Sedimentology, 27**,** 333-339.

DALLAN, A., WORSLEY, D. & OFSTAD, K. 1988. A lithostratigraphic scheme for the Mesozoic and Cenozoic succession offshore mid- and northern Norway. NPD-Bulletin, 4**,** 42-65.

DALLMANN, W. K. 1999. Lithostratigraphic lexicon of Svalbard. Review ad recommendations for nomenclature use. Upper Palaeozoic to Quaternary Bedrock. Norwegian Polar Institute, 318 pp.

DICKINSON, G., 1953. Geological aspects of abnormal reservoir pressures in the Gulf Coast Louisiana. American Association of Petroleum Geologists Bulletin 37 (2), 410–432.

DJÉRAN-MAIGRE, I., TESSIER, D., GRUNBERGER, D., VELDE, B. & VASSEUR, G. 1998. Evolution of microstructures and of macroscopic properties of some clays during experimental compaction. Marine and Petroleum Geology, 15**,** 109-128.

DORÉ, A. G. & JENSEN, L. N. 1996. The impact of late Cenozoic uplift and erosion on hydrocarbon exploration: offshore Norway and some other uplifted basins. Global and Planetary Change, 12**,** 415-436.

DOTT, R. H. 1964. Wacke, Graywacke and Matrix--What Approach to Immature Sandstone Classification? . SEPM Journal of Sedimentary Research, 34.

DURMISHYAN, A.G., 1974. Compaction of argillaceous rocks. International Geology Review 16 (6), 650–653.

DVORKIN, J. & NUR, A., . 1996. Elasticity of high-porosity sand-stones: Theory for two North Sea data sets. Geophys, 61**,** 1363 - 1370.

EHRENBERG, S. N. & BOASSEN, T. 1993. Factors controlling permeability variation in sandstones of the Garn Formation in Trestakk Field, Norwegian continental shelf Journal of Sedimentary Research, 63**,** 929.

ENGELHARDT, W.V., Gaida, K.H., 1963. Concentration changes of poresolutions during the compaction of clay sediments. Journal of Sedimentary Petrology 33 (4), 919–930.

ENGLAND., P. & MOLNAR., P. 1990. Surface uplift, uplift of rocks, and exhumation of rocks. Geological Society of America, 18**,** 1173-1177.

FALEIDE, J. I., GUDLAUGSSON, S. T. & JACQUART, G. 1984. Evolution of the western Barents Sea. Marine and Petroleum Geology, 1**,** 123-128, IN1-IN4, 129-136, IN5-IN8, 137-150.

FALEIDE, J. I., VÅGNES, E. & GUDLAUGSSON, S. T. 1993. Late Mesozoic-Cenozoic evolution of the south-western Barents Sea in a regional rift-shear tectonic setting. Marine and Petroleum Geology, 10**,** 186-214.

FAWAD, M., MONDOL, N. H., JAHREN, J. & BJØRLYKKE, K. 2010. Microfabric and rock properties of experimentally compressed silt-clay mixtures. Marine and Petroleum Geology, 27**,** 1698-1712.

FOWLER, S.R., WHITE, R.S., LOUDEN, K.E., 1985. Sediment dewatering in the Makran accretionary prism. Earth and Planetary Science Letters 75 (4), 427–438.

GABRIELSEN, R., H,., FÆRSETH, R., B,., JENSEN, L., N,., KALHEIM, J., E. & RIIS, F. 1990. Structural elements of the Norwegian continental shelf, Part I: The Barents Sea Region. Norwegain Petroleum Directorate Bulletin, 6**,** 47.

GARDNER, G. H. F. & HARRIS, M. H. 1968. Velocity and Attenuation of Elastic waves in Sands. PWLA 9th Annual Logging Symposium, 1968-M**,** 1-19.

GASSMANN, F. 1951. Elastic waves through a packing of spheres. Geophysics, 16**,** 673-685.

GLØRSTAD-CLARK, E., FALEIDE, J. I., LUNDSCHIEN, B. A. & NYSTUEN, J. P. 2010. Triassic seismic sequence stratigraphy and paleogeography of the western Barents Sea area. Marine and Petroleum Geology, 27**,** 1448-1475.

GRABOWSKA-OLSZEWSKA, B. 2003. Modelling physical properties of mixtures of clays: example of a two-component mixture of kaolinite and montmorillonite. Applied Clay Science, 22**,** 251-259.

GREGORY, A. R. 1976. Fluid saturation effects on dynamic elastic properties of sedimentary rocks. Geophysics, 41**,** 895 - 921.

GOULTY, N.R., 1998. Relationships between porosity and effective stress in shales. First Break 16 (12), 413–419.

HAM, H.H., 1966. New charts help estimate formation pressures. Oil and Gas Journal 65 (51), 58–63.

HANSEN, S., 1996. A compaction trend for Cretaceous and tertiary shales on the Norwegian shelf based on sonic transit times. Petroleum Geoscience 2 (2), 159–166

HEDBERG, H.D., 1936. Gravitational compaction of clays and shales. American Journal of Science 31 (184), 241–287.

HICKS, W. G. & BERRY, J. E. 1956. APPLICATION OF CONTINUOUS VELOCITY LOGS TO DETERMINATION OF FLUID SATURATION OF RESERVOIR ROCKS. Geophysics, 21**,** 739-754.

HO, N.-C., PEACOR, D. R. & VAN DER PLUIJM, B. A. 1999. Preferred Orientation of Phyllosilicates in Gulf Coast Mudstones and Relation to the Smectite-Illite Transition 47**,** 495-504.

HOUSEKNECHT, D. W. 1987. Assessing the Relative Importance of Compaction Processes and Cementation to Reduction of Porosity in Sandstones AAPG Bulletin, 71.

JAPSEN, P. & CHALMERS, J. A. 2000. Neogene uplift and tectonics around the North Atlantic: overview. Global and Planetary Change, 24**,** 165-173.

KOEFOED, O. 1955. ON THE EFFECT OF POISSON'S RATIOS OF ROCK STRATA ON THE REFLECTION COEFFICIENTS OF PLANE WAVES*. Geophysical prospecting, 3**,** 381-387.

KRIEF, M., GARAT, J., STELLINGWERFF, J. & VENTRE, J. 1990. A Petrophysical Interpretation Using The Velocities Of P And S Waves (full-waveform Sonic). The Log Analyst**,** 355-369.

LABERG, J. S., ANDREASSEN, K. & KNUTSEN, S. M. 1998. Inferred gas hydrate on the Barents Sea shelf — a model for its formation and a volume estimate. Geo-Marine Letters, 18**,** 26-33.

LANDER, R. H. & WALDERHAUG, O. 1999. Predicting porosity through simulating sandstone compaction and quartz cementation. AAPG Bulletin, 83**,** 433 - 449.

LARSEN, G., CHILINGER, G.V., 1983. Diagenesis in Sediments and Sedimentary Rocks; 2, Introduction, Developments in Sedimentology 25B. Elsevier Scientific Publishing Co., New York.

LI, Y., DOWNTON, J. & XU, Y. 2007. Practical aspects of AVO modeling. The Leading Edge, 26**,** 295-311.

LIU, G., LIPPARD, S., FANAVOLL, S., SYLTA, S., VASSMYR, S., SYLTA, O. & DORE, A. 1992. Quantitative geodynamic modelling of Barents Sea Cenozoic uplift and erosion Norsk geologisk tidsskrift 72**,** 313.

LOENG, H. 1991. Features of the physical oceanographic conditions of the Barents Sea. Polar Research, 10**,** 5-18.

MAGARA, K., 1968. Compaction and migration of fluids in Miocene mudstone, Nagaoka plain, Japan. American Association of Petroleum Geologists Bulletin 52 (12), 2466–2501.

MEADE, R. H. 1963. FACTORS INFLUENCING THE PORE VOLUME OF FINE-GRAINED SEDIMENTS UNDER LOW-TO-MODERATE OVERBURDEN LOADS1. Sedimentology, 2**,** 235.

MEADE, R. H. 1964. Removal of water and rearrangement of particles during the compaction of clayey sediments—review U.S Geological Survey Professional Paper, 497B**,** 1 - 22.

MEADE, R.H., 1966. Factors influencing the early stages of the compaction of clays and sands-review. Journal of Sedimentary Petrology 36 (4),1085–1101.

MINSHULL, T.A., WHITE, R., 1989. Sediment compaction and fluid migration in the Makran accretionary prism. Journal of Geophysical Research, B, Solid Earth and Planets 94 (6), 7387–7402.

MONDOL, N. H. 2008a. Experimental Compaction of clays: relationship between permeability and petrophysical properties in mudstones. Petroleum Geoscience, 14**,** 319.

MONDOL, N. H. 2008b. Synthetic mudstone compaction trends and their use in pore pressure prediction. First Break, 26**,** 0263-5046.

MONDOL, N. H., BJØRLYKKE, K., JAHREN, J. & HØEG, K. 2007. Experimental mechanical compaction of clay mineral aggregates--Changes in physical properties of mudstones during burial. Marine and Petroleum Geology, 24**,** 289-311.

MONDOL, N. H. (2011). Personal Communication, University of Oslo, Norway.

MORAD, S., ., AL-RAMADAN, K., ., KETZER, J., M,. & DE ROS, L., F,. 2010. The Impact of Diagenesis on the heterogeneity of sandstone reservoirs: A review of the

role of depositional facies and sequence stratigraphy. AAPG Bulletin, 94**,** 1267 - 1309.

MØRK, A., KARUD, R. & WORSLEY, D. 1982. Depositional and diagenetic environments of the Triassic and lower Jurassic succession of Svalbard. Canadian Society of Geologist, Calgary, Alberta, Canada**,** 371e398.

MØRK, M. B. E. 1999. Compositional Variation and Provenance of Triassic Sandstone from the Barents Shelf. Journal of Sedimentary Research 69**,** 690 - 710.

MURPHY, W. M., OELKERS, E. H. & LICHTNER, P. C. 1989. Surface reaction versus diffusion control of mineral dissolution and growth rates in geochemical processes. Chemical Geology, 78**,** 357-380.

NPD 2011. Fact pages. Norwegian Petroleum Directorate Fact pages.

OERTEL, G. & CURTIS, C., D 1972. Clay-Ironstone Concretion Preserving Fabrics Due to Progressive Compaction. Geological Society of America Bulletin, 83**,** 2597-2606.

OHM, S. E., KARLSEN, D. A. & AUSTIN, T. J. F. 2008. Geochemically driven exploration models in uplifted areas: Examples from the Norwegian Barents Sea. AAPG Bulletin, 92**,** 1191-1223.

OSBORNE, M. J. & SWARBRICK, R. E. 1999. Mechanisms for generating overpressure in sedimentary basins: A reevaluation: Reply. AAPG Bulletin, 83(5)**,** 800-801.

OSTRANDER, W. J. 1984. Plane-wave reflection coefficients for gas sands at nonnormal angles of incidence. Geophysics, 49**,** 1637-1648.

PALCIAUSKAS, V.V., 1991, Primary migration of petroleum, in R. K. Merril, ed., Source and migration processes and evaluation techniques: AAPG Treastise of Petroleum Geology, Handbook of Petroleum Geology, P. 13 – 22.

PELTONEN, C., MARCUSSEN, Ø., BJØRLYKKE, K. & JAHREN, J. 2008. Mineralogical control on mudstone compaction: a study of Late Cretaceous to Early Tertiary mudstones of the Voring and More basins, Norwegian Sea Petroleum Geoscience, 14**,** 127.

PELTONEN, C., MARCUSSEN, Ø., BJØRLYKKE, K. & JAHREN, J. 2009. Clay mineral diagenesis and quartz cementation in mudstones: The effects of smectite to illite reaction on rock properties. Marine and Petroleum Geology, 26**,** 887-898.

PEPPER, A. S. & CORVI, P. J. 1995. Simple kinetic models of petroleum formation. Part III: Modelling an open system. Marine and Petroleum Geology, 12**,** 417-452.

PERRODON, A. 1992. PETROLEUM SYSTEMS: MODELS AND APPLICATIONS. Journal of Petroleum Geology, 15**,** 319-325.

PETERS, K. E. AND CASA, M. R., 1994. Applied Source Rock Geochemistry. In The petroleum system – from source to trap: AAPG Memoir 60. P. 93 – 120.

PHILIPPI, G. & CORDELL, R. 1974. Depths of oil origin and primary migration: a review and critique. AAPG bulletin 56 2029.

POLYAEVA, E., KLARNER, S., LOWREY, C. J., ZABRODOTSKAYA, O. 2011. Depth Dependent Rock Physics Trends for Triassic Reservoirs in the Norwegian Barents Sea. 73rd EAGE Conference, Vienna, Australia, 23 – 26 May 2011.

PROSHLYAKOV, B.K., 1960. Reservoir properties of rocks as a function of their depth and lithology. Geol. Nefti i Gaza 12, 24–29.

RIIS, F., ., LUNDSCHIEN, B., A,., HØY, T., ., MØRK, A., . & MØRK, M., B, E,. 2008. Evolution of the Triassic Shelf in the northern Barents Sea region. Polar Research, 27**,** 318 - 338.

RUTHERFORD, S. R. & WILLIAMS, R. H. 1989. Amplitude-versus-offset variations in gas sands. Geophysics, 54**,** 680-688.

SCLATER, J.G., CHRISTIE, P.A.F., 1980. Continental stretching; an explanation of the post-Mid-Cretaceous subsidence of the central North Sea basin. Journal of Geophysical Research 85 (B7), 3711–3739.

SMELROR, M., MØRK, A., MØRK, M. B. E., WEISS, H. M. & LØSETH, H. 2001. Middle jurassic-lower cretaceous transgressive-regressive sequences and facies distribution off northern nordland and troms, Norway. In: OLE, J. M. & TOM, D. (eds.) Norwegian Petroleum Society Special Publications. Elsevier.

SMITH, G. C. 1987. Weighted Stacking for Rock Property Estimation and Detction of Gas. Geophysical prospecting, 35**,** 993.

SMITH, T. M., SONDERGELD, C. H. & RAI, C. S. 2003. Gassmann fluid substitutions: A tutorial. Geophysics, 68**,** 430-440.

STORVOLL, V., BJØRLYKKE, K., KARLSEN, D. & SAIGAL, G. 2002. Porosity preservation in reservoir sandstones due to grain-coating illite: a study of the Jurassic Garn Formation from the Kristin and Lavrans fields, offshore Mid-Norway. Marine and Petroleum Geology, 19**,** 767-781.

STORVOLL, V., BJORLYKKE, K. & MONDOL, N. H. 2005. Velocity-depth trends in Mesozoic and Cenozoic sediments from the Norwegian Shelf. AAPG Bulletin, 89**,** 359-381.

STORVOLL, V. & BREVIK., I. 2008. Identifying time, temperature, and mineralogical effects on chemical compaction in shales by rock physics relations. Leading Edge, 27**,** 738.

TERZAGHI, K., 1925. Principles of soil mechanics: I—phenomena of cohesion of clays. IV—settlement and consolidation of clay. Engineering News-Record 95 (19), 742–746, 874–878.

THYBERG, B., JAHREN, J., WINJE, T., BJØRLYKKE, K., FALEIDE, J. I. & MARCUSSEN, Ø. 2009. Quartz cementation in Late Cretaceous mudstones, northern North Sea: Changes in rock properties due to dissolution of smectite and precipitation of micro-quartz crystals. Marine and Petroleum Geology.

VASSOEVICH, N.B., 1960. Experiment in constructing typical gravitational compaction curve of clayey sediments. Nov. Neft. Tekh., Geol. Ser. (News Pet. Tech., Geol.) 4, 11–15.

VELDE, B., 1996. Compaction trends of clay-rich deep sea sediments. Marine Geology 133 (3–4), 193–201.

VERNIK, L. & LIU, X. 1997. Velocity anisotropy in shales; a petrophysical study. Geophysics, 62**,** 521-532.

VERNIK, L. & NUR, A., . 1992. Petrophysical classification of siliciclastics for lithology and porosity predictions from seismic velocities:. AAPG Bulletin, 7620110221**,** 1295

WALDERHAUG, O. 1994. Temperatures of Quartz Cementation in Jurassic Sandstones from the Norwegian Continental Shelf--Evidence from Fluid Inclusions SEPM Journal of Sedimentary Research, 64A.

WALDERHAUG, O., BJØRKUM, P. A., NADEAU, H. P. & LANGNES, O. 2001. Quantitative modelling of basin subsidence caused by temperature driven silica dissolution and reprecipitation. Petroleum Geoscience, 7**,** 107-113.

WAPLES, D. W. & COUPLES, G. D. 1998. Some thoughts on porosity reduction -- rock mechanics, overpressure and fluid flow. Geological Society, London, Special Publications, 141(1)**,** 73-81.

WELLER, J.M., 1959. Compaction of sediments. American Association of Petroleum Geologists Bulletin 43 (2), 273–310.

WHITE, D. A. 1993. Geologic risking guide for prospects and plays. AAPG Bulletin, 77**,** 2048-2061.

WORSLEY, D. 2008. The Post-Caledonian development of Svalbard and the Western Barents Sea. Polar Research, 27**,** 298 - 317.

WORSLEY, D., JOHANSEN, R., & KRISTENSEN, S.E. 1988. The Mesozoic and Cenozoic succession of Tromsøflaket. In A Dallan, D. Worsley & K. Ofstad (Eds.), A lithostratigraphic scheme for the Mesozoic and Cenozoic succession offshore Mid- and Northern Norway. Norwegian Petroleum Directorate (NPD) Bulletin, 4, 42 – 65.

ZOEPPRITZ, K. 1919. Erdbebenwellen VIIIB, über Reflexion and Durchgang Seismischer Wellen durch Unstetigkeitsflachen. Nachrichten, I**,** 66-84.

Appendix

List of figures

Chapter 1. Introduction

Fig. 1 Location map of the Barents Sea (adapted from Faleide et al., 1984).....1

Fig. 1.1. Location map of two major commercial hydrocarbon fields in the South West Barents Sea Snøhvit and Goliat Fields. Modified from NPD Factmaps (2011).....2

Fig. 1.3 Map of Norway and Barents Sea (inset map) and the location of the study area about 45Km NNE of Goliat and about 55Km east of Snøhvit fields. Source: NPD Factmaps (2011).....2

Fig. 1.4 Well bore location map of the study area across the Tornerose prospect.....8

Chapter 2. Regional Geological Framework

Fig. 2.1 Tectonic framework of the entire Barents Sea region. Source:(Gabrielsen et al., 1990)...12

Fig. 2.2 Subsidence curves for different parts of the Norwegian Barents Sea. Three major uplift and erosion episodes are indicated to occur at 60 Ma, 35 Ma and recent. Source: (Ohm et al., 2008).....13

Fig. 2.3 Schematic illustration of Barents Shelf and Spitsbergen lithostratigraphic column. Formation definition is by(Worsley, 2008). Source: (Bugge et al., 2002).....15

Fig. 2.4 Core photograph of the Hekkingen Formation from well 7228/9-1S. Source: (NPD, 2011).....18

Fig. 2.5 Tentative maturity map depicting oil maturity distribution of Permian, Triassic and Jurassic source rocks. This map is based on maturity data from wells in the area, semi-regional maturity trends of vitrinite reflectance (Ro) versus depth. The study area is highlighted by the solid red circle showing the occurrence of multiple source rock. Modified from: Ohm et al., 2008.....19

Fig. 2.6 Wireline log character across the Stø Reservoir from well 7123/4-1A. P-wave, S-wave, Neutron porosity, water saturation, resistivity and gamma ray logs respectively. Different depositional facies are clearly identified using the gamma ray log.....20

Fig. 2.7 Core photograph obtained around the top of Stø reservoir sandstones from well 7122/6-1 with a core start depth of 1595m BSF and end depth of 1599 m BSF. These sands are prolific with excellent reservoir qualities. Source: NPD Factpage 2011.....21

Fig. 2.8 Wireline log responses across the studied Snadd reservoir sand unit found at the top of the Formation from well 7123/4-1A. P-wave, S-wave, Neutron porosity, water saturation, resistivity and gamma ray logs respectively.....22

Fig. 2.9 Modified core photo of the Ladinian Snadd Formation from at two different depth from (a) well 7230/05-U-04 AT 64.2m and (b) from well 7230/05-U-04 at 60.7m. Source: Bugge et al. 2002.....22

Fig. 2.10 Structural map of the study area illustrating the trap style of the Tornerose prospect on the rotated fault block. Source: NPD Factmaps. 2011.....23

Chapter 3. Compaction and Evolution of Rock Properties

Fig. 3.1 Principal aspects of sediment compaction. With increasing burial depth, sediments are subjected to changes in physical properties as a function of increasing stress and temperature. Source: Bjørlykke, 1998.....24

Fig. 3.2 Sonic velocity measurements (every 0.5 – 0.7m with depth) from seventeen wells located in the western region in of the Haltenbanken area- Norwegian North Sea (after Storvoll et al. 2005). The estimated trend line (dashed blue line) will be used for comparism with well data from this study area.....25

Fig. 3.3 Schematic illustration of the contributions of overburden stress, stress at grain contacts and pore pressure to mechanical compaction.....27

Fig. 3.4 Experimental mechanical compaction of brine-saturated kaolinite aggregates, sorted by grain size (after Mondol et al. 2008). Samples containing less than 2µm sized kaolinite aggregates retained higher porosity compared to all other mixtures. The maximum porosity reduction is observed in the composite mixtures containing all grain sizes, demonstrating the importance of grain size and sorting in determining rock properties....27

Fig. 3.5 Diagenetic processes, mainly quartz cementation as a function of temperature and time. Note that quartz cementation will continue also during uplift as long as the temperature exceeds 70–800C. Source: (Bjørlykke et al., 2010)…….29

Fig. 3.6 Cross plots of P-wave velocity (a) and S-wave velocity versus the vertical effective stress for dry (in gray) and brine-saturated (in black) clay mixtures (Mondol et al. 2007). Solid lines show least square fits to the data.....30

Fig. 3.7 Formation of (A) authigenic micro quartz (mQtz) cement in mudstones from Northern North Sea. Source: (Thyberg et al., 2009). (B) pore filling illite formed either by alteration (dissolution and precipitation) of smectite and/ or from kaolinite and K-feldspars Source: (Bjørlykke, 1995).....31

Fig. 3.8 Experimental compaction of fine-grained and coarse-grained sand showing that well sorted fine grained is less compressible than coarse grained sands. Source: (Chuhan et al., 2003).....32

Fig. 3.9 (A) Schematic illustration of Pressure solution of quartz clasts at grain contacts with clays (stylolite). Grain coatings prevent or slow down quartz cementation and preserve porosity at greater depths. (b) Quartz cement with smooth crystal surfaces as overgrowth on clastic grains. Source: (Bjørlykke et al. 2010).....33

Fig. 3.10 Cross plots of Vp/ Bulk density / Neutron porosity/Gamma ray versus depth for five wells cross the entire study area. Generally two distinct compaction trends are identified on all cross plots.....37

Fig. 3.11 Vp (m/s) - Depth (m) plot for well 7123/4-1A at present burial depth below sea floor (BSF). The various Formations have been separated in to different colours for better illustration. The general trend line (in black) is not for a particular lithology but for the entire well data. The highlighted area (black circle) represents anomalous velocity. The

transition zone (TZ) separates mechanical compaction (MC) from chemical compaction (CC).....38

Fig. 3.12 Shear modulus versus porosity (NPHI) for shales only in well 7123/4-1A. Colour coded with depth to illustrate the transition zone (TZ) from mechanical compaction (MC) to chemical compaction (CC) occurring at the 'knee point'.....40

Fig. 3.13 Cross plots of P-wave versus Depth for (a) entire well data, (b) clean sands and (c) shales only, for well 7123/4-1A colour coded with V-shale. The highlighted area in red circle indicates a zone of overpressure in the Hekkingen Formation. Sands compact along a higher gradient than shales. A similar pattern is observed for wells 7122/4-1, 7122/6-1 and 7122/6-2.....41

Fig. 3.14 Crossplot of Shear-wave velocity versus P-wave velocity for well 7123/4-1A color coded with V-shale. S-wave velocities show a lithology dependent gradation, hence good lithology indicators.....42

Fig. 3.15 Attribute cross section from the Vs versus Vp cross plot versus depth (m) BSF for well 7123/4-1A showing the vertical distribution of clean sands (orange) as in the Stø reservoir and shaly sands (blue) as in the Snadd reservoir. The Triassic sequence is dominated by shaly sands.....43

Fig. 3.16 Effect of incipient quartz cement on bulk density, well 7123/4-1 at present burial depth below sea floor (BSF). Vp/ Vs / Bulk Density versus Depth (m) Below sea floor (BSF). The transition zone (TZ) between mechanical compaction (MC) and chemical compaction is marked by the red line.....43

Fig. 3.17 Exhumation estimates for well 7122/2-1 using experimental compaction curves for Clay - Silt and Clay - Clay mixtures. The shales are for mechanical compaction domain only...44

Fig. 3.18 Correction for exhumation using shales only, for five wells corresponding to mechanical compaction. (a) Vp(m/s) – Depth(m)BSF at present burial depth compared with different experimental clay mixtures. (b) Vp(m/s) – Depth (m) after correcting for exhumation and compared with experimental samples.....45

Fig. 3.19 Shales only, corresponding to mechanical compaction after correcting for exhumation. (a) Neutron porosity (NPHI) / Density porosity (DPHI) versus depth compared with experimental porosity-depth curve for a Kaolinite – silt (50:50) mixture. (b) cross plot for bulk density – Depth for shales compared with experimental density curve for a kaolinite – silt (50:50) mixture.....46

Fig. 3.20 Composite cross plot of Vp – Depth for 5 wells using entire well data. Trend lines from three different published and experimental data have been included for comparison. (a) Present depth below sea floor (BSF). (B) Corrected for Tertiary exhumation. The highlighted area (red circle) represents anomalous velocity from shallow carbonates.....48

Fig. 3.21 Modified tentative uplift map illustrating the total amount of uplift based on vitrinite data. The area under consideration in this study is indicated by the red circle. Modified from: (Ohm et al., 2008).....49

Fig. 3.22 Cross plots of Vp (m/s) and Resistivity (Om^2/m) logs versus Depth (m) BSF for (A) well 7123/4-1A and (B) well 7122/6-2. Both wells depict a decrease in resistivity around the transition from mechanical to chemical compaction though as seen from the cross plots the depth of this zone is slightly different for both wells. Both well data are put at thesame depth level uniquely for illustration purpose.....51

Fig. 3.23 Cross plot of P-wave velocity (m/s) versus Density (g/cc) colour coded with V-shale. The highlighted area (red circle) depicts low density and velocity in the organic rich and overpressured Hekkingen Formation.....56

Fig. 1.24 Variability in mudstone compaction trends. Variations are prominent in the mechanical compaction. After Mondol et al., 2008, (modified from Mondol et al., 2007).....57

Chapter 4. AVO/AVA Modeling

Fig. 4.1 Schematic illustration of the Convolutional trace model. The pulse used is a zero-phase Ricker wavelet with peak frequency at 45 Hz……61

Fig.4.2 Mode conversion (energy partitioning) of an incident P-wave producing P and S reflections and transmissions. The reflected angle of the converted S-wave is smaller than the reflected angle of the P-wave……62

Fig. 4.3 (a) AVO intercept (A) versus Gradient (B) cross plot showing four quadrants. (b) Plane wave reflection coefficients at the top of each Rutherford and Williams (1989) classification of gas sand after (Castagna et al., 1998)……..66

Fig. 4.4 Similarities and differences a between measured Vs, Vs_Castagna and Vs_Krief (a) comparism on wireline logs within the Stø reservoir (b) comparison of the amplitude response at the top of the reservoir……...70

Fig. 4.5 Ricker zero phase wavelets in time and frequency domain for different parameters. (a) The dominant frequency is at 45Hz, sample rate of 2(ms) and wavelet length of 200m. It is used in this study. (b) Is a 20Hz wavelet, with a sample rate of 2(ms), a wavelet length of 200m……...72

Fig. 4.6 Illustration of the implication of block size on NMO corrected synthetic CDP gathers and eventual AVO signatures. A block size of 20m results in a high impedance AVO signature. While a block size 23m yields a low impedance AVO signature……73

Fig. 4.7 AVA cross plot for four wells at top Stø reservoir at in-situ scenario, Oil model and Gas model with a maximum offset of 40 degrees. Three of the wells yield class I AVO response at in-situ scenario while well 7122/4-1 shows a class II AVO response……..76

Fig. 4.8 Quantitative analysis of zero-offset reflectivity of four wells at: in-situ scenario, oil model and gas model……76

Fig. 4.9 AVA cross plot for four wells for top Snadd Formation at in-situ scenario and after substituting the pore fluid with entirely 100% Brine……...77

Fig. 4.10 Illustration of zero offset reflectivity for four wells at in-situ scenario (blue) and at 100% brine saturation (red)……78

Fig. 4.11 Comparison of seismic responses to changes in reservoir fluid property and saturations; from in-situ fluid (brine) to 10%, 50% and 90% gas saturations respectively. The offset range is from 0m to 1600m in all cases. Note the large change from in-situ scenario to 10% gas saturation……79

Fig. 4.12 Fluid saturation effects on dynamic elastic properties of the Stø reservoir sands……...79

Fig. 4.13 Influence of changes in reservoir pore fluid and saturation on AVO response for Stø reservoir……...80

Fig. 4.14 Lateral variations in cap rock properties and its influence on AVO interpretation…….....81

Fig. 4.15 High gamma ray measurements across the studied Snadd reservoir for five wells. Reservoir heterogeneity is largely related to different sediment provenances during the Triassic…….....81

Fig. 4.16 Cross plots of (a) Ksat (b) Density (c) P-wave velocity (d) Vp /Vs ratio as a function of gas saturation…….83

Fig. 4.17 (A) Poisson's ratios for different wells depicting an indication of significant lateral facies variation within the Snadd reservoir sandstones. (B) AVO response for thesame reservoir sands with same pore fluids but located at two widely different depths in wells 7122/4-1 and 7122/6-1……..…..…84

List of Tables

Table. 1.1 Detail field statistics. (Source: NPD. 2011)…….7

Table. 2.1 Stratigraphic statistics of five wells across the study area. Source: (NPD, 2011)…….14

Table. 3.1 Exhumation estimates for four wells based on experimental compaction curve of a Kaolinite - Silt mixture (50:50). Mondol 2011 (personal communication)……...45

Table. 3.2 Transition zones (TZ) from mechanical to chemical compaction with the corresponding temperatures of transition for five wells both at present day depth and temperatures and after correcting for exhumation respectively…….53

Table. 4.1 Adapted range of reflectivity values used to classify AVA response.....75

Table. 4.2 Top reservoir sand reflection coefficient versus angle behavior of the Stø reservoir for different fluid scenarios……..…75

Table. 4.3 Top reservoir sand reflection coefficient versus angle behavior of the Snadd reservoir for different fluid scenarios……77

Table. 4.4 Pore fluids saturation effects on Vs and shear modulus……....82